UNIVERSITÀ DEGLI STUDI DI BRESCIA

Dipartimento di Ingegneria

Scuola di Dottorato in
Scienze Fisiche applicate all'Ingegneria
Ciclo XXXV

Synthesis and Characterization of Inorganic Perovskites for Nanophotonics

Sintesi e Caratterizzazione di Perovskiti Inorganiche per Nanofotonica

Candidate

Giammarco Roini (ID number 730600)

Thesis Advisors

Prof. Ivano Alessandri

Prof.ssa Anna Vinattieri

Academic Year 2021/2022

Thesis not yet defended

Synthesis and Characterization of Inorganic Perovskites for Nanophotonics
PhD thesis. University of Brescia

This thesis has been typeset by LaTeX and the UniFiTh class.

Author's email: g.roini@unibs.it

Abstract

English

In this PhD thesis several aspects of the physics of halide inorganic perovskites are addressed. In particular I will focus on:

- Intrinsic properties of the material such as the structural and dynamical disorder by a deep study of the photoluminescence in a large set of $CsPbBr_3$ samples differing for morphology and synthesis protocol. Being the disorder affecting the spectral line shape of the photoluminescence, and playing a major role in the carrier transport properties at the band edge, the investigation here presented is of interest for the large set of optoelectronic applications of halide perovskites. The results obtained during the PhD activity contribute to clarify the main characteristics of disorder in this class of semiconductors.

- The interaction between $CsPbBr_3$ microcrystals and the substrate/metasurface where they are deposited. In fact, the integration of halide perovskites in metasurfaces and photonic structures is a research at the early stage and deep investigation is required before the implementation of innovative photonic devices. In particular I will present a set of experimental results concerning non-linear effects (superlinear and sublinear behavior) in the radiative emission of $CsPbBr_3$ films deposited by spin-coating on a particular type of metasurface realized by core-shell microresonators (*T-Rex*) assembled in an hesagonal pattern on a silicon substrate. The experimental results evidence the presence of *Amplified Spontaneous Emission* (ASE) which, depending on the sample structure, *does or does not* show up with a superlinear increase of the emission. In particular we distinguish between two processes: light amplification by randomly arranged emitters and amplification by a quite ordered distribution of nanocrystals around a resonator.

- $CsPbBr_3$ has optimal characteristics as adsorber and catalyst in the processes of absorption of pollutants from industrial waste water.

In the final part of my work, in the appendix, I will show preliminary results concerning the fast adsorption of Methylene Blue (MB), a substance typically used in the textile industry, dissolved in aqueous solution when $CsPbBr_3$ nanopowders (NPs) are encapsulated inside chitosan bubbles (CH-BB). A significant increase of the adsorption percentage of MB is obtained in presence of the perovskite nanopowders respect to the use of empty chitosan bubbles.

Italian

In questa tesi di dottorato vengono affrontati diversi aspetti riguardanti la fisica delle perovskiti inorganiche alogenate. In particolare mi focalizzerò su:

- Proprietà intrinseche del materiale come il disordine strutturale e dinamico, approfondito da uno studio della fotoluminescenza in un grande insieme di campioni $CsPbBr_3$ che si differenziano per morfologia e protocollo di sintesi. Siccome il disordine pregiudica la forma spettrale della linea della fotoluminescenza e gioca un ruolo importante nelle proprietà di trasporto di carica al bordo della banda, l'indagine presentata in questa tesi è di interesse per l'ampio insieme delle applicazioni optoelettroniche delle perovskiti alogenate. I risultati ottenuti durante l'attività di dottorato contribuiscono a chiarire le principali caratteristiche del disordine in questa classe di semiconduttori.

- L'interazione tra i microcristalli di $CsPbBr_3$ e il substrato/metasuperficie su cui sono depositati. Infatti, l'integrazione di perovskiti alogenate su metasuperfici e strutture fotoniche è una ricerca in fase iniziale e un'indagine approfondita è necessaria prima dell'implementazione di dispositivi fotonici innovativi. In particolare presenterò una serie di risultati sperimentali riguardanti effetti non lineari (comportamento superlineare e sublineare) nell'emissione radiativa di film $CsPbBr_3$ depositati da spin-coating su un particolare tipo di metasuperficie realizzata da microrisonatori core-shell (*T-Rex*) assemblati in pattern esagonali su un substrato di silicio. I risultati sperimentali evidenziano la presenza di *Amplified Spontaneous Emission* (ASE) che, a seconda della struttura del campione, si presenta e non si presenta con un aumento superlineare dell'emissione. In particolare si distinguono due processi: l'amplificazione della luce da emettitori disposti in modo casuale e l'amplificazione da una distribuzione abbastanza ordinata di nanocristalli intorno a un risonatore.

- $CsPbBr_3$ ha caratteristiche ottimali come adsorbitore e catalizzatore nei processi di assorbimento degli inquinanti dalle acque reflue industriali.

Nella parte finale del mio lavoro, in appendice, mostrerò i risultati preliminari riguardanti il rapido assorbimento del Blu di Metilene (MB), una sostanza tipicamente utilizzata nell'industria tessile, disciolta in soluzione acquosa quando le nanopolveri di $CsPbBr_3$ (NPs) sono incapsulate all'interno di sferette di chitosano (CH-BB). Un aumento significativo della percentuale di adsorbimento di MB si ottiene in presenza delle nanopolveri di perovskite rispetto all'uso delle sferette di chitosano vuote.

Contents

Introduction

The rapid technological development we have witnessed in recent decades stems from the enormous advances in material science, which benefits from basic research in physics and chemistry. The technological sectors that have mostly taken advantage from the innovative thrust of new materials are the field of renewable energy, in particular photovoltaics, photonics and sensors. In these areas, the most innovative devices arise from the use of a class of semiconductors called *perovskite*. The term "perovskite" was initially coined to identify calcium titanate ($CaTiO_3$) but afterwards it was attributed to all compounds having the same chemical formula as calcium titanate, ABX_3, in which A and B are typically metal cations while X an anion. In these days, the perovskites of interest for scientific and industrial applications are based on halides and the X ion can be chlorine, bromine or iodine (X = Cl, Br, I) [117, 60, 43]. Halide perovskites are named organic-inorganic or inorganic according to the organic or inorganic nature of cation A. What makes these materials particularly interesting is their versatility: in fact, being able to use a substantial number of different elements in their synthesis, it is possible to engineer materials with multiple properties that find applications in numerous fields of optoelectronics. In addition, the chemical synthesis process is a low cost procedure when compared with other techniques used for semiconductor fabrication (such as epitaxial techniques). The control of chemical synthesis also allows to modify the nanostructuring of the material, thus being able to make bulk crystals, nanowires, nanoplates and quantum dots (QDs). It is worth noting that halide perovskites can be realized on different substrates: amorphous as glass or polymer, crystalline as sapphire, silicon, etc. and also metallic. The role of substrate can be relevant to determine the overall properties of the material. Since the early 2000s, research has focused on hybrid perovskites, which are having a significant impact in photovoltaics; in fact prototype perovskite cells have shown photovoltaic conversion efficiency comparable to that of traditional silicon cells[66, 63, 144, 15, 76], with greater ease of synthesis and lower production costs. However, hybrid perovskites are considerably sensible to moisture and oxygen [96, 70], which limits their use in applications being the material stability a fundamental requirement. Starting in 2015, inorganic halide perovskites (hereafter indicated as IHP) based on Caesium (Cs) were studied; they have similar optoelectronic properties as the hybrid counterparts but better stability over a long period of time. With the synthesis of the first Quantum Dots (QDs) of $CsPbX_3$ [103], extraordinary optical properties were observed such as high luminescence efficiency, relatively narrow emission bands (12-40 nm), when compared with those of organic QDs or II-VI semiconductors and a wide spectral range of emission obtainable by varying the halogen or the structuring of the material

on a micrometer/nanometer scale. In particular, this latter feature makes IHPs interesting not only for applications to photovoltaics and sensors, but especially for the realization of light emitters, such as LEDs, which use thin films and QDs [78, 147] and Lasers, made from QDs and Cs-based perovskite micro/nanocrystals [132, 32].

$CsPbBr_3$ belongs to the family of IHPs and it is a semiconductor of extreme interest for the realization of incoherent, coherent light sources, resonators, waveguides and other photonic devices in the green spectral region where the efficiency of indium nitride emitters is poor[158].
My PhD work concerns an in-depth study of the optical properties of $CsPbBr_3$ in different morphologies: micro/nanocrystals and compact polycrystalline films deposited on different substrates and on metasurfaces. In particular, several aspects of inorganic halide perovskite will be addressed such as intrinsic properties of the material (structural and dynamical disorder), and properties related to the deposition technique and the substrate on which perovskite is deposited.

The thesis outline is as follows:

- **Chapter 1**: in this chapter I describe the main physical characteristics of perovskites, focusing on the physical and optical properties of halide-based inorganic perovskites, going into the details of the physical processes that characterize this type of material. I also present the main applications to devices and introduce the concepts behind the interaction between $CsPbBr_3$ and microresonator called *T-Rex*.

- **Chapter 2**: I present the main synthesis/deposition techniques used by myself and collaborators to realize the samples I investigated. In particular I describe Spin-coating deposition and Radio-Frequency Magnetron Sputtering growth, making a comparison and enlighting advantages and disadvantages. I also present the experimental setups used for the analysis of the optical properties of the samples, describing the various analysis techniques used to perform the experiments. Moreover I report on some results related to the morphology, structure and stoichiometry of the investigated samples providing SEM and SNOM images of the different kind of samples

- **Chapter 3**: this chapter is devoted to the high resolution (in space and time) photoluminescence results. In particular I will addressthe topic of disorder, presenting a detailed analysis of the Urbach tail in bulk and polycristalline films. This topic is of relevance for all the applications where absorption and transport are involved.

- **Chapter 4**: in this chapter I present experimental results that show the transition between incoherent emission (PL) and amplified spontaneous emission (ASE) in spin-coated films on a semiconductor substrate and on a metasurface realized by micro/nanospheres having a core of SiO_2 and a shell of TiO_2 (hereafter indicated as *T-Rex*) on a silicon substrate. This topic is of relevance for the realization of devices aiming to amplify the emission in a waveguided mode and/or laser microresonators.

This thesis closes with a concluding chapter that collects and summarizes the most relevant results of all the experiments I performed and indicates future developments aimed at engineering these materials for the realization of efficient emitters with controlled properties as polarization, directionality, etc. and efficient sensors/adsorbers.

In particular, in Appendix A I present a research which is in progress concerning the use of $CsPbBr_3$ nanopowders as adsorber and catalyst for the photodegradation of pollutants. In particular I will show results for Methylene Blue (MB), a typical pollutant that can be found in water as waste of textile industry. I will also discuss the possibility to circularly reuse perovskites recovered from other applications and exploit their properties as pollutant adsorbers.

In Appendix B I report the list of scientific articles I coauthored and conferences I attended.

Chapter 1

Halide perovskites: structure and electrical properties

In this chapter I present the main structural and optical properties of halide perovskites and a brief review of the main application areas. More emphasis is given to inorganic perovskites which are the subject of study of my PhD. In particular, I illustrate what are the chemical composition and the main crystalline structures in which we can find this type of materials, focusing on the optical and electronic characteristics that make halide perovskite materials of interest for several optoelectronic applications. Then I focus on the main possible application of my work, i.e. the integration of halide perovskites in metasurfaces for photonics and photocatalysis.

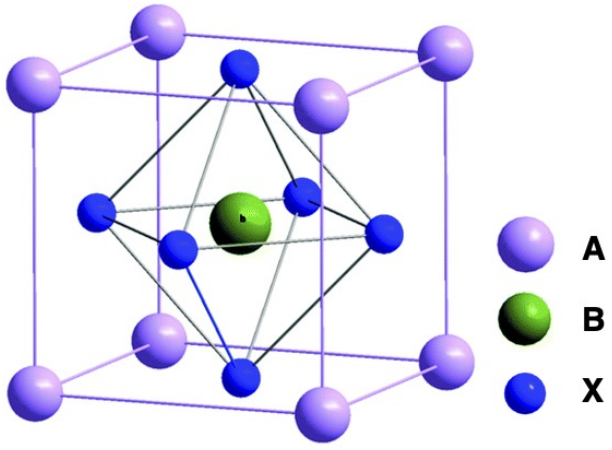

Figure 1.1. Atomic structure of perovskite ABX_3

1.1 Structure and optical properties of halide perovskites

The term "perovskite" primarily refers to the mineral made of calcium titanate ($CaTiO_3$). Discovered in 1839 in the Ural Mountains in Russia by Gustav Rose, the Perovskite name was attributed in honor to the Russian mineralogist Lev Aleksevich von Perovski [108]. Currently, the term is associated with all chemical compounds having the same crystalline structure as $CaTiO_3$. The chemical formula of perovskites is ABX_3 in which A and B are typically metal cations of different sizes while X is an anion. In the ideal structure of perovskites, B and X form octahedra types BX_6 in which B is placed in the center and X around B, as illustrated in Fig.1.1: each octahedron is connected to the others by sharing the X ion so as to form a three-dimensional structure. Cations A fill the cavities formed by adjacent BX_6 octahedra to balance the charge of the entire structure. In the elementary cell of the perovskite, ions A and B are arranged according to a centered cubic structure, with A ions at the vertices and B ions at the center, while X ions are arranged in the center of each side of the cube. Recent studies show that perovskites have mainly a cubic or pseudocubic structure but there are also other symmetries in which the crystal can be found [2]. Many materials in fact have a distorted orthorhombic structure at room temperature or even rhombohedral, hexagonal or tetragonal structures [16]. The perovskites studied in this work and of interest for the most innovative technological applications in the field of optoelectronics are perovskites of halides, that is where X can be chlorine, bromine or iodine (X = Cl, Br, I). From this moment on I will use the generic term perovskite to indicate only the perovskites of halides (hereafter indicated as HP). HPs are semiconductors with direct *band gap*, where the band gap is defined as the difference between the maximum of the valence band, VB (higher-energy electronic band occupied at T=0 K), and the minimum of the conduction band, CB (lowest energy electronic band not occupied at T=0 K). Depending on the chemical components (in particular the halogen anion), the energy of the band gap can vary between about 1.5 eV and 4 eV [129]. Therefore, many compounds with different optical properties and the same chemical structure (ABX_3) can be made from different elements. This extraordinary versatility has made HPs very interesting for many applications. Depending on the nature of cation A, halide perovskites are classified into hybrids or inorganics. In hybrid perovskites A is an organic group cation, such as methylammonium ($CH_3NH_3^+$, MA) or formamidium ($HC(NH_2)_2^+$, FA), while the most commonly used inorganic ion is caesium (Cs^+): the samples studied in this thesis work are caesium-based inorganic perovskites, in particular $CsPbBr_3$. Ion B is generally a bivalent metal (Pb^{2+}, Sn^{2+}, Ge^{2+}) and X a halogen (I, Br, Cl): the choice of the different elements that make up a perovskite depends on the type of application. Perovskites in which B is a lead ion, Pb^{2+}, have greater stability compared to tin, Sn^{2+}, and germanium, Ge^{2+}, although they are not optimized for solar cell applications; in fact it would be better to use tin as it would reduce the value of the gap, closer to the optimal values for solar cells (1.2÷1.4 eV for $MASnX_3$, 1.4÷1.8 eV for $MAPbX_3$) [21]. Among inorganic halide perovskites (hereafter indicated as IHP), the orthorhombic phase $CsSnI_3$ could be used in many applications as it has a band gap energy of 1.3 eV (solar cells, etc.) [22]. However, tin-based perovskites have lower optical properties than lead-based perovskites and in particular are much

more sensitive to temperature and humidity [78]. Stability and moisture sensitivity are two issues that researchers are deeply investigating to reduce the material ageing. In fact, with just 50% humidity in the air, these materials lose their properties and a rapid decrease in the performance of the electrical and optical characteristics is manifested. Carrying out my thesis, I witnessed a rapid degradation of some samples. In fact, although the right precautions were taken for their preservation in a controlled atmosphere and away from contaminants, during spectroscopic analysis, some of the samples showed typical symptoms of degradation. However, this allowed me to understand how and when these phenomena occur. As already mentioned, changing the halogen, the energy bandgap and therefore the absorption spectrum of the material are varied. In particular, proceeding from fluorine (F) towards iodine (I), that is, going down along the column of the VII group, in correspondence with the increase of the atomic radius, the absorption edge is moved towards greater wavelengths. The atomic radius of the elements constituting the perovskite plays a fundamental role in making an optically efficient and stable material. To predict the stability of the perovskite structure, two geometric parameters are typically used: the tolerance factor (t), introduced by Goldschmidt [44], and the octahedral factor (μ) [77]. The tolerance factor is expressed as the ratio of the bond distance A-X to the distance B-X in a cubic structure, defined as:

$$t = \frac{R_A + R_X}{\sqrt{2}(R_B + R_X)} \tag{1.1}$$

where R_A, R_B and R_X are, respectively, the radii of ions A, B and X. This provides a range of variability of the ionic radii in which the lattice shape remains cubic (for IHPs, $0.85 < t < 1$ is obtained). In the case of organic-inorganic hybrid perovskites, since the A ion is an organic cation, there is a variation in the bond length due to the hydrogen bond interaction and this makes difficult to define an ionic radius. To solve this problem, a rigid sphere model has been proposed [62, 61] to obtain an effective ionic radius for the molecular cation ($r_{A,eff}$), defined as:

$$r_{A,eff} = r_{mass} + r_{ion}. \tag{1.2}$$

Table 1.1. Ionic radii (in Å) of the most commonly used ions in perovskites. Effective radii are given for organic cations A (MA, FA) [21, 77].

A		**B**		**X**	
MA	2.17	Sn	1.1	I	2.2
FA	2.53	Pb	1.19	Br	1.96
Cs	1.67			Cl	1.81

In Eq.1.2, r_{mass} is the distance between the center of mass of the molecule and the atom, which is not hydrogen, with the greatest distance from the center of mass, while r_{ion} is the corresponding ionic radius of the atom. The ionic radii of the ions most commonly used in perovskites are reported in Tab.1.1: the effective radii of the molecular cations are reported for the organic cations A (MA, FA). As for the

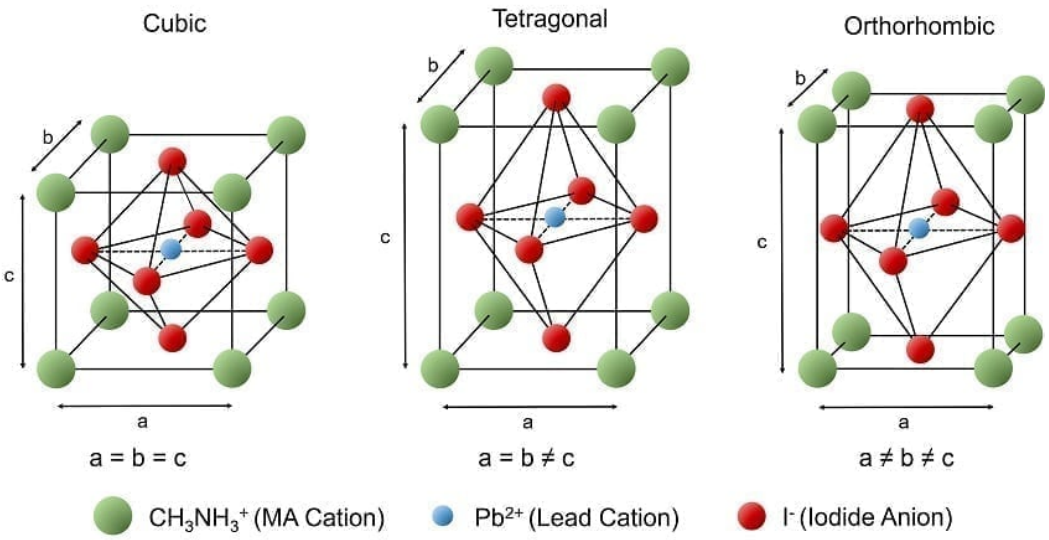

Figure 1.2. Crystalline phases of hybrid perovskite $CH_3NH_3PbI_3$

octahedral factor (μ), this is directly related to the BX_6 octahedron being defined as the ratio between the ionic radii of B and X:

$$\mu = \frac{R_B}{R_X} \tag{1.3}$$

For the HPs $\mu > 0.442$ while for lower values the formation of the perovskite does not take place as the BX_6 octahedron becomes highly unstable. However, these conditions are necessary but not sufficient for the formation of the perovskite to take place, given that the synthesis process also depends on other factors such as pressure and temperature which the geometric parameters do not take into account. In many cases distortions of symmetry are observed, giving rise to different crystalline phases. The most commonly observed crystalline phases are tetragonal and orthorhombic, shown in Fig.1.2 in comparison with cubic, for a hybrid perovskite $CH_3NH_3PbI_3$. Depending on the temperature, there are transitions between one crystal phase and another. In fact, temperature-dependent high resolution X-ray diffraction measurements have shown that $CH_3NH_3PbI_3$ is in an orthorhombic phase below 160 K; for temperatures between 160 K and room temperature it has a tetragonal phase while for temperatures above room temperature, the lattice structure is cubic. In the case of $CsPbBr_3$, the transition from the orthorhombic phase to the tetragonal phase was detected at 361 K, while the transition from the tetragonal phase to the cubic phase at 403 K [51]. Phase changes occur with a torsion of the octahedron BX_6 along the direction that minimizes electrostatic energy and maximizes the valence bond of cation A [151]. Again through diffraction measurements, it has been verified that these phase transitions are reversible [121] even though they can be incomplete [150].

The extraordinary interest in the inorganic perovskites of halides stems from the fact that their band gap energy falls in the visible range. Moreover, as already mentioned above, the band gap energy can be modified simply by replacing the halogen that makes up the perovskite, thus allowing to cover the entire visible

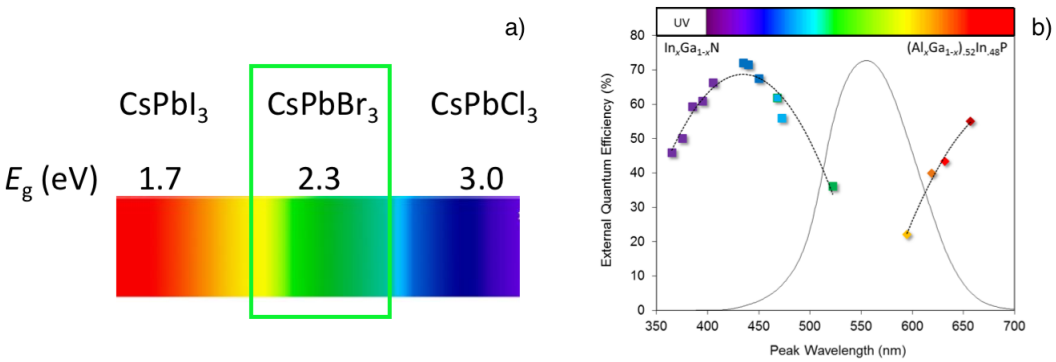

Figure 1.3. Band gap energies of inorganic perovskites $CsPbI_3$, $CsPbBr_3$ and $CsPbCl_3$ (a). Specifically the perovskite $CsPbBr_3$ has a band gap energy of ~ 2.3 eV. In (b) the External Quantum Efficiencies (EQE) are shown in relation to the emission wavelengths for the compounds of $In_xGa_{1-x}N$ and $(Al_xGa_{1-x})_{0.52}In_{0.48}P$. The continuous curve represents the emission spectrum of a compound $CsPbBr_{1-x}I_x$.

range, as shown in Fig.1.3(a). This makes them very interesting for the realization of light emitters such as LED and Laser throughout the visible spectrum. With conventional solid-state light emitters, for example based on InGaN, efficient emission at wavelengths between 450 nm and 750 nm is unlikely (Fig. 1.3(b)), since for this type of material, given the low miscibility of Indium (In), it is not possible to obtain a homogeneous alloy and micro/nano regions are formed in the material where the InN and GaN compounds are separated. The energy of the InN band gap is ~ 0.8 eV while that of GaN is ~ 3.5 eV. This means that the occurrence of variable composition aggregates strongly limits the use of $In_xGa_{1-x}N$, for x $>$ 0.2. With inorganic metal halide perovskites (IHP) (see Fig. 1.3(a)) an excellent homogeneity of both ternary and quaternary compounds is obtained, where two different halogens are used in varying proportions and therefore it is possible to cover the whole visible spectrum. In particular, $CsPbBr_3$ has a band gap energy of ~ 2.3 eV, which makes it perfect for making light emitters at wavelengths centered around 530 nm.

1.1.1 Band structure

The theoretical Density Functional calculation of the electronic properties of IHPs has been the subject of several studies [95, 149] in which the band structure is described by means of models using the method of functional density. In Fig.1.4(a) the band structure calculated for $CsPbBr_3$ is shown: the density of states of the valence band is generated by a hybridization of the Br orbitals, while for the conduction band the dominant contribution is given by the Cs orbitals. As from Fig.1.4(a), $CsPbBr_3$ is a direct band gap semiconductor and the maximum of the valence band and the minimum of the conduction band coincide in the R point of the Brillouin zone (Fig.1.4(a)). As mentioned above, if we consider compounds of the type $CsPbX_3$ (X = Cl, Br, I), depending on the halogen X, the energy bandgap E_g changes as reported in Tab.1.2.

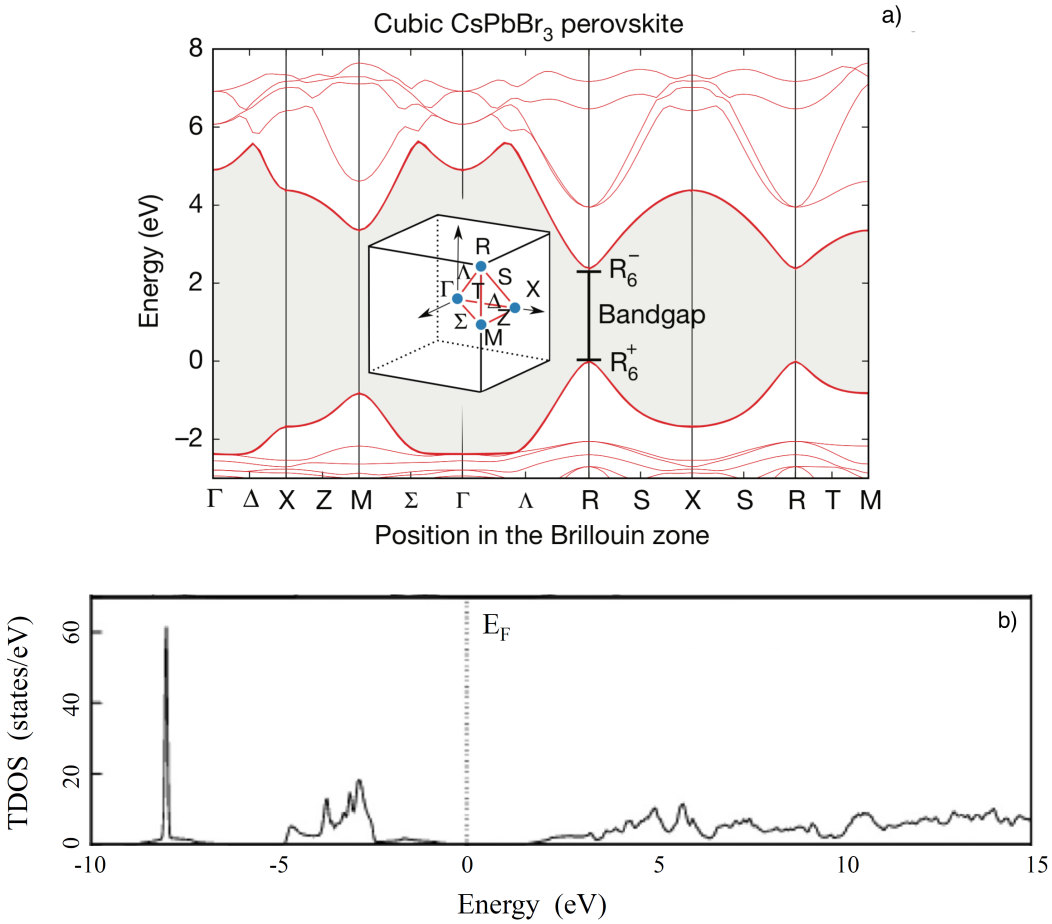

Figure 1.4. Representation of the band structure with its first Brillouin zone (a) and density of $CsPbBr_3$ cubic phase states TDOS (b).

Table 1.2. Measured band gap energy values (E_g) (at 300 K) for inorganic perovskites $CsPbCl_3$, $CsPbBr_3$ and $CsPbI_3$ [111, 25].

Perovskite	**E_g(eV)**
$CsPbCl_3$	3.0
$CsPbBr_3$	2.3
$CsPbI_3$	1.7

Role of composition

As from Tab. 1.2 E_g decreases changing the halide from Cl to I. This comes from the increase of the energy of the orbital states p of the halogen ion. Instead changing the ion A does not directly affect the energy of the band gap: what is altered with its size it is simply the volume of the lattice [71]. However, as the size of ion A increases, the structure, ideally cubic, can be distorted, so the strength of the B-X bond changes. Therefore, there is , indirectly, a variation in the energy gap due to this effect. In particular, it has been shown that a 3% variation in the initial parameters of the cubic lattice causes a change in the band gap energy of a few tenths of eV [45].

Role of temperature

In halide perovskites E_g significantly depends on the temperature. In particular, a peculiar feature of this class of semiconductors is the increase of E_g with the increase of temperature [24, 115, 69, 90, 80, 30, 134], opposite behavior to what commonly found in semiconductors [130].
In a semiconductor, the variation of E_g with temperature is due to two different contributions: the thermal expansion of the lattice, which produces a variation of the electronic levels, and the renormalization of the energies of the bands due to electron-phonon interaction [97]. In particular, the dependence of the band gap energy on temperature, at constant pressure, can be written as [97]:

$$\left(\frac{\partial E_g}{\partial T}\right)_P = \left(\frac{\partial E_g}{\partial T}\right)_V + \left(\frac{\partial E_g}{\partial lnV}\right)_P \left(\frac{\partial lnV}{\partial T}\right)_P \tag{1.4}$$

where the first term is responsible for the electron-phonon interaction and the second for thermal expansion. The term $\left(\frac{\partial lnV}{\partial T}\right)_P$ is the coefficient of thermal expansion of the volume. In many semiconductors the contribution of thermal expansion is negligible compared to that of phonon interaction and what is observed is a *red-shift* of E_g as the temperature increases [72]. On the contrary in HP the second term of Eq. 1.4, which can be both positive and negative depending on the structure of the electronic band, plays a fundamental role as the coefficient of thermal expansion (for example, $\approx 10^{-4}\ K^{-1}$ for MAPI [115]) is much higher than in other semiconductors such as silicon ($7 \cdot 10^{-6}\ K^{-1}$ [23]) or GaAs ($< 10^{-5}\ K^{-1}$ [118]). Due to the nature of the valence band, formed by a hybridization between the s atomic orbitals of the metal cation and the p orbitals of the halogen, the term $\left(\frac{\partial E_g}{\partial lnV}\right)_P$ will be positive for the perovskites [152]. Indeed, with the expansion of the lattice there is a reduction of this hybridization that produces a shift of the valence band towards lower energies [88] leading to an overall *blue-shift* of the band gap [24]. By increasing the temperature, if there are no crystalline phase transitions, the term coming from the phonon interaction becomes dominant, due to the population of optical phonon modes. For example, in $CsPbBr_3$, [134] a blue-shift (~ 0.3 meV K^{-1}) of the PL from 10 K to 220 K is observed, where the contribution of thermal expansion dominates, while at higher temperatures, the peak of PL approaches a constant value, due

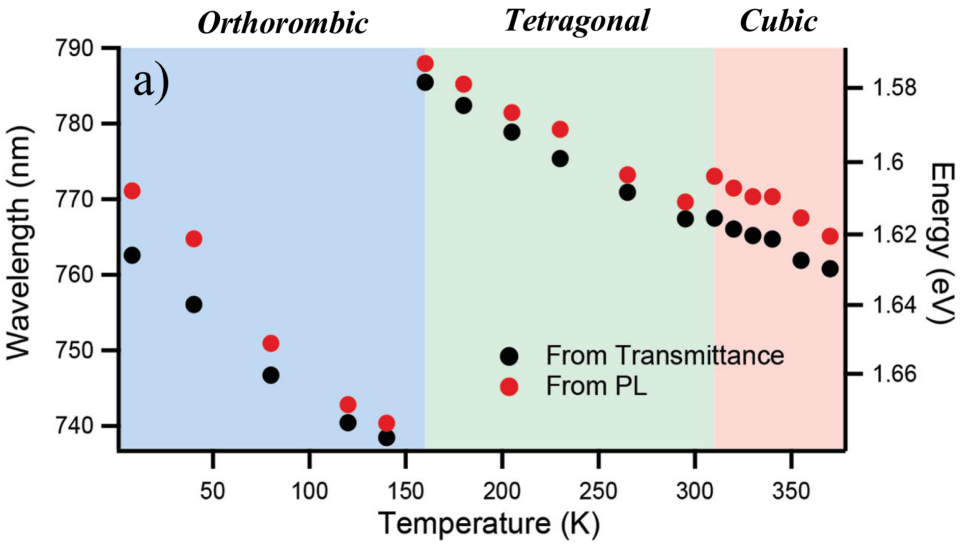

Figure 1.5. Wavelength (energy) of the of the absorption band *edge* and wavelength (energy) of the MAPI PL peak as a function of temperature extracted from the transmission spectra (in black) and the PL spectra (in red) [90].

to a much higher negative contribution than the term due to the electron-phonon interaction.

Role of the crystalline phase

As already mentioned, the energy of band gap also depends on the crystalline phase of the perovskite [24, 69, 30, 36]. For example, in MAPI it is observed that E_g is greater for the orthorhombic phase than the tetragonal phase, which is stable from 160 K (Fig. 1.5). In both crystal phases of MAPI, the band gap energy increases with temperature ($dE_g/dT = 0.3 \div 0.5$ meV K^{-1}[69]) and near the phase transition temperature there is a significant red-shift of *edge* of the band (about 100 meV) in the transmission spectrum, which marks the transition from the orthorhombic to the tetragonal phase.

1.2 Optoelectronic applications

The interest of the scientific community towards the perovskites of halides comes from the possible applications of these materials for the realization of innovative devices such as high-efficiency and low-cost photovoltaic cells [56], light emitters such as LEDs and Lasers [82], sensors [113] and radiation detectors [133]. In the photovoltaic field there has been a dramatic advancement in a short time, going from a photovoltaic conversion efficiency of $\sim 3.8\%$ at the beginning of 2009 up to values above 22 %, [66, 63, 144], in continuous growth [15, 76]. Therefore, if we compare the development of perovskites in this field with that of other types of materials (see Fig. 1.6) we observe that no other material has ever shown such

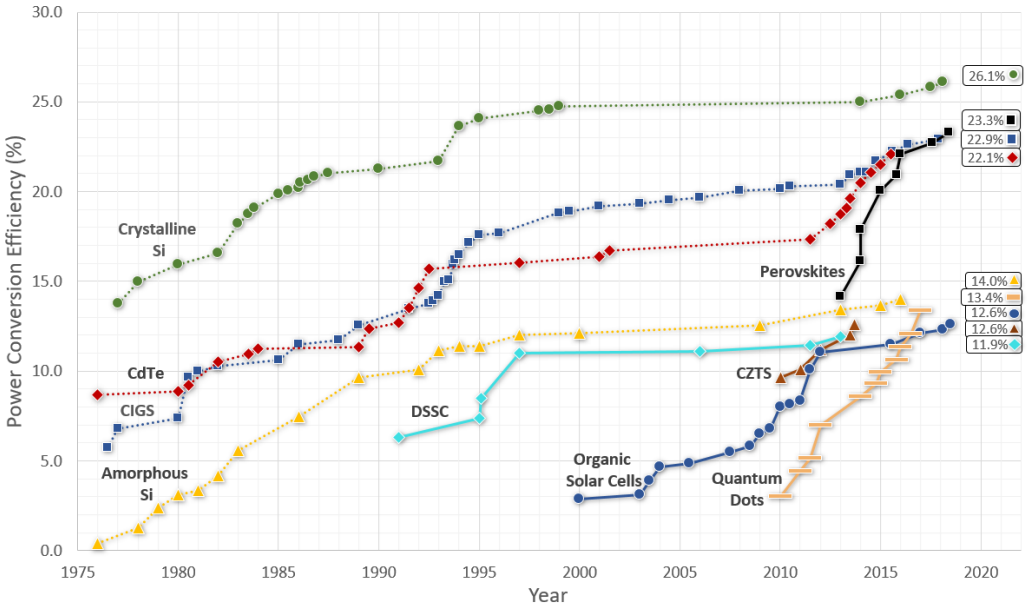

Figure 1.6. Trend of photovoltaic conversion efficiencies for different types of materials (www.ossila.com). For the perovskites (small black square in legend) the reported period goes from 2013 to 2018 [15, 76].

a rapid development in terms of efficiency for solar energy conversion. Until now, research has mainly focused on hybrid perovskites, despite the fact that the first observation of photoconductive response (1958) concerned an inorganic perovskite based on $CsPbBr_3$ [92]. In 2015, with the chemical synthesis of some $CsPbX_3$-based nanocrystals (X = Cl, Br, I) [103], the intensive study of inorganic metal halide perovskites was launched. The interest in these materials stems from the need to solve some problems regarding the hybrid perovskites, in particular the instability over a long period due to the interaction with external agents such as temperature, humidity and light [15]. These problems have been solved in part by the introduction of inorganic perovskites, which have the same optoelectronic properties as the hybrids but better stability [82].

1.2.1 Photovoltaic cells

As mentioned above, hybrid perovskites have been very successful in the photovoltaic field despite presenting a considerable ease of degradation in time [96] and a not perfect thermal stability [70]. In particular, comparing samples of $MAPbBr_3$ and samples of $CsPbBr_3$, synthesized with similar processes, the $MAPbBr_3$ shows, in thermal stability compared to the $CsPbBr_3$, a decrease of the short-circuit current, of the open circuit voltage and therefore of the efficiency on a timescale faster than the order of the thousand of hours [70, 89]. This behaviour is probably due to the greater interaction of the organic cation with the surrounding water vapour. Solar cells based on $CsPbI_3$ in various geometries were then made [33], which, although they showed rather low photovoltaic conversion efficiencies ($\sim 2\%$), are characterized by greater stability at room temperature than organic perovskites. Currently cells

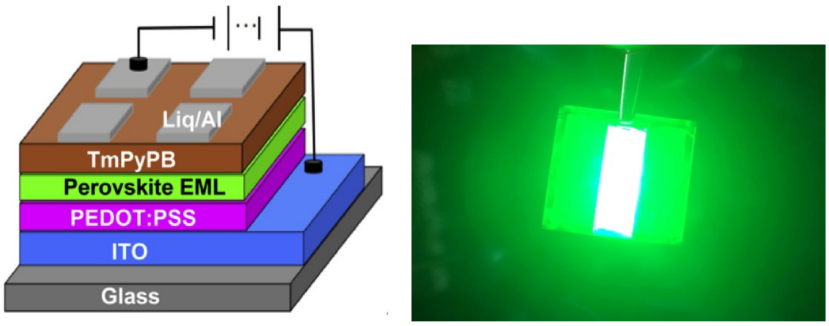

Figure 1.7. Typical multilayer structure of a $CsPbBr_3$ perovskite-based LED device and its output [84, 79].

with inorganic perovskites have efficiencies not exceeding $\sim 9.8\%$ [125], not yet comparable to cells based on hybrid perovskites.

1.2.2 Photodetectors

Inorganic perovskites are also used for the realization of photodetectors. In order to have good detectors it is necessary a high mobility of the charges and a quite long lifetime to allow the extraction of the charges before recombination. These properties have been observed in monocrystalline $CsPbBr_3$ through measurements of resistivity and photoconductivity [121]. In particular, the values obtained in these studies make these materials competitive with those typically used for the realization of photodetectors. $CsPbBr_3$ thin film detectors have achieved efficiencies of $\sim 40\%$ with rise and fall time of the signal in the millisecond range. To my knowledge, the best result, until now, has been obtained for a planar detector based on $CsPbBr_3$: the rise and fall times of the signal are of the order of μs [119] with a good contrast between current in the presence of signal and current in the dark ($\sim 10^3$). This application field is still in the development phase and the efficient light absorption and transport properties of these materials are very promising.

1.2.3 Light-emitters

As already mentioned, in halide perovskites it is possible to vary the direct bandgap energy simply changing the type of halogen that makes up the material, so a fine tuning of the absorption and emission spectra [103] can be realized to cover the whole visible range. This aspect makes them particularly suitable for applications such as light emitters, where they have been most successful.

The emission spectrum of a metal halide perovskite is characterized by a relatively small spectral width (≈ 30 nm) when compared with that of organic compounds used for OLED (≈ 70 nm), with a wide range of wavelengths obtainable and stable in time [103]: this allowed the development of LED devices [78, 120]. To improve the performance it is necessary to act on the current injection: this is possible working

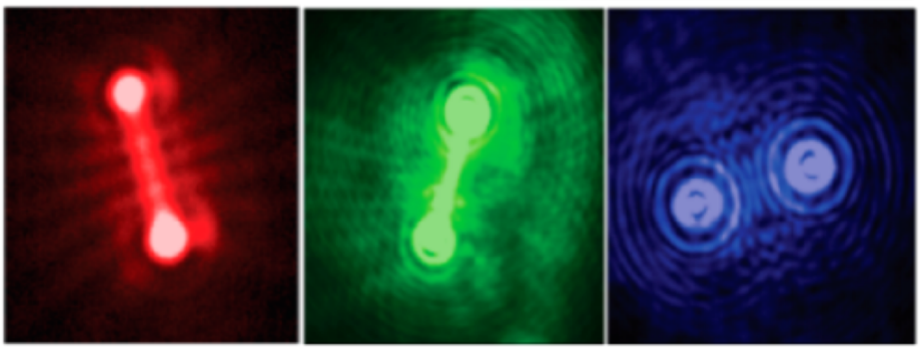

Figure 1.8. Images of laser emissions from inorganic perovskite-based nanowires [32, 38, 139].

on the design of the device and on the charge transport layers, which make up the device [107] (see Fig. 1.7). In order to obtain a LED device with good efficiency it is of great importance to limit the non-radiative recombination paths and this is possible by minimizing the presence of defects inside the material. Different protocols can be used for defect passivation [148]. LED devices have been manufactured with polycrystalline films and nanostructures (in particular quantum dots (QDs)) [147]. The use of homogeneous thin films facilitates the carrier transport; for this reason the research is aimed at the creation of homogeneous and compact films with increasingly cutting-edge deposition techniques, which we will discuss in the next chapters. In view of the realization of a light emitter, it is also important to understand the interaction between the active medium (perovskite) and the substrate on which it is deposited, as well as to define the thickness of the active medium needed to maximize the device efficiency. In this work, I present a study concerning the role of the deposition substrate with a focus on the relationship between substrate and optical properties. Considering lasers, the first experiments aimed at the realization of this type of device were conducted on hybrid perovskites, in particular those composed of methylammonium $CH_3NH_3^+$ [29, 156]. In 2004, the detection of stimulated emission at 77 K was reported in a sample consisting of a microcrystalline film of $CsPbBr_3$ [68, 67]. A review of recent results concerning the amplified spontaneous emission (ASE) in halide perovskites can be found in ref.[123]

In recent decades we have seen a research strong interest in the development of nano/micrometric size lasers that can be integrated into other devices. Also in this case it has been tried to realize this type of devices exploiting the optoelectronic properties of perovskites, therefore leading to the development of *nanowires* based on hybrid perovskites, which have shown a high efficiency [160]. With the rediscovery of inorganic perovskites, an attempt was made to implement nanowires to exploit the properties of these types of materials: the first reports refer to $CsPbBr_3$ and $CsPbCl_3$ [32, 38, 139] (see Fig. 1.8).

1.3 Light management at the nanoscale

In this section I will provide a brief overview on some aspects of nanophotonics which is a central topic in this thesis.

1.3.1 Metamaterials and Metasurfaces

In the last decades, Nanophotonics, the science that builds a close connection between optics and physics at the nanoscale, has received an enormous interest from a large community of researchers that includes physicists, material scientists and chemists. In fact, the fundamental requirement is to realise nano-objects where light can be confined and where light-matter interaction gives rise to new properties/ behaviors of interest for innovative devices. This ambitious objective requires a large spectrum of expertise, so explaining the interdisciplinary nature of this research. We commonly indicate as metamaterials and metasurfaces the proper assembly of nano-objects that can produce significant modification of the optical response of the material itself[53, 20]. At the initial stage, most of the research on metamaterials and metasurfaces focussed on metals, because of the presence of the surface plasmon resonances[11]. However, some limitations are inherent to the use of metals, in particular the high losses and more recently the interest was directed to the realisation of all dielectric metasurfaces, in particular resonators, because of the high refractive index, low optical losses, high potential for active functionalities, and large amount of techniques available for the their realisation. Halide perovskites which already found a lot of application in photovoltaics, LEDs, lasers and sensors are more and more considered for the realisation of nano-photonic platforms. In fact their optical properties (in particular the high luminescence yield and the high index of refraction) allow their use for realising metasurfaces or integrating them in dielectric metasurfaces [1]. Recent literature already reports on integration of halide perovskites in different kind of metasurfaces to exploit Purcell effect [8], broadband suppression of reflection [7], circular dichroism [86], etc. Moreover, non-linear effects are under investigation for realization of devices as fast modulators and saturable absorbers [159]. In this thesis I will show the integration of $CsPbBr_3$ in a metasurface realized with MIE microresonators, providing a significant enhancement of PL light diffusion and Amplified Spontaneous Emission.

1.3.2 T-Rex and related system

All-dielectric materials are emerging as a new class of substrates for enhanced Raman scattering. As ohmic losses are reduced in the absence of plasmonic metals, Raman data obtained with dielectrics are very reproducible and reliable. The system SiO_2/TiO_2 core/shell beads (*T-Rex*) are able to exploit the evanescent field generated by total internal reflection and multiple scattering light at the sphere-to-sphere interface to multiply the number of Raman photons, improving the sensitivity of Raman detection and extending the application of surface enhanced Raman scattering for investigating surface chemical reactions.

T-Rex spheres are made by the following procedure: a solution containing SiO_2 spheres is deposited on a Si substrate with drop-casting deposition technique. After

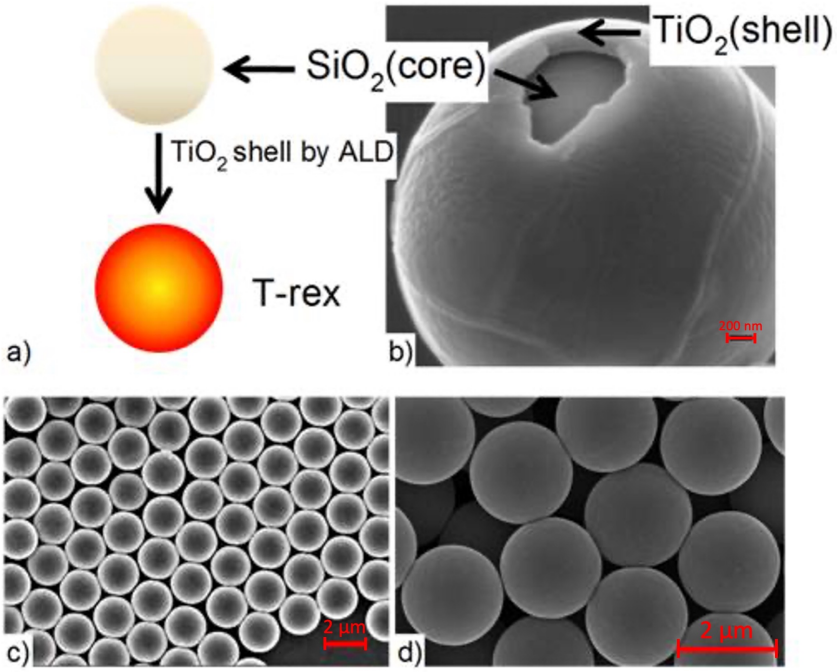

Figure 1.9. Typical structure of a *T-Rex* sphere (a, b). The spheres are deposited in multilayers packed according to a honeycomb pattern (c, d) [3].

solvent evaporation, SiO_2 spheres are covered by TiO_2 layer, through *Atomic Layer Deposition* (ALD) technique, forming the shell of the *T-Rex* following a core/shell SiO_2/TiO_2 configuration. In Fig.1.9(a, b) the *T-Rex* structure is shown. The size of the SiO_2 cores can be varied over a wide range (from tens *nm* to several μm), and the shell thickness is modulated accordingly, in order to obtain *T-Rex* beads with a given core/shell ratio. Most of the *T-Rex* beads utilized for Raman analysis are obtained from 2-µm-sized cores coated with shell layer with thicknesses varying from 25 to 100 nm. This is due to practical reasons, as 2-µm-sized beads can be directly observed with the optical microscopes that are commonly implemented in typical micro-Raman setups. As the laser beam size in this kind of apparatus does not exceed 2 µm, individual beads can be selected and analyzed separately, with major advantages from the analytical viewpoint. Moreover, core/shell single spheres offer an important option for exploiting Morphology-Dependent Resonances (MDRs). In particular, low-refractive-index core/high-refractive-index shell spheres allow the exciting light to be much more efficiently refocused and internally reflected within the sphere. As a consequence, intense, yet low-Q evanescent fields interrogate the surface sphere, giving rise to enhanced Raman signals. This effect can be observed in core/shell microspheres characterized by a strong refractive-index contrast between the core and shell. *T-Rex* represents striking examples of this behavior (Fig.1.10).

Examples of the application of *T-Rex* beads in detecting and monitoring environmental pollutants, greenhouse gases, biochemical species, and biochemical reactions are presented. The use of core/shell resonators for multi-modal analysis based on the combination of surface enhanced Raman scattering with either mass spectrometry or refractive index optical sensing is also discussed, suggesting different

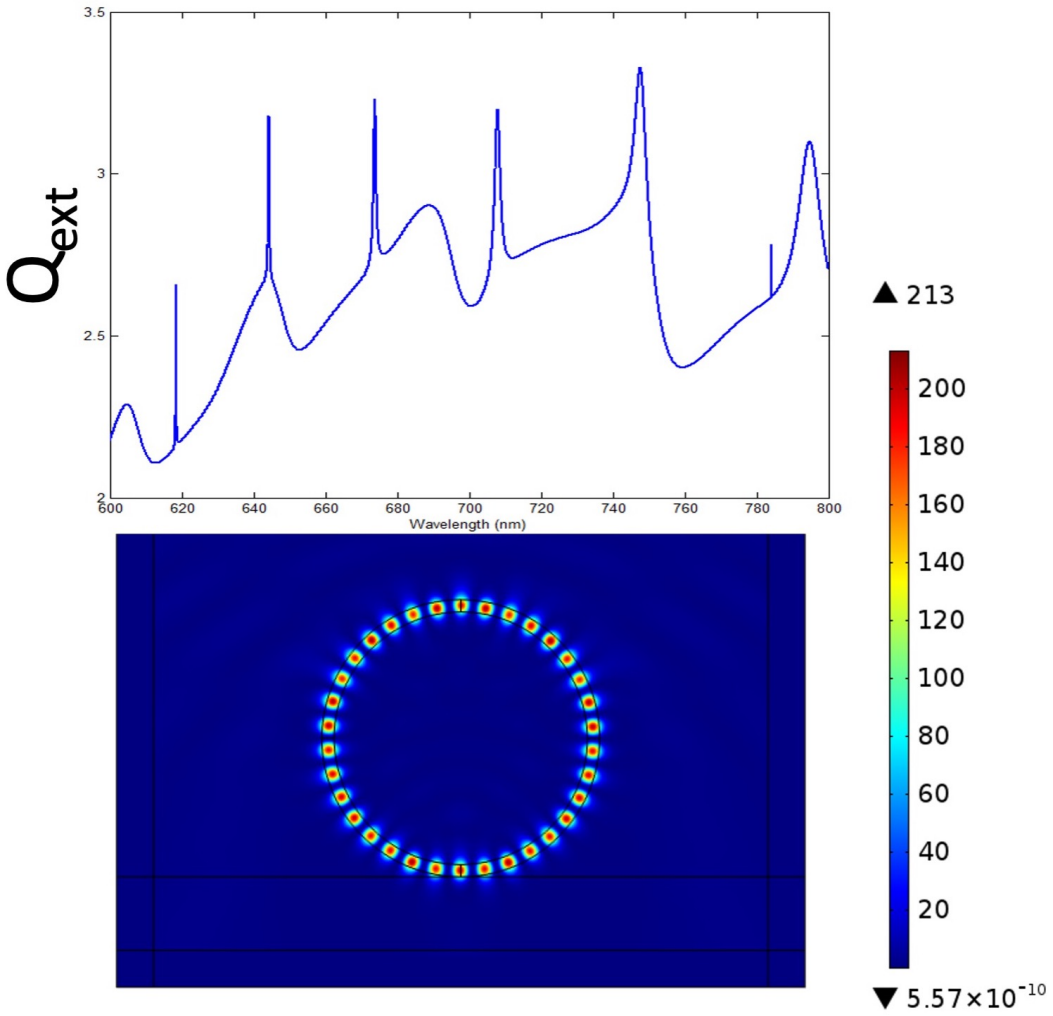

Figure 1.10. Mie-elastic-scattering-based simulations of MDRs for a SiO_2/TiO_2 core/shell microsphere [dcore(SiO_2) = 2 µm, shell thickness (TiO_2) = 100 nm] in air. Top: Q_{ext} vs λ. Bottom: Visualization of a specific MDR excited at 670 nm, indicated by an arrow. Credits: Dr. Luca Carletti and Prof. Costantino De Angelis (University of Brescia, Brescia, Italy) [4].

possible future developments. In particular, one of the most used applications is as resonators. Coating the low-index dielectric spheres with a high-index shell gives rise to core/shell systems characterized by a remarkable modification of their optical properties. The high-index coating induces light trapping within the sphere. Internal reflections generate optical cavities, whose quality factor (the ratio between the time averaged energy in the cavity and the energy loss for cycle) depends on the material utilized for the shell layer and its thickness.

Moreover, *T-Rex* beads offer a number of opportunities for Raman analysis as biomedical reaction monitoring, molecular recognition, environmental monitoring, gas sensing, multimodal analysis, detection of organic pollutants. It is worth noting that, unlike traditional plasmonic SERS, the main target of all-dielectric Raman amplifiers is not ultrasensitive detection yet reproducible monitoring of analytes and chemical reactions in real working conditions. In this regard, *T-Rex* beads are valuable complements to metal-assisted SERS, offering an alternative whenever metals cannot be applied. However, although the use of all-dielectric antennas for Raman purposes is still at its infancy, and there is still extensive room for improvement, the results achieved so far are relevant in terms of sensitivity and reproducibility.

In this thesis I aim to exploit the transport properties and optical conduction of *T-Rex* and combine them with the properties of absorption and emission of light radiation of perovskites, trying to obtain advantages regarding the spectral emission when compared with results obtained by the perovskite alone.

Detection of organic pollutants from water by *T-Rex* beads

It is right to dwell on the application of *T-Rex* for detection of organic pollutants from water. This is because the adsorption of pollutants from water is a topic that will be deepened in Chap.A and we will see the use of perovskite as adsorbers.

The first application of *T-Rex* was in detection of some organic pollutants, including thiazine-dyes such as Methylene Blue (MB), dissolved in water. This application exploits the high Raman reproducibility (relative standard deviation (RSD) well below 10%) exhibited by *T-Rex* beads and the possibility to combine evanescent field enhancement with the molecular resonances of the analytes. An important advantage of *T-Rex* relies on the photo- catalytic activity of the titania shell layer under ultraviolet (UV) irradiation. This allows to select specific *T-Rex* beads loaded with analytes, acquire the Raman spectra without the interference of plasmonic metals, and irradiate the beads with UV lamps or clean them with an ozone-UV cleaner treatment, in order to remove the analyte from the beads. Due to the thermal stability of TiO_2, most of the organic compounds can be removed also by fast thermal degradation without provoking phase transitions in the titania shell. In any case, at the end of those processes, the same *T-Rex* bead can be reused for further Raman analysis. Thus, different analytes or different stages of a reaction can be investigated using the same platform, which represents a key advantage for semiquantitative comparisons (Fig.1.11).

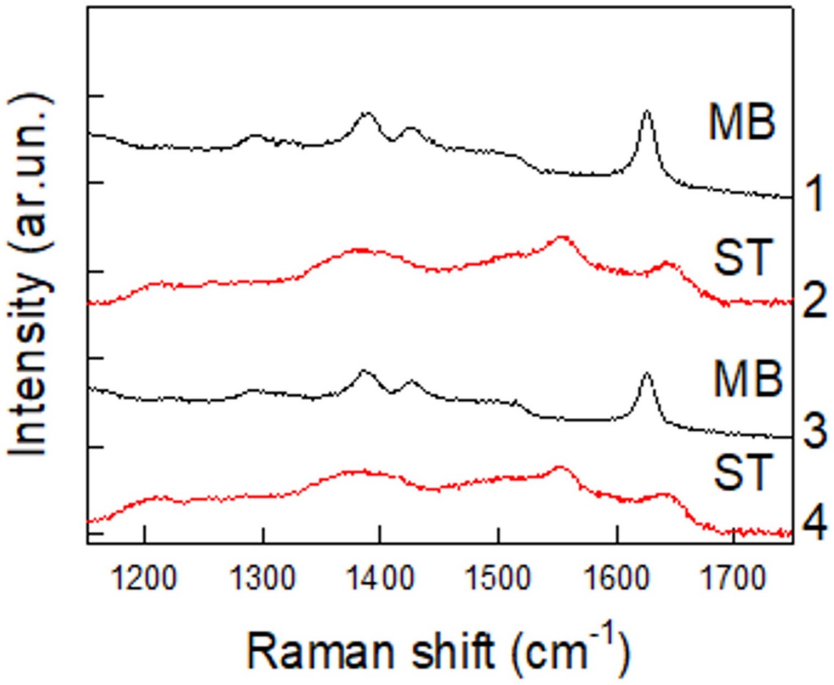

Figure 1.11. Example of recyclability tests carried out through different soaking-cleaning cycles. In each cycle 10^{-5} M solutions of either MB or ST dyes were alternatively adsorbed by a T-Rex100 sphere and subsequently removed by UV-cleaning and repeated rinsing in milliQ-grade water [3].

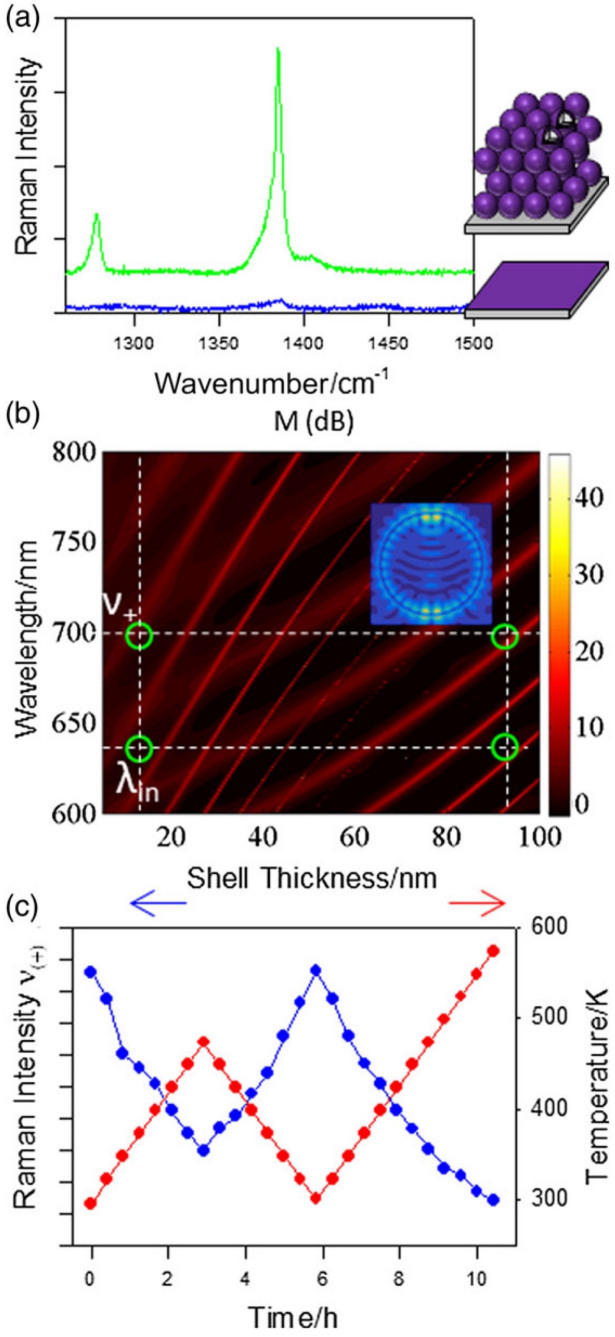

Figure 1.12. (a) Enhanced Raman detection of CO_2 adsorbed on *T-Rex* three-dimensional colloidal crystals. The CO_2 spectrum for a reference planar sample is shown for comparison; (b) Mie-scattering simulation-based maps of the optical resonance of individual *T-Rex* beads as a function of the shell thickness. An example of field distribution at resonance wavenumber is given in the inset; (c) use of *T-Rex* three-dimensional colloidal crystals for monitoring CO_2 variations as a function of different temperature sweeps. Adapted from Bontempi et al.[12] Copyright 2017 Royal Society of Chemistry

Gas sensor

Another important application is gas sensing. One of the objectives of this PhD thesis is to understand the interaction properties between *T-Rex* beads and perovskite in order to exploit these materials in gas sensing.

T-Rex beads offer interesting perspectives for Raman sensing of gaseous species. It is well known [3] that the Mie-type resonances of a *T-Rex* bead can be modulated by varying the core/shell thickness ratio (or, more practically, by changing the thickness of the shell layer for a given core size). Most of the gases that are interesting for environmental monitoring and food industry exhibit molecular vibrations in the 200- to 4,000- cm^{-1} range [58]. A proper adjustment of the shell layer thickness can tune the specific Mie-type resonances on the vibrational modes of a gaseous target, allowing to extract its signal from a mixture containing many other species, even in higher concentration (this is the typical situation of a sample of air, whose chemical composition is dominated by nitrogen and oxygen). In particular, *T-Rex* beads show a unique sensitivity to environmental carbon dioxide, which is adsorbed on the TiO_2 shell layer and can be easily detected using the Fermi dyads peaks at 1,285 and 1,388 cm^{-1} as a fingerprint (Fig.1.12(a)). *T-Rex* beads outperformed both titania reference thin films and nano-particles (e.g., P25 aerogels) in terms of sensitivity in CO_2 detection. It was demonstrated that the Raman response does not increase linearly as a function of the thickness of TiO_2 shell but follows an oscillatory trend that correlates with the presence of Mie-type resonances. Useful maps of these resonances as a function of the shell thickness can be obtained by Mie scattering-based numerical simulations, enabling the design of CO_2-sensitive resonators tailored on the wavelength of the laser utilized as a source for Raman excitation (Fig.1.12(b)). The simulations of the optical properties are in good agreement with the experimental results; thus, they can be extended to obtain qualitative predictions on the Raman response of other gaseous species. The use of 3D colloidal crystals is justified by their superior sensing performances, which are ultimately related to increased light trapping and multiple scattering. 3D crystals can be also exploited as sintered monolithic membrane for monitoring CO_2 at high operating temperature/pressure conditions, as those realized in exhaust systems or industrial plants. Experimental data of CO_2 adsorption sweeps as a function of the working temperature revealed an excellent stability of Raman data and no hysteresis over many adsorption/desorption cycles (Fig.1.12(c)). We note that the possibility to select different individual spheres and to follow their Raman response in situ upon changing temperature and CO_2 concentration allows to obtain data characterized by a very low standard deviation (<4%). The same approach utilized for CO_2 detection could be extended to other relevant gases, such as NO_x, NH_3, SO_x, ethylene, and acetone. Considering that *T-Rex* could be coupled in optical-fiber Raman sensors, exciting opportunities are envisioned for the selective detection of gaseous species in environmental matrices. Moreover as many critical reactions involved in generation of solar fuels (e.g., the photoreduction of CO_2, water splitting, and ammonia synthesis) pass through surface reactions of gaseous species adsorbed on a photocatalysts, *T-Rex* or analogous systems can be exploited as analytical platforms to investigate the reaction mechanisms and to monitor intermediate states and final products.

Chapter 2

Materials and methods

2.1 T-Rex synthesis

In this chapter I will describe the deposition techniques used in this thesis for the production of $CsPbBr_3$ samples on particular substrates. I will also present the experimental techniques used for sample characterization and the study of their properties. To a large extent, this PhD project focused on the integration and exploration of the properties of $CsPbBr_3$ thin films deposited on particular substrates formed by a metasurface having a core/shell SiO_2/TiO_2 microspheres deposited on a Si substrate. This metasurface is called *T-Rex* (TiO_2-based core/shell resonators) [131]. In particular, *T-Rex* beads are formed by a SiO_2 core with a TiO_2 shell. Starting from a Si substrate, 100/200 µl of SiO_2 microspheres are deposited by drop casting on the substrate and, once the solvent is dried, we can deposit a thin film of TiO_2, that form the shell of the beads, by means of *Atomic Layer Deposition*, hereafter indicated as ALD. In fact the TiO_2 layer surrounds the SiO_2 spheres forming the core/shell beads.

Typically *T-Rex* are used as micro-resonator [3], so the idea is to exploit the absorption/ emission/adsorption properties of perovskite and combine them with the transport properties of *T-Rex* to possibly enhance optical/sensing response of the perovskite itself. I have deposited $CsPbBr_3$ thin films on different substrates realized with different diameters of the *T-Rex* and with different deposition techniques in order to find the best match between perovskite crystals and the beads and to understand the optimal growth conditions. In particular, I have studied samples with spheres of different sizes. In Tab.2.1 the dimensions of *T-Rex* used are indicated, each of which has been deposited in 3 different dilutions on a silicon substrate, in order to obtain more or less concentrated single layer samples, and multilayer samples. Therefore, starting from the basic solution of SiO_2 beads, these were deposited in base concentration (D3) to obtain a multilayer; dilute 1:10 in water (D2) to obtain a concentrated single layer and dilute 1:100 (D1) in water to obtain a single layer. Then I deposited, by ALD, a TiO_2 film of different thicknesses (25÷100 nm) to form the shell of the T-Rex. Finally I deposited on top a film of $CsPbBr_3$. Different samples were prepared using spin-coating deposition, with dilution of precursor salt $PbBr_2$ of 0.17 M and 0.017 M, and Radio Frequency-Magnetron Sputtering (RF-MS). This also allowed us to understand which is the best deposition technique

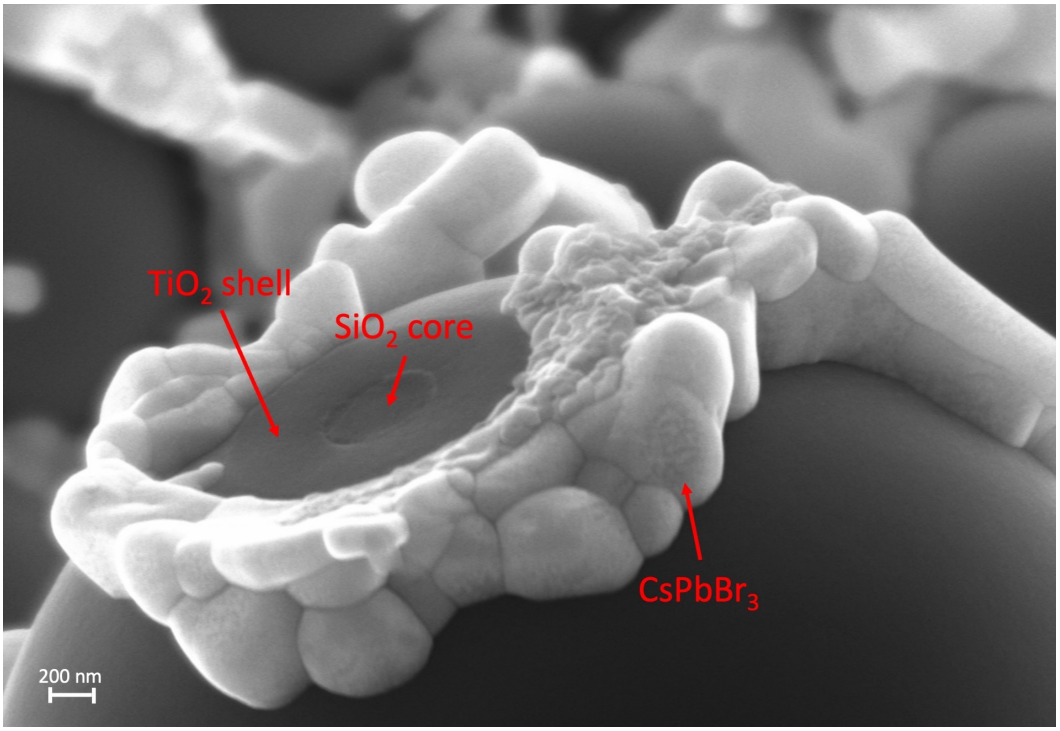

Figure 2.1. Image of a 6 µm diameter T-Rex sphere in which core, shell and $CsPbBr_3$ perovskite crystals can be observed.

and for which application to use it. The fig.2.1 shows the different parts of the

Table 2.1. Bead diameter (nm) and TiO_2 thickness (nm) of *T-Rex* nano/micro-spheres of the sample studied during my PhD.

Bead diameter (nm)	105	117	235	411	503	755	2000	6000
TiO_2 thickness (nm)	100	25÷100	25÷100	25÷100	100	25÷100	100	100

T-Rex sphere for a sample with 6 µm diameter spheres, 100 nm TiO_2 shell on which $CsPbBr_3$ was deposited by Spin-coating. The layer of TiO_2 is perfectly adapted to the shape of the sphere of core (SiO_2) creating precisely the *T-Rex* sphere; the perovskite crystallizes in nano/micro-crystals on and around the sphere. We will see later the differences in synthesis that occur depending on the deposition technique used for realizing the perovskite.

2.1.1 Atomic Layers Deposition ALD

Atomic layer deposition (ALD) is a thin-film deposition technique based on the sequential use of a gas-phase chemical process; it is a subclass of chemical vapour deposition. ALD is a key process in fabricating semiconductor devices, and part of the set of tools for nanomaterials synthesis. The majority of ALD reactions uses two chemicals called precursors (also called "reactants"). These precursors react with the surface of a material one at a time in a sequential, self-limiting, manner. A thin film

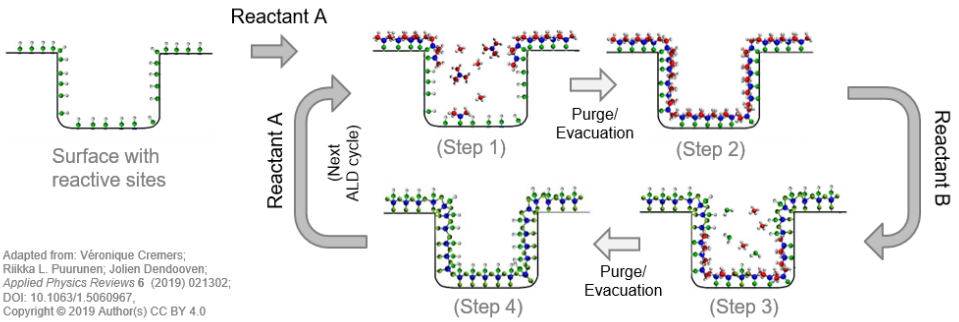

Figure 2.2. Schematic illustration of one reaction cycle of the ALD process, using the Tetrakis(dimethylamido)titanium TDMAT-water process to make thin titanium oxide films.

is slowly deposited through repeated exposure to separate precursors. Differently from chemical vapor deposition, the precursors are never present simultaneously in the reactor, but they are inserted as a series of sequential, non-overlapping pulses. In each of these pulses the precursor molecules react with the surface in a self-limiting way, so that the reaction terminates once all the reactive sites on the surface are consumed. Consequently, the maximum amount of material deposited on the surface after a single exposure to all of the precursors (a so-called ALD cycle) is determined by the nature of the precursor-surface interaction. By varying the number of cycles it is possible to grow materials uniformly and with high precision on arbitrarily complex and large substrates.

The growth is epitaxial so the deposition times can be very long: for this reason, this type of tool is typically used to deposit very thin layers. ALD is considered a deposition method with great potential for producing very thin, conformal films with control of the thickness and composition of the films possible at the atomic level.

By way of example, in fig.2.2 I show the operating diagram of ALD for the deposition of TiO_2 on the substrate. Our substrate, in this case, is Si on which the SiO_2 spheres have been previously deposited, with a certain dilution; each SiO_2 sphere will form the core of the *T-Rex* bead. The starting surface contains hydroxyls (OH groups) as reactive sites; step 1 is the reaction of TDMAT; step 2 is a purge or evacuation step, step 3 is the reaction of water, and step 4 is a purge or evacuation step. Then we choose the material to be deposited and place the sample inside a vacuum chamber ($\sim 5.5 \cdot 10^{-1}$ Torr in our case), we adjust the temperature of the chamber, precursors and system and we choose the exposure times of the precursors. The process takes place cyclically, opening and closing the exposure valves of the precursors for a few milliseconds (0.1 s for TiO_2 and 0.015 s for water). Between one step and another it is necessary to wait a few seconds so that the reaction takes place on the surface of the sample and the chosen material is deposited, in our case TiO_2. Based on the reaction cycles we can quantify the *nm* of material deposited on the sample and the process time.

What we get from this technique is the shell of the *T-Rex* spheres observed in fig.2.1 as the material during ALD deposition is perfectly adapted to the surface.

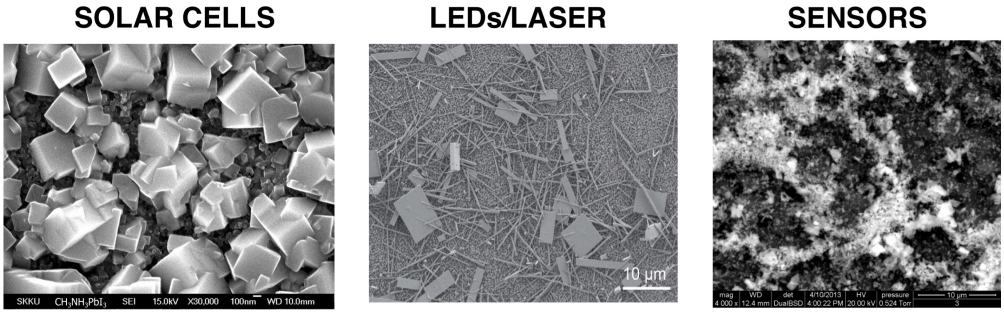

Figure 2.3. Morphology of some organic and inorganic perovskite samples used for solar cells, LEDs or Lasers and sensors.

Figure 2.4. Thin film deposition techniques of hybrid or inorganic perovskite from precursor salts dissolved in solution.

This type of deposition technique returns a much higher quality and homogeneity of the film than the common deposition techniques used for thin films. Of course the price to pay for this quality is the very long deposition time. In our case, the deposition of 25 nm of TiO_2 took 2 hours and a quarter (373 cycles) and for deposition of 100 nm of TiO_2 the process took almost 9 hours.

2.2 Samples preparation

The morphology of the sample has a fundamental role in the applications: depending on the device I want to realize, the perovskite has to have a very precise nano/micro structuring, as seen in Fig.2.3, for solar cell applications, LED, Laser and sensors. For this reason, the type of technique used for the sample realization is extremely important, as it defines its morphology. In the following paragraph I discuss a few techniques used in my PhD work for the realization of thin films of $CsPbBr_3$ deposited on different substrates and on different sizes of *T-Rex* beads, analysing their advantages and disadvantages compared to other deposition techniques.

2.2.1 Growth and deposition techniques

In order to realize a perovskite-based device, the choice of the growth and deposition technique is fundamental because different morphologies can be obtained (nano/microcrystals of different shapes, bulk crystals, nanowires, homogeneous films, etc.) each of which is used for different applications. In general, when we think of a device, the most commonly required morphology is that of a homogeneous

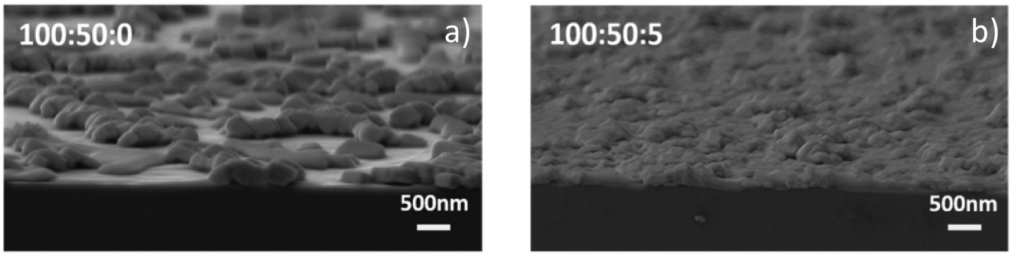

Figure 2.5. SEM images of a thin film of $CsPbBr_3$ deposited on glass-ITO through the spin-coating technique with perovskite concentrations:additives equal to $CsPbBr_3$:PEO:PVP = 100:50:0 (a) e $CsPbBr_3$:PEO:PVP = 100:50:5 (b) [81].

thin film. There are many aspects to consider when making a film to be used for device applications. Surely there is a need to check the characteristics of the material in terms of thickness, roughness, uniformity, distribution of crystalline grains, stoichiometry and the presence of defects. For device applications there is also a need to make homogeneous films over large areas. In addition, it would be of interest for the implementation of an optoelectronic device if the deposition technique allowed the doping of the material and the deposition of multilayers of different materials, in addition to the active layer, such as metals, layers used for the charge carrier collection/transport and electrodes. So far the most used techniques for the deposition of thin perovskite films are based on solutions of the precursor salts: for perovskites ABX_3, the precursor salts are AX and BX_2 dissolved in a solvent, for example DMSO (*Dimethylsulfoxide*). Starting from the solutions of the precursor salts, the film is made by deposition for *Blade-coating*, *Spray-coating*, *Dip-coating*, *Spin-coating* (see Fig. 2.4) [146, 99]. In the case of $CsPbBr_3$ the precursors are CsBr and $PbBr_2$ dissolved in DMSO. Spin-coating is currently the most widely used technique for laboratory sample preparation: the morphology and homogeneity of the film depend on the evaporation rate of the solvent and the wettability of the substrate. In particular, even if it is possible to obtain film thicknesses of tens of nanometers, the homogeneity of the film on macroscopic areas (mm^2) is very poor. Moreover, since deposition occurs normally in an uncontrolled atmosphere, the presence of defects can be significant. The samples in this case require further treatment of *thermal annealing* or the addition of polymer additives to improve their quality. Spin-coating remains a good technique for small laboratory samples. In Fig.2.5 we can observe the SEM (Scanning Electron Microscopy) images of a thin film of $CsPbBr_3$ deposited on glass-ITO, obtained by the spin-coating technique with the addition of additives PEO *PolyEthylene Oxide*) and PVP (*PolyVinyl Pyrrolidone*) in different concentrations. In particular, it is observed that the surface of the sample in the absence of PVP additives (Fig.2.5(a)) is strongly non-homogeneous while with the addition of PVP (Fig.2.5(b)) it is more uniform. This last sample was used for the realization of an LED device with *External Quantum Efficiency* EQE = 5.7 % based on $CsPbBr_3$, currently the best in the literature [81].

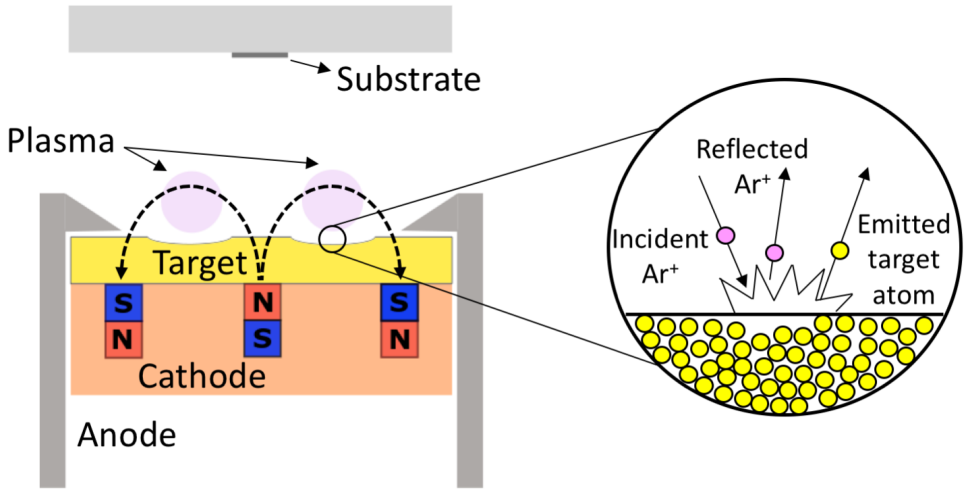

Figure 2.6. Section of the deposition chamber showing the working principle of an RF-MS process.

2.2.2 Radio-Frequency Magnetron Sputtering

The *Radio-Frequency Magnetron Sputtering* (RF-MS) technique was used for the realization of some samples in this PhD project. Sputtering ia a physical deposition technique well known for the deposition of metallic films but used for the first time for the deposition of thin perovskite films by the research group of Prof.ssa Anna Vinattieri at the laboratories of the University of Florence together with researchers of the Department of Chemistry of the University of Florence [46, 14], with whom I collaborated on my PhD project. The homogeneity of the samples resulting from the use of this technique is higher than that obtained by deposition by other deposition techniques. The advantages of this technique are many:

- allows the production of homogeneous samples over large areas
- allows to grow high quality multilayers with nanometer control of the thickness and roughness of the surface
- the samples are deposited inside a controlled atmosphere chamber, thus limiting contamination by external agents
- deposition takes place at room temperature limiting the stress between material and substrate
- allows a remarkable ease of doping of the material through the possibility of depositing from multiple targets of different material
- also allows deposition by *reactive sputtering*, that is in the atmosphere of nitrogen or oxygen reacting with the material.

RF-MS is classified as a *Physical Vapor Deposition* (PVD) and is mainly used to deposit metals, alloys, composite fabrics and other materials with a thickness up to 5

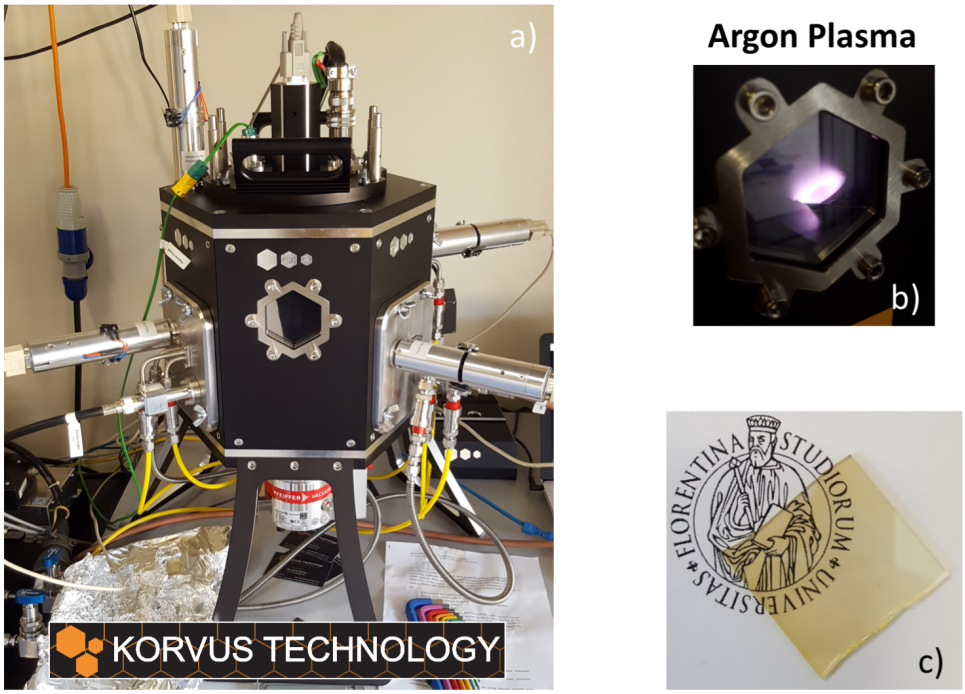

Figure 2.7. RF-MS used for the realization of the samples studied in this thesis work (a); Argon ion plasma (Ar^+) created inside the chamber of the RF-MS (b); Example of a sample of $CsPbBr_3$ obtained through the technique of the RF-MS (c) at the University of Florence.

μm. In textile coatings, it is used to coat fabrics with metals to provide antimicrobial, antistatic and electroconductive properties. In Fig.2.6 the working principle of the Magnetron Sputtering Radio-Frequency is shown. Inside a low-pressure controlled atmosphere chamber, a target or precursor metal (*target*), which we want to deposit on a substrate, is bombarded with inert gas energy ions (e.g. Argon or Helium), which form a plasma inside the chamber, accelerated through a collision process with electrons themselves accelerated by an electric field. The applied electric field can be continuous or a radio frequency, but it is preferable the application of a radio-frequency field to avoid that near the target a spatial charging region is created. For dielectric deposition the use of the radio-frequency is mandatory. The collision of the ions with the target produces the expulsion of the atoms of the target, which are projected throughout the chamber and in particular on the substrate, thus forming a film. During the process it is advisable to maintain the correct pressure and temperature conditions in order to maximize the energy of the ions of the inert gas, which act as a real *chisel*, but avoiding that these are implanted in the target reducing the extraction efficiency and introducing defects in the deposited material. In particular, the pressure inside the chamber and the energy of the ions play a fundamental role: in fact, the nanometric or micrometric grain of the film (fine or coarse) and the adhesion to the substrate are based on these two factors. The presence of the magnetic field allows to act on the electrons through the Lorentz force, making them spatially confined in an area close to the target, thus increasing the density of interaction between electrons and ions, then between ions and target. This increases the efficiency of the whole process compared to the classic *Sputtering*, in which there is no magnetic field. A wide range of film materials can be used, such as metals and/or semiconductors including silver, copper, brass, titanium, silicon, silicon nitride and carbon nitride.

Experimental details of the RF-MS deposition

To obtain the film of $CsPbBr_3$, the target is prepared from the precursor salts (CsBr and $PbBr_2$) in equimolar ratio. These salts are finely ground and compressed to form a tablet a few millimeters thick (3÷6 mm) and 5 cm in diameter. The deposition of the samples was performed in a single step, with a single target, with a *Korvus HEX Magnetron Sputtering* equipped with a radio frequency source working at 13.56 MHz (see Fig.2.7(a)). The deposition was performed at room temperature, on a rotating substrate, with a working pressure of 0.2 Pa and the power of the radio frequency source was set to 20 W. The deposition rate was adjusted to 0.07 nm s^{-1} and the final thickness of the samples has been fixed and monitored through a micro quartz crystal balance. In general, the instrument is equipped with three inputs in which it is possible to insert metal arms on which is placed the material to deposit. Two of the three inputs work with direct current while one in radio frequency. In our case only the radio frequency source was used. In Fig.2.7(b) the plasma of Ar^+ that is created inside the chamber during the deposition is shown. With this deposition technique, $CsPbBr_3$ was deposited directly on different substrates as soda lime glass, amorphous quartz, silicon and sapphire. Besides, a film was also deposited on a *T-Rex* substrate showing a good homogeneity of the film, as reported in fig.2.8 where the SEM image refers to a sample with 2 µm *T-Rex*, covered with $CsPbBr_3$.

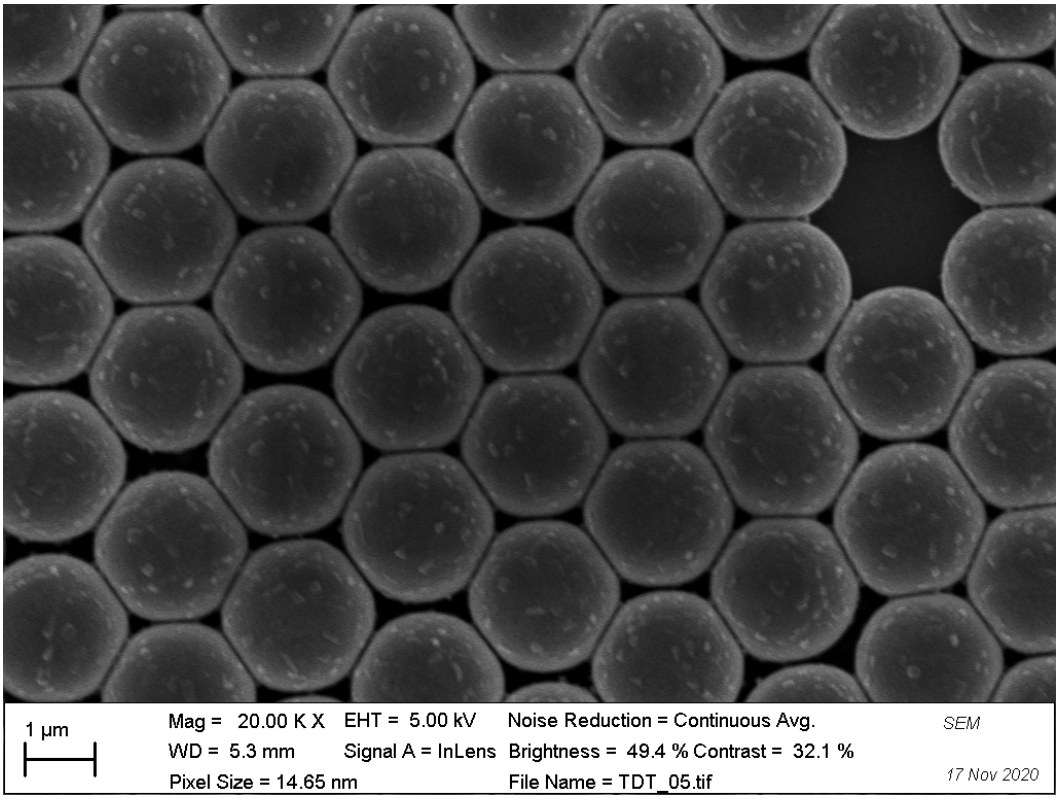

Figure 2.8. SEM image of 2 µm *T-Rex* sample with $CsPbBr_3$ deposited by RF-MS.

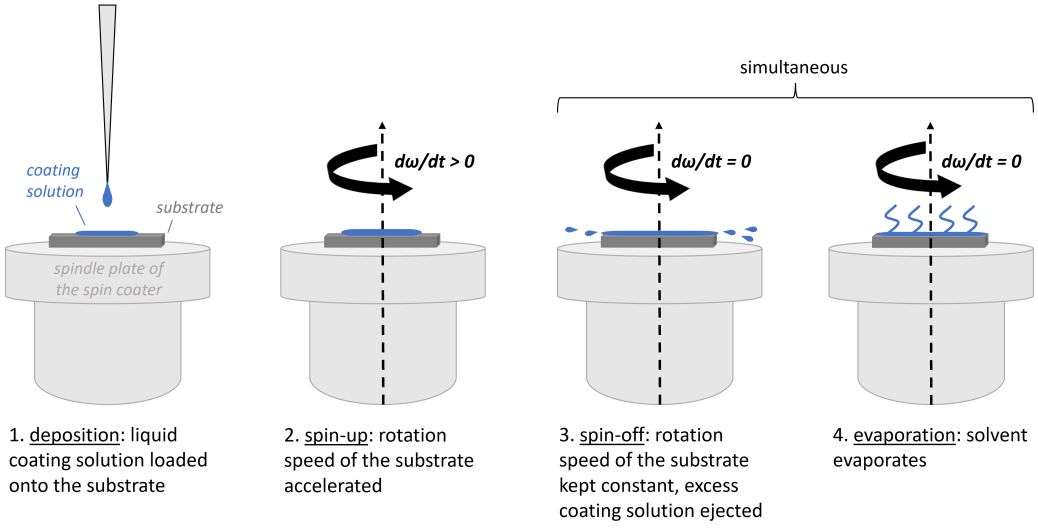

Figure 2.9. Diagram of the operation of a spin-coating.

With RF-MS the perovskite crystallizes in small crystals on top of the spheres covering the whole surface. This growth of crystals is different from that obtained with other types of deposition techniques such as *Spin-Coating*, as I will show in the followings. Therefore the deposition/growth technique used is of considerable importance depending on the application of interest.

2.2.3 Spin-Coating

Spin-coating is a procedure used to deposit uniform thin films onto flat substrates. Usually a small amount of coating material is applied on the center of the substrate, which is either spinning at low speed or not spinning at all. The substrate is then rotated to spread the coating material by centrifugal force. The solvents used are usually very volatile, so the film thins during the process also due to the evaporation of the solvent. The higher the angular speed of spinning, the thinner the film. The thickness of the film also depends on the viscosity and concentration of the solution, and the solvent. Rotation is stopped as soon as the desired thickness is reached, which can go below 10 nm. The machine used for spin-coating is called a spin-coater, or simply spinner.

The substrate on which we want to deposit the solution is anchored to the rotating disk of the spin coater, the pressure is lowered by a small vacuum pump and everything is then covered to avoid solution dispersion in the environment. In particular, the spin-coating process is generally divided into five main phases:

- **Deposition of the solution on the substrate**: this can be done by using a pipette that deposits a few drops of the solution or by spraying it onto the substrate surface first or during the rotation. Usually an excess amount of solution is used because during the rotation of the spinner a lot of material is expelled.

- **Substrate acceleration up to the chosen rotation speed**: this phase is

characterized by the expulsion of excess liquid.

- **Rotation of the substrate at constant speed**: the solution layer gradually thins due to the centrifugal force, which is counteracted by the force due to viscosity. The fluid motion on the substrate is now laminar with a low flow rate. The thermal conduction within the fluid occurs mainly by convection.
- **Evaporation**: at this point, the forces of the viscous type increase rapidly due to the gradual evaporation of the solvent, until they counterbalance the centrifugal force and the film thinning ends.
- **Substrate deceleration**: the deposition process has taken place and all the excess material has been expelled, the rotating disc on which the substrate is anchored decelerates gradually until it stops.

The parameters that can be set in the spin-coater are the rotor acceleration and deceleration (rpm/s) of the plate, the rotation speed (rpm) that represents the constant speed at which the anchor plate rotates, and the time (s) within which to rotate the plate. All these parameters allow to define the thickness of the deposited film.

The advantages in using this deposition technique are:

- Production costs, in addition to those of buying/operating a spin-coater are relatively low.
- Fast growth procedure respect to epitaxial growth techniques (like ALD) used for semiconductors and respect to RF-MS.
- Easy control of the chemical composition of the material. Unlike RF-MS, there is more control over where to deposit material as well as less material waste.
- Deposition parameters (solvent, temperature, spinning velocity/acceleration, substrate wettability, etc.) define the sample morphology. So by adjusting the parameters we can directly act on the deposition of the material.

Compared to other deposition techniques however, the spin-coater also has disadvantages:

- Scarce control of the homogeneity over several cm^2. In fact, being the deposition rather rapid with respect to the deposition for epitaxial growth or to the RF-MS, this rate of growth results in poor control of the homogeneity of the deposited film.
- Significant presence of traps and defects requires annealing. As already stated, the lack of homogeneity control leads to the inexorable emergence of defects in the sample.

Therefore, all this implies that the choice of the deposition technique used is of considerable importance both depending on the quality of the film we want to obtain, and with regard to the choice of timing that we should necessarily take into account for the realization of the samples. It is all about understanding what kind of application the material is designed for.

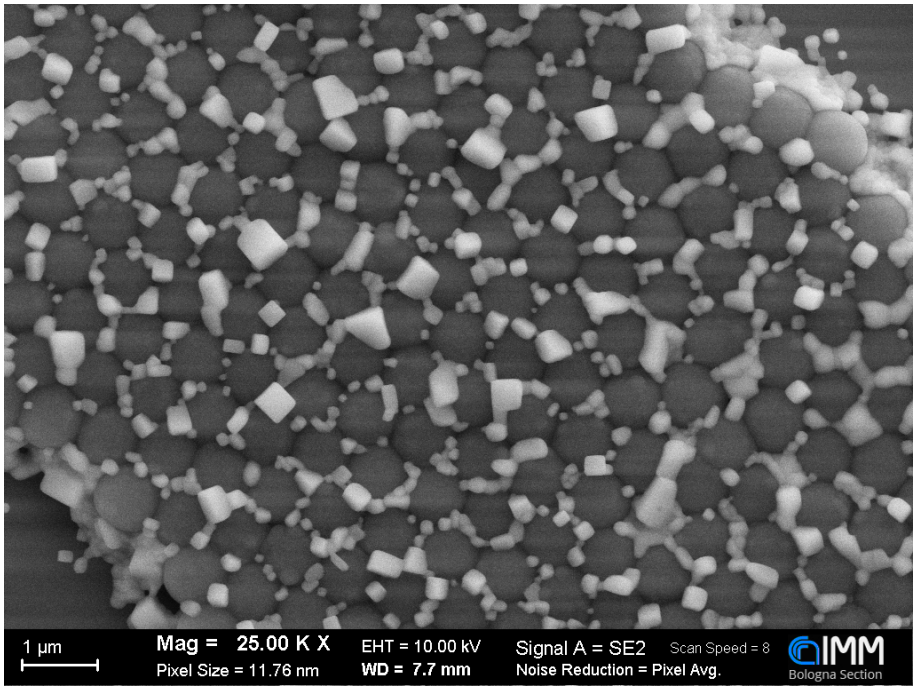

Figure 2.10. SEM image of *T-Rex* sample (diameter 755 nm; TiO_2 shell 100 nm) with $CsPbBr_3$ crystals.

2.2.4 Sample preparation

I now describe the protocol used for the deposition of $CsPbBr_3$ on *T-Rex* spheres using the spinner. I will discuss the preparation of films by magnetron sputtering in Chapter 3. Once the *T-Rex* substrate has been obtained, deposited on Si and fixed a suitable shell thickness ranging between 25 nm and 100 nm, the perovskite is deposited directly on the substrate. For the synthesis of $CsPbBr_3$ we start from the precursors $PbBr_2$ and CsBr dissolved respectively in *Dymethilformammide* (DMF) and Methanol (MeOH). In particular, 0.17M of $PbBr_2$ is dissolved in DMF and heated to 75 °C. By pipetting, 100/200 µl of $PbBr_2$ are deposited on the substrate once it is anchored to the vacuum system of the Spin-coater. Then, the chamber is closed and the Spin-coater is activated by inserting the parameters (speed of spin 2500 rmp, acceleration of spin 300 rpm/s, time 40 s). After deposition of the precursor $PbBr_2$/DMF, the sample is dried at 75 °C for 30 min in a heater. It is then immersed in a solution of 0.035 M CsBr, dissolved in MeOH at 50 °C, for 15 min and then rinsed in 2-Propanol and dried at 150 °C for 30 min. In this way, the crystallization of perovskite is in crystals of different sizes that settle between and above the T-Rex spheres, creating a connection between the spheres as show in Fig. for a *T-Rex* sample (diameter 755 nm; TiO_2 shell 100 nm) on which $CsPbBr_3$ was deposited by spin-coating.

2.2.5 Samples morphological and structural characterization

Several are the techniques that can be used to characterize the sample morphology and structure. It is also worth mentioning that it can be necessary to verify the

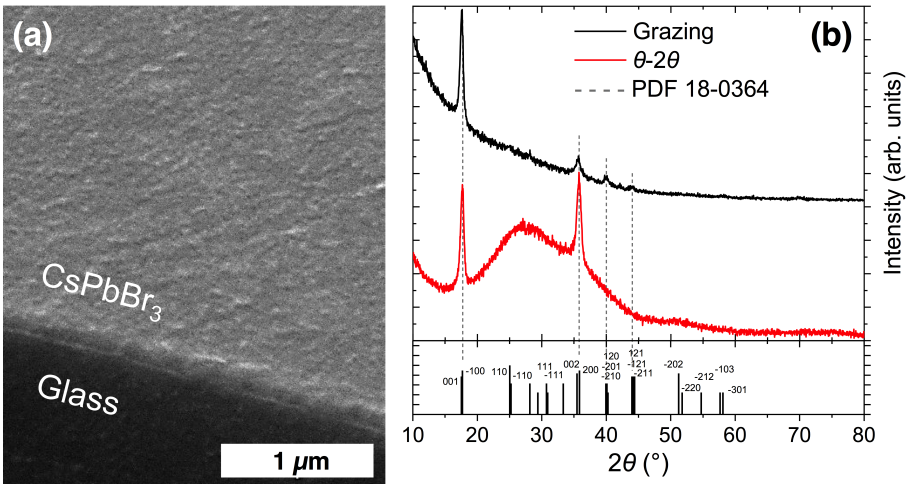

Figure 2.11. SEM image of a 140 nm film of $CsPbBr_3$ deposited by RF-MS on a soda lime glass (a). XRD of the same sample in two configurations (in black grazing incidence) compared with the XRD card (b). From ref.[34].

sample stechiometry and X-ray Photoemission Spectroscopy (XPS) is a commonly used technique, even though it provides only information on the first few nanometers below the surface. All samples presented in Chapter 3 were studied by XPS: the experiments were done by coworkers in the Department of Chemistry of the University of Florence. X-Ray spectra were measured by collaborators at the University of Florence and Trento to assess the crystallinity of the samples. SEM analysis was performed at the University of Florence and by collaborators at the Institute for Microelectronics and Microsystems (IMM) in Bologna.

In Fig.2.10 a SEM image of a sample where $CsPbBr_3$ has been spinned on the *T-Rex* beads is presented.

In Fig.2.11 I report the SEM image (a) of a $CsPbBr_3$ thin film prepared by radio-frequency magnetron sputtering along with the XRD spectrum (b) realized in a standard θ-2θ configuration and in a grazing incidence condition (red line): in this case the broad peak comes from the amorphous substrate. The comparison with the XRD card for $CsPbBr_3$ is shown.

2.3 Photoluminescence spectroscopy

The study of the optical properties of samples, presented in the thesis, was carried out using photoluminescence spectroscopy (PL). In this section I will introduce this technique explaining what physical information can be obtained. In the following section I will present the experimental setups used for the different experiments of photoluminescence.

Photoluminescence spectroscopy is an experimental technique widely used to investigate the optical properties of a semiconductor. It consists of exciting the sample by photons having energy E_{ph} equal to or greater than the band gap energy (E_g) of the semiconductor and in detecting the light emitted from the radiative recombination of the photoexcited carriers. In the case of non-resonant excitation

(E_{ph}>E_g) electrons and holes are excited with an energy greater than the minimum (maximum) of the conduction (valence) band. These carriers are in an excited state and typically relax towards the bottom of the band before recombining, losing their energy through phonon emission and capture by defects, if present. The carrier relaxation can be described by four regimes that occur at different time scales. The *Coherent regime* (time-scale typically shorter than the picosecond) is characterized by a well-defined phase relationship between the polarization produced by the excitation and the electromagnetic field that creates the excitation. The carrier-carrier scattering is the main responsible for the phase relaxation, which typically occurs in a very fast time scale (sub-picosecond), and which leads to the *non-thermal regime* in which the carrier distribution is nonthermal, therefore not describable by means of an equilibrium statistics. The non-thermal regime, which takes place on time scales varying between a few ps and tens of ps, is characterized by processes of carrier-carrier scattering and optical electron-phonon scattering that leads the non-thermal distribution to a thermal distribution (*hot carriers regime*). In this regime (duration 10÷100 ps) the carriers are thermalized, but the temperature is higher than that of the lattice. Finally, the carriers reach the lattice temperature by losing energy through scattering processes with acoustic and optical phonons; all carriers will be in thermal equilibrium with the lattice, but there will be an excess of electrons or holes with respect to thermodynamic equilibrium. During the relaxation path carriers can form excitons and also be captured by defects. Once reached the *isothermal regime* (typically longer than 100 ps) the free carriers and excitons recombine and return the semiconductor to thermodynamic equilibrium. It should be noted that there is no clear separation between the different regimes which also occur in a shorter or longer time frame than previously discussed depending on the type of semiconductor (e.g. carrier-phonon interaction strongly depends on the semiconductor and it can be different for *bulk* and nanostructures).

2.3.1 Recombination processes

The recombination of charge carriers can be either *radiative* or *non-radiative*. Non-radiative recombination processes are generally due to lattice defects that act as capture centers and do not lead to photon emission. On the contrary, radiative recombination processes lead to the emission of photons, giving rise to the photoluminescence signal.
The most important radiative recombination processes in a direct band gap semiconductor are:

- Recombination of electron-hole pairs. If the recombination between electrons and holes occurs at the bottom of the bands, the photon energy will be equivalent to the band-gap energy (E_g).
- Recombination of free excitons. Excitons are electron and hole pair bounded by the Coulomb interaction: in this case the energy of the emitted photon is:

$$h\nu = E_g - E_x \tag{2.1}$$

  where E_x is the exciton binding energy. In halide perovskites the exciton binding energy is few tens of meV, therefore excitonic effects are relevant also

near/at room temperature. Moreover when nanostructures are considered, due to confinement, E_x increases. [6].

- Bound exciton recombination. Excitons can bound to defects/impurities: therefore another contribution has to be considered due to the localization energy. In this case
$$h\nu = E_g - E_x - E_b \tag{2.2}$$
where E_b is the exciton binding energy to the impurity. Typically E_b is few meV when shallow impurities are considered.

- Recombination of carriers bounded to defects.

- Phonon replicas of the various types of recombination listed above, which are due to radiative recombination, assisted by the emission of one or more longitudinal optical phonons (LO). These emissions are at lower energies than the main recombination and are equally spaced by an amount equal to the LO phonon energy ($\hbar\omega_{LO}$). So the energy of the n-th phonon replication (E_{nLO}) is:
$$E_{nLO} = E_0 - n\hbar\omega_{LO} \tag{2.3}$$
where E_0 is the main energy and n the number of photons emitted in this process. Phonon replica are mainly observed at low temperature in polar materials where the carrier-phonon interaction is strong.

Non-radiative recombination, generally due to defects or Auger processes, becomes dominant as the sample temperature increases. Therefore, from low temperature to high temperature we commonly observe a *thermal quenching* of the PL. This quenching stays commonly with a decrease of the PL lifetime as measured by time-resolved PL spectra. It is worth noting that the quenching of PL can originate from: 1) a loss of population in the radiative states that not produce a change in the PL lifetime if carriers are lost in the relaxation path before recombination, 2) non-radiative recombination channels which act in parallel to the radiative recombination. In Chapter 3 I will present a detailed investigation of the dependence of the main PL characteristics (lineshape, intensity, time decay) obtained for the samples studied during my PhD with a specific focus on the characteristics of the Urbach tail in thin films. In Chapter 4 PL spectroscopy is used to investigate the radiative emission when $CsPbBr_3$ microcrystals are coupled to the *T-Rex* resonators.

2.4 Experimental Setup

In this section I will describe the experimental setups used to measure the optical properties of perovskite samples through *macro-photoluminescence* experiments (macro-PL), including *time-integrated photoluminescence* measurements (TI-PL), *time-resolved* photoluminescence (TR-PL) and measurements in transmission, and then the setup used for *micro-photoluminescence* measurements (micro-PL), useful for the study of sample homogeneity and the diffusion of the light emitted from the perovskite crystals between the *T-Rex* beads. These techniques differ for the excitable portion of the sample, $50 \div 100$ μm for macro-PL measurements and the

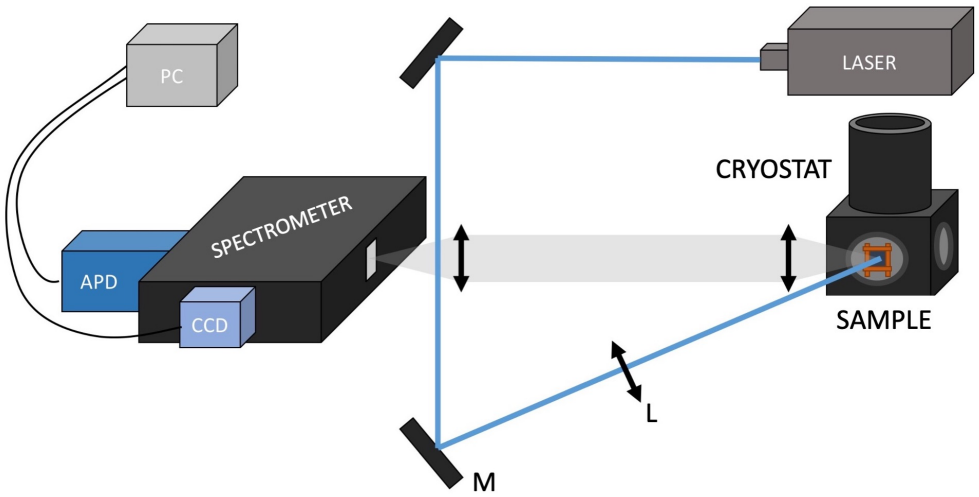

Figure 2.12. Diagram of the experimental setup used for macro-PL measurements.

order of μm for those of micro-PL. In each of these setups the sample is mounted in a vacuum chamber (10^{-7} mbar) inside a helium cryostat with closed cycle or cold finger flow. The minimum achievable temperature is 10 K and is measured with a semiconductor diode near the sample. The temperature in the cryostat can be varied between 10 and 300 K with an appropriate heater.

2.4.1 Macro-PL measurements

TI-PL measurements

In TI-PL measurements, the PL signal is measured by exciting the sample with continuous or pulsed laser sources, but the signal detection is carried out in such a way that the detected photons are measured in fixed time intervals, without any reference to the temporal evolution of the signal in case the excitation laser is impulsive. This allows the spectrum of photoluminescence to be studied by varying parameters such as the location of the excitation laser spot on the sample, the excitation power and the temperature of the sample. Each of these measurements provides different information on the homogeneity on large scale, the presence of intrinsic/extrinsic emission (linked to defects), the processes of *thermal quenching*, that is the decrease in the intensity of PL as the temperature increases. The excitation of the sample occurs by focusing the laser on the sample through the use of a lens system: in particular, in our measurements the *beam waist* of the laser beam on sample was about 100 microns in diameter, typical size that is obtained by using a lens with a focal length between 150 mm and 200 mm and a source with the same spatial characteristics of the one that has available.

In Fig.2.12 we can see the experimental setup used for TI-PL measurements. The excitation sources used are continuous laser (CW) (at 405 nm and 450 nm) or pulsed (at 266 nm and 360 nm) with an energy equal to or greater than the band gap of the sample under analysis. The beam at 360 nm was obtained by the II

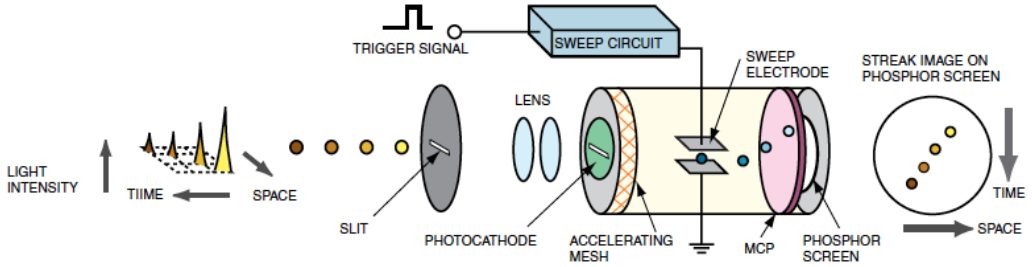

Figure 2.13. Operating diagram of a Streak Camera, instrumentation used in TR-PL measurements.

harmonic generation of the beam from a mode-locked Sapphire:Ti laser ($700 \div 850$ nm, 1.2 ps pulses at a repetion rate of 81.3 MHz). A list of the laser sources used for both TI-PL and TR-PL measurements is shown in table Tab.2.2.

Table 2.2. Laser type used for TI-PL and TR-PL measurements.

LASER	**Mode**	**Wavelength** (nm)
Teem Photonics SNU-20F-100	300 ps pulse; rep. rate 20 kHz	266
Diode laser MLL-III-405	CW	405
Diod laser MLL-III-450	CW	450
Thorlabs CPS520	CW	515
Thorlabs CPS532	CW	532
Spectra Physics Ti:Sapphire[1]	1.2 ps pulse; rep. rate 81.3 MHz	700÷850

The resulting light emitted by the sample (Photoluminescence) is collected through a system of lenses, collimated and focused on the inlet slit of a spectrometer *(Acton Spectra Pro 2500i)*, which is connected, on the flat field output, to a CCD (Charge Coupled Device). The spectrometer used for TI-PL has a focal length of 500 nm and is equipped with three diffraction gratings. For TI-PL and transmission measurements the 1200 lines/mm grating, with 750 nm blaze wavelength, was used. The PL is revealed by the CCD *Andor DU420-BU*, composed of an array of 1024×256 pixels: the size of each pixel is 26 *mu*m. The CCD detector needs to be cooled to a temperature of -70 °C to reduce noise from thermionic emission. The spectral resolution of this setup in my measurements is about 1 meV. Both the CCD and the spectrometer are interfaced to a computer and through a suitable software the spectrum of PL is acquired by controlling the positioning of the spectrometer grating.

TR-PL measurements

TR-PL measurements were made using a *Streak Camera* (*Hamamatsu C5680*) which, coupled to the *ps* pulsed laser, provides a temporal resolution of up to a few *ps*. This detector allows to measure the evolution of the photoluminescence signal in the first *ns* after excitation and to obtain information about the processes of relaxation and

[1]The laser is optically pumped from the second harmonic of a CW Nd:YAG laser.

Table 2.3. Temporal dispersion, temporal resolution and the factors limiting resolution for the 4 time scales of the camera streak used in the TR-PL experiments.

Temporal Scale	Dispersion (ps/px)	Resolution (ps)	Limiting factors
1	0.26	5	Asymchronism between detector and excitation source
2	1.42	15	Spatial dimension of the image
3	2.44	25	Spatial dimension of the image
4	3.7	40	Spatial dimension of the image

recombination. It is also able to simultaneously acquire the spectral and temporal evolution of the photoluminescence signal. The streak camera is positioned at the flat field output of a spectrometer (focal length 300 mm, grating 300 lines/mm grating, blazed at 500 nm). The sample is excited by the II harmonic of a mode-locked Ti:Sapphire *Spectra Physics Tsunami* laser (Tab.2.2), pumped by the II harmonic of a CW Nd-YAG (*Millennia, Spectra Physics*). The Ti:Sapphire laser emits pulses of duration ~ 1.2 ps with a repetition rate of 81.3 MHz. The wavelength of emission can vary in a range between 700 and 850 nm. To obtain photons of energy higher than the band gap of $CsPbBr_3$ (~ 2.3 eV), the Ti:Sapphire beam is duplicated in frequency through a nonlinear crystal of Barium Beta Borate (BBO), obtaining an excitation wavelength of ~ 360 nm.

The principle of operation of the streak camera, which can be defined as an "*optical oscilloscope*", is shown in Fig.2.13. The photons emitted by the sample are dispersed spectrally by the spectrometer and reach the entrance slit of the streak camera in different horizontal positions, depending on their energy. A photocathode converts the photons into photoelectrons which are accelerated towards two vertical electrodes to which an oscillating voltage is applied. This voltage is synchronous, both in phase and in frequency, with the excitation laser: consequently, photoelectrons generated at different times will be deflected in different vertical positions. Then the deflected photoelectrons are multiplied through a micro channel intensifier (MPC), and then reach the phosphor screen, where they are converted into light. This light is finally revealed by a CCD consisting of 768×572 pixels. Then a two-dimensional image is generated with energy/wavelength on the horizontal axis and temporal evolution on the vertical axis. The streak camera I used has four time scales that correspond to different deflection speeds by the deflector electrodes. The streak camera can also be used in *focus* mode, without temporal dispersion of photoelectrons, thus obtaining a spectrally integrated spectrum (TI-PL). The time resolution of this instrument depends on the time scale used during the measurement, as shown in tab.2.3. The time resolution in this kind of experiments is evaluated as the full width at half-height (FWHM) of the laser time profile as detected by the streak camera. In fact, if we consider the laser pulse equal to a delta in time (in our case the pulse lasts 1.2 ps), the temporal broadening, measured when the laser light elastically diffused from the sample surface is detected, depends exclusively on the temporal resolution of the streak camera. This resolution is determined by the temporal jitter between the instrument electronics and the laser oscillator and the finite spatial

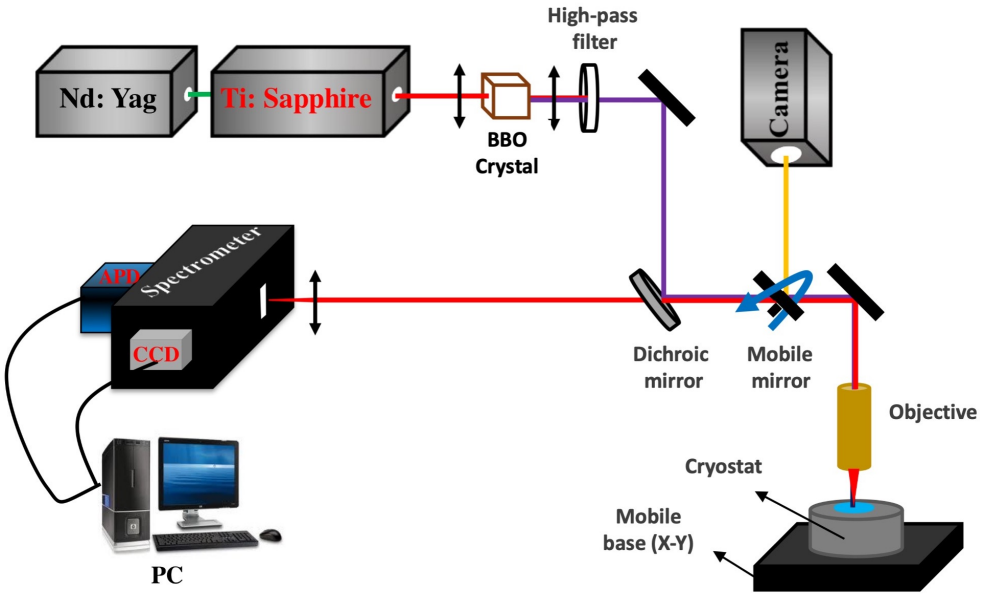

Figure 2.14. Diagram of the experimental setup used for micro-photoluminescence measurements.

dimension of the PL source focused at the input of the instrument.

2.4.2 Micro-PL measurements

In the experimental setup used for macro-PL measurements, the laser beam is focused through a long focal length lens and the sample is excited with a spot of the order of 100 µm in diameter. As a result, the PL signal we measure will be an average emission over a large area of the sample. In contrast, micro-PL measurements allow us to excite the sample with a spot of a few μm, allowing us to investigate the emission properties of the individual microstructures of the sample. In particular, in the setup used for micro-PL measurements (see Fig.2.14) a confocal microscope is used to drastically reduce the illuminated portion of the sample, thus reaching the diffractive limit ($\sim 1\ \mu m$).

The excitation source used are several (see Tab.2.2) including the Ti:Sapphire laser (*Spectra Physics Tsunami*) duplicated in frequency to obtain an excitation wavelength of $\sim$ 365 nm. In addition, the sample can also be illuminated with a white light from a lamp; the reflected light is collected from a camera that captures the image of the sample.

The apparatus has a confocal geometry, in which the excitation light and the produced PL signal follow the same way. To eliminate the laser light in the collection path, a dichroic mirror is placed inside the experimental scheme that reflects the light at the wavelength of the laser and transmits that of the luminescence to be detected. As shown in Fig.2.14, the laser beam, having passed the dichroic, is focused by means of an objective on a cold finger helium flow cryostat in which the sample is placed.

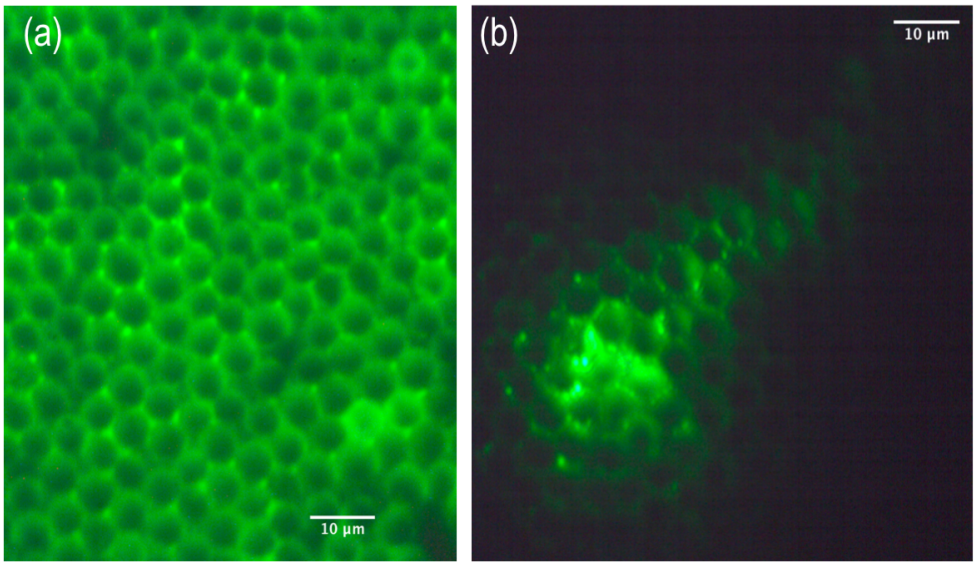

Figure 2.15. (a) Diffusion photoluminescence effect (532 nm) of a 6 µm *T-Rex* sample as detected with the micro-PL setup after excitation of a large portion of the sample with a laser at 405 nm. (b) The PL as detected exciting and collecting the light by the confocal microscope.

The objective *Mitutoyo* 100×, with numerical aperture NA = 0.7, is mounted on a piezoelectric translation stage coupled to a micrometric translation stage that allows a first focus that can be adjusted finely later thanks to the piezoelectric translator.

The cryostat is mounted on two motorized translations controllable from the outside through dedicated software, through which we can move the sample along the X-Y plane with a resolution of 100 nm: this allows to acquire spatially resolved PL maps by moving the laser spot to different points in the sample and capturing the PL spectrum at each of these points.

The luminescence of the sample is collected from the objective and then focused on the input slit of a *Acton Spectra Pro 2300i* spectrometer (focal length 30 cm) via an achromatic doublet with a focal length of 2 cm, leading to a total magnification of 10×. As in the macro-PL apparatus, the spectrometer has two outputs, one of which is flat field on which is placed a CCD *PIXIS 100f, Princeton Instruments* equipped with a matrix of 1340 × 100 pixels. On the second output instead is mounted an avalanche photodiode *ID quantique ID100MMF50-ULN* (APD) for the measurement of decay times (temporal resolution of 60 ps and sensitive area diameter of 50 µm) which is coupled with a fiber to the output slit.

Inserting a kinematic beam splitter before the lens, as shown in Fig.2.14, we can illuminate the sample with the white light lamp and collect the image with the camera.

The spectral resolution of this apparatus is about 1 meV.

Diffusion measurements

The experimental apparatus of micro-PL also allows measurements of the diffusion of photoluminescence on the sample. By exciting the sample laterally, then shining the sample with a beam laser not in a confocal way but at an angle of about 60 degrees, and collecting the PL through the microscope Fig.2.14 and the camera, we get information on the diffusion of the photoluminescence emitted by the sample. In Fig. 2.15 I show an image of this effect obtained for a sample having *T-Rex* beads with a diameter of 6 µm, having a shell of 100 nm of TiO_2, on which a film of $CsPbBr_3$ has been deposited by spinning. The effect will be better explained in Chapter 4 concerning the discussion of the results obtained for this type of samples. It clearly appears that the emitted light spreads between the spheres clearly highlighting the pattern of the substrate and in particular the link that is created between the perovskite crystals and *T-Rex* microspheres.

Chapter 3

HP thin films: the Urbach tail

In this Chapter I will present a detailed analysis of the Urbach tail, which is a characteristic feature that semiconductors with a degree of disorder show in the absorption spectrum. I will show that quantitative information on the Urbach tail in halide perovskites can be extracted by a deep analysis of the photoluminescence in different experimental conditions. Several samples of $CsPbBr_3$ grown with different synthesis techniques, namely bulk crystals, spin-coated thin films, and layers of nanometric thickness grown by RF-MS were investigated. By means of time-integrated (TI) and *ps* time-resolved (TR) PL measurements, as a function of the temperature and the excitation power, we elucidate the role of both dynamic and static disorder in the exciton/carrier recombination dynamics and in the spectral characteristics of $CsPbBr_3$, as well we highlight the role of strain in determining the band-gap energy. The results here presented have been published in ref.[35].

Structural and dynamical disorder in semiconductors is a topic of fundamental relevance. In fact it contributes to the spectral line shape of the photoluminescence and it has a significant role in determining the carrier transport properties at the band edge. Halide perovskites show a peculiar degree of disorder and disorder affects the optical/electrical properties that make HPs of interest for numerous innovative optolectronic applications. In a semiconductor, it is important to distinguish between structural disorder and dynamical disorder. Structural disorder is related to defects. Inorganic halide perovskites are commonly considered "defect tolerant" [59, 17, 18, 98] being the cross section of defects small. Their defects originate from the presence of elements different from the constituent ones and from structural disorders like vacancies, deviation from stoichiometry, domains formation, and lattice distortion, possibly combined with local strain. The dynamical disorder comes from the structural instability of these perovskites around room temperature [122, 57, 65, 143] and it has been experimentally investigated [94, 75, 100] and theoretically modeled [41, 109]. However many aspects are still controversial as the presence of a dynamical Rashba effect [93, 55]). Both kind of disorder affects the carrier dynamics and the overall properties, as recently reported in two-dimensional lead halide perovskites

[127]. In fact, independently from its nature, it can give rise to a reduction of the carrier lifetime and mobility, with the consequent quenching of the PL intensity, and a spectral broadening of the PL spectrum. The shallow states in the gap related to the static and/or dynamic disorder affect both the carrier dynamics and the spectral shape; on the contrary the states deriving from the static disorder, such as recombination centers and deep traps, affect only the recombination lifetime. Excluding a few single nanocrystals of outstanding quality that exhibit very long carrier lifetimes and mobility [50] and/ or very narrow PL linewidths [37, 106], at low temperatures, for most of the samples lifetimes of the order of a few hundreds of *ps* and PL linewidths of few meV [104] are reported. If we analyze the PL lineshape we can evidence a main excitonic peak and two tails, at higher and lower energy. The low energy contribution represent the Urbach tail (UT): its slope as well as the width of the main PL peak depends on the degree and nature of the disorder. Many studies have found a direct relationship between UT and performance in photovoltaic applications [28, 73].

3.1 Sample preparation

Different $CsPbBr_3$ samples were prepared and investigated: a macro-crystal sample (*bulk*), with a *mm* size along each axis, was grown by the antisolvent vapor-assisted crystallization (AVC) [154], and methanol was used as antisolvent. The bulk shows the presence of a few differently oriented crystalline domains detected in the XRD pattern [40]. Using a laser excitation spot ($\sim 10^{-2}\ mm^2$), much smaller than the domain size, the sample response to the optical excitation can be considered as that of a single crystal. Microcrystals were realized by spin-coating, on a soda lime glass (SLG) or silicon (Si) substrate, starting from a $CsPbBr_3$ solution prepared by dissolving equal molar quantity of the precursors (CsBr and $PbBr_2$) in dimethyl sulfoxide [54]. The solution was stirred overnight to obtain a clear liquid. After the spinning, the samples were dried and annealed at 120 °C for 10 min. Thin films of $CsPbBr_3$ were also realized by RF-MS following the procedure describes in Chap.2 [13]; several samples were investigated with thickness in the range 50÷500 nm deposited on different substrates: the main focus will be on samples deposited on SLG and Si. The typical size of crystals in spin-coated and magneto-sputtered samples ranges between few tens of *nm* to 1 µm and the main differences between the two kinds of samples are the homogeneity and compactness of the film. It is worth mentioning that all the samples investigated did not present evident material decomposition/aging over months, having kept them in controlled dry ambient for the time duration of the whole set of experiments.

The analysis of the samples, then of the characteristics of the Urbach tail, have been realized by means of the set-up of micro-PL (µPL) and macro-PL (MPL) introduced in the Chap.2 (Fig.2.14 and Fig.2.12, respectively). As mentioned above, the distinction between these two setups lies in the spot excitation laser used, 10^{-4} cm^2 for MPL and 1÷2 μm^2 for µPL. All MPL experiments were performed in a quasi-back scattering geometry, placing the samples in a closed-cycle cryostat and changing the temperature in the range of 10÷300 K. The experiments of µPL were realized using the home-made confocal microscopy setup of Fig.2.14 equipped with

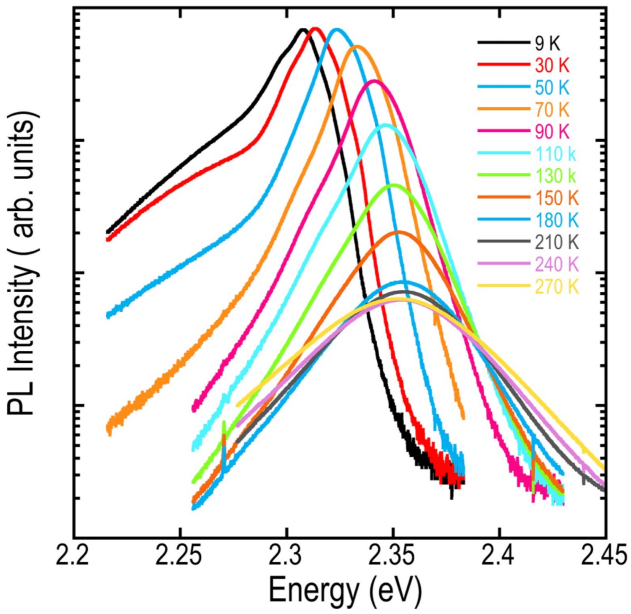

Figure 3.1. PL spectra as a function of T for a $CsPbBr_3$ spin-coated film on a soda-lime glass substrate[35].

a Mitutoyo 100× objective (378-806-3, NA = 0.7) or a Mitutoyo 50× objective (378-818-4, NA = 0.42), providing a spatial resolution of about 500 nm or 1 µm depending on the objective. Samples were kept in a low-vibration Janis ST-500 cryostat, which was mounted on a Physik Instrumente x–y translation stage for scanning the sample surface. The spectral resolution was ≤ 1 meV in both MPL and µPL experiments. A frequency-doubled mode-locked *ps* Ti-Sapphire laser, operating at 81.3 MHz repetition rate with 1.2 ps long pulses, was used for TR-PL experiments; in this case, the maximum excitation intensity was about 10 W/cm^2, corresponding to an estimated excitation density of about 2×10^{16} cm^{-3} carriers per pulse. TR-PL measurements were carried out only in the macro-scale configuration using a synchro-scan streak camera (time resolution 5 ps) after spectral dispersion of the detected signal through a 25 cm monochromator, equipped with a 300 gr/mm (blaze 500 nm, spectral resolution 2 meV). It is relevant to point out that we did not find changes in the PL spectral characteristics, particularly in the Urbach tail after several temperature cycles in the range 10÷300 K.

3.2 PL analysis

3.2.1 CW PL

We performed MPL measurements, exciting the PL with a 405 nm (3.062 eV) CW diode-laser; the photon energy is well above the band-gap energy of $CsPb_3$; the excitation density was ≤ 10 W/cm^2. In this experimental conditions the PL spectrum is dominated by the exciton emission (central peak) and two exponential tails are

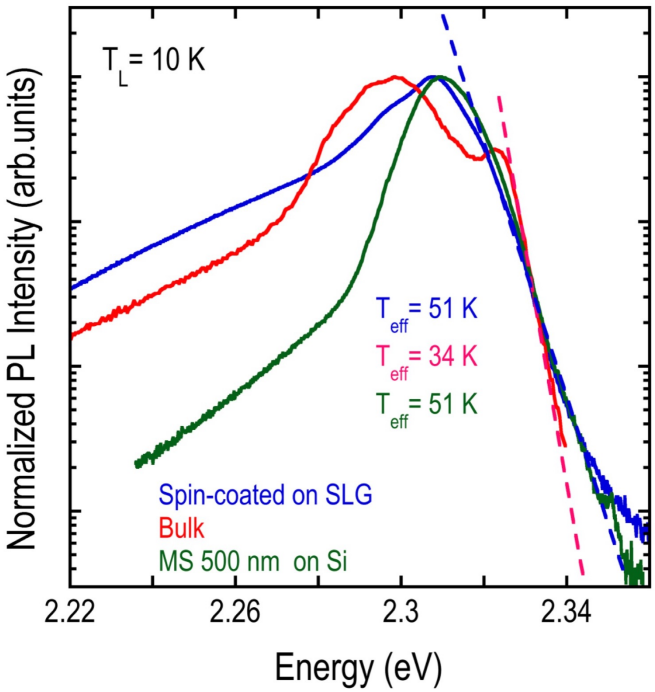

Figure 3.2. Low temperature PL spectrum of different $CsPbBr_3$ samples: bulk sample (red curve), spin-coated thin film (blue curve), and 500 nm thick film obtained by RF-MS on silicon (green curve). The dashed lines are fits of the high energy tail and the effective temperatures are reported [35]

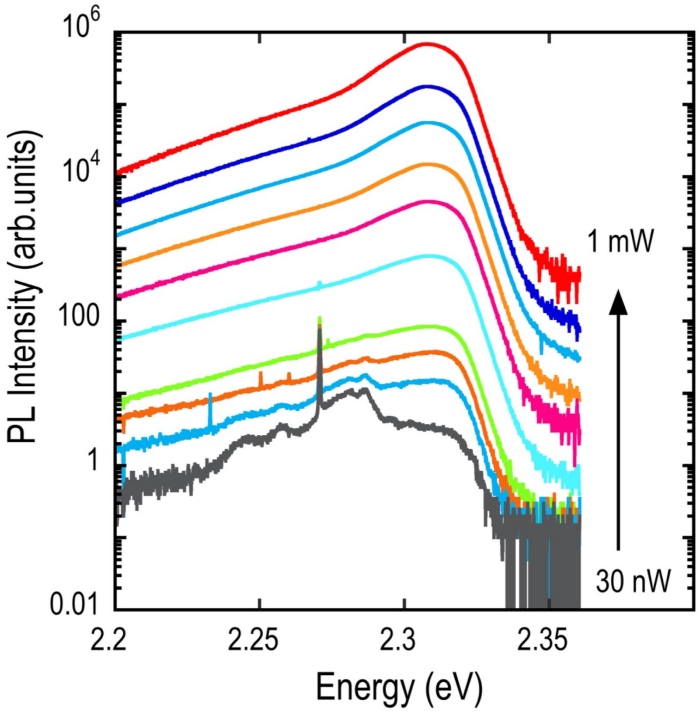

Figure 3.3. Low temperature PL spectra of a spin-coated $CsPbBr_3$ sample on a Si substrate as a function of the excitation power. The step in the power follows the sequence 1-3-10[35]

present that change with the temperature (Fig.3.1). At low temperature the PL peak has a central Gaussian shape with a shoulder on the low energy side, more or less pronounced depending on the sample, due to localized or bound exciton emission. The Gaussian shape indicates the presence of disorder and the PL broadens when the sample temperature increases. The tail on the high energy side, whose slope changes with T, is often observed in the PL: it comes from the thermal distribution of the excitons and, when the thermal energy promotes the exciton dissociation, from recombination of the free carriers population. The broadening of the exciton emission on the high energy side should be absent in a perfect semiconductor; it takes origin from processes (i.e. disorder, impurity scattering, localization) that, breaking the wavevector K selection rule, allows radiative recombination of excitons with $K \neq 0$. The spectral profile of the excitonic tail depends on the exciton density of states (DOS), the K-vector indeterminacy, due to disorder, and the temperature that determines the population of the high energy states [110]. In a non-degenerate case (this is our experimental condition with a low excitation density), the exciton population can be described by a Boltzmann distribution. Therefore the slope of the high energy exponential tail can be used to evaluate the temperature of the excitons. If we assume a complete relaxation of the K selection rule, with a step-like density of states (2D-system), the high energy tail slope directly provides the temperature of the exciton gas. In 3D systems, with a DOS having a square root dependence on the energy, the slope gives an effective temperature T_{eff} no more than 10% higher than the real excitonic temperature. In Fig.3.2 we compare, at low temperature for the different samples prepared, the PL spectra normalized at the peak intensity. The PL of the bulk sample is dominated by the bound exciton emission at around 2.298 eV, while the free exciton emission is at 2.323 eV [111]. Increasing the temperature the bound exciton emission is suppressed. The sputtered and the spin coated films have a similar PL peak at 2.309 eV. All of them exhibit similar spectra with a high energy exponential tail, which corresponds to an exciton temperature T_{eff} higher than the lattice temperature T_L.

At low lattice temperature T_L, it is not surprising to find an exciton temperature T_{eff} higher with respect to the lattice [40, 48, 145]; gradually T_{eff} and T_L get equal at higher T_L. The difference between the two temperature values indicates that the exciton gas does not thermalize with the phonon reservoir in the time scale of the exciton lifetime [112].
The low energy tail of PL in Fig.3.2 is nearly bi-exponential at low T and rising T gradually becomes mono-exponential; this relevant tail in PL is related to the Urbach Tail (UT), so it is correlated to disorder.

We performed experiments varying the excitation density to obtain information on the nature of disorder.

The results obtained for the spin-coated sample at T_L= 10 K changing the incident power over four order of magnitude (30 nW ÷ 1 mW) are shown in Fig.3.3. At the lowest power, the PL is dominated by defects and the excitonic contribution is negligible. Increasing the excitation density, we observe a saturation of the emission arising from defects and the excitonic contribution to PL becomes dominant; at the same time, the low energy tail increases and acquires an exponential constant slope: this is a clear evidence of its close correlation with the exciton emission. As discussed in previous chapters, samples present a certain degree of spatial inhomogeneity which

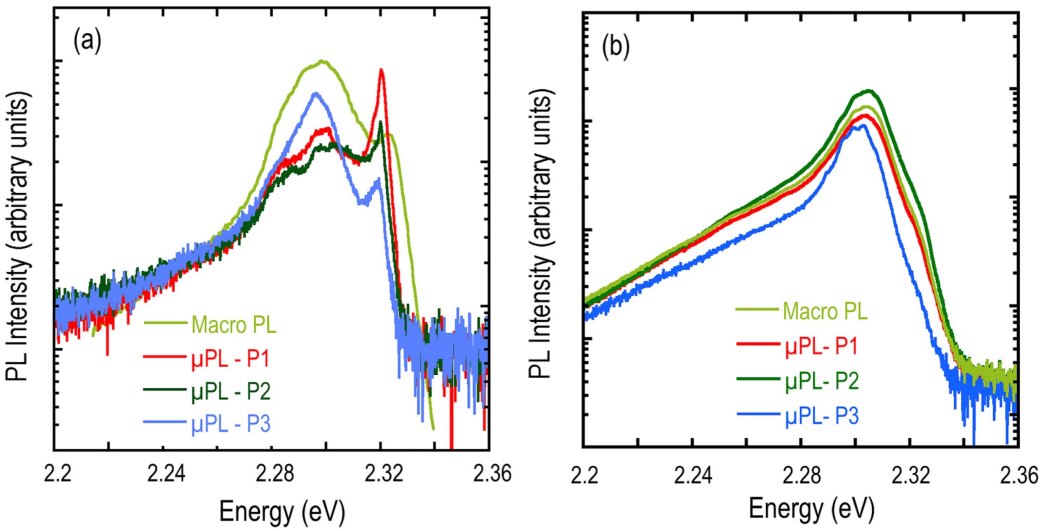

Figure 3.4. Comparison between µPL (1 µm spot) and MPL spectra (100 µm spot) at a lattice temperature of 10 K for the bulk sample (a) and for a spin-coated sample on SLG (b). P1, P2, and P3 are different points of the samples.[35]

is correlated to the static component of the disorder. To investigate this aspect, we performed µPL at low T so to provide a distinction between disorder acting on a macroscale, i.e., over lengths exceeding a micrometer, or on a submicrometer scale.

In Fig.3.4 we report a comparison at T_L=10 K between the PL of the bulk sample (a) and a spin-coated film on SLG (b) detected with the macro-PL setup and a set of measurements in different points of the samples detected by the confocal µPL setup. For the bulk sample, it is quite remarkable that the bound exciton emission at around 2.3 eV and the free exciton emission at 2.32 eV have a very similar broadening irrespective of the spatial scale of the detection setup. This result is a strong indication that the broadening originates from a disorder on a submicrometer length scale below the resolution of the µPL setup. Moreover, the free exciton line PL has different weight respect to the bound exciton region (Fig.3.4 (a)): this aspect arises from the static disorder. Most likely, the emission results from excitons bound to vacancies [111, 59] and, as expected, it disappears increasing the lattice temperature. Therefore, it is not unexpected that the observed changes depend on the detection spot. In the case of the spin-coated sample [Fig.3.4(b)], we found slight differences in the exciton energy with no major change in the PL line shape; this is again evidence of a disorder acting on a submicrometer scale. The graph in log scale [Fig.3.4] helps in showing the very same characteristics of the low energy tail, irrespective of the detection (MPL/µPL).

This last result helps us in understanding the contribution of the static disorder. In fact if static disorder dominates the Urbach tail, we would expect to detect changes in the low energy tail, depending on the excited spot in the sample. On the contrary, as shown in Fig. 3.4, the lack of significant changes in the low energy exponential tail of the PL is a result that supports the negligible contribution of the static disorder in the Urbach tail.

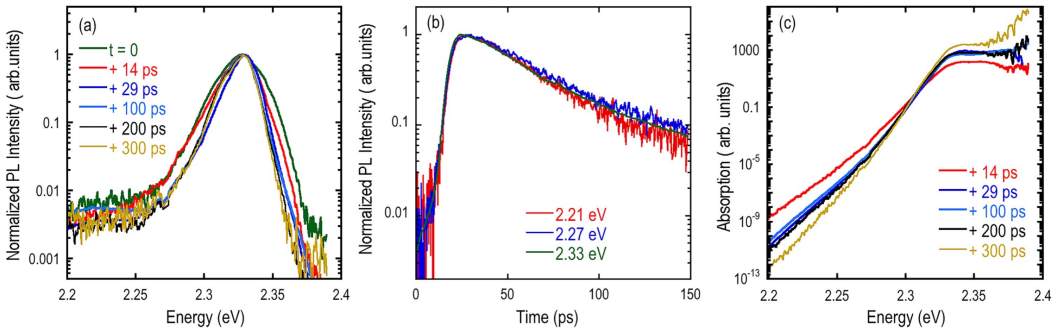

Figure 3.5. (a) Time resolved PL spectra at $T_L = 10$ K of a 70 nm thick film deposited on SLG by means of RF-MS. (b) PL decays at two energies in the Urbach tail and at the exciton energy. (c) Absorption extracted from (a) as discussed in the text [35]

.

3.2.2 Time-resolved PL analysis

TR PL measurements allow to extract more information about the kind of disorder (static/dynamic) at the origin of Urbach tail. In fact, while CW PL measurements return similar effects regarding static or dynamic disorder, TR PL spectra, giving direct access to the population dynamics of the states contributing to the radiative emission, can bring evidence of the different nature of disorder. In particular, on a picosecond time scale, we expect that an exponential tail due to dynamic disorder, being closely related to the exciton-phonon interaction, will follow the exciton dynamics without major changes in the spectral shape. On the contrary, if a carrier thermalization occurs within an exponential tail of real states, which originate from static disorder, the time scale of the process is of several tens of *ps* and different time evolutions inside the PL band are found. In fact, the exciton and carrier localization typically produces a characteristic spectral diffusion [114, 49] and a marked variation of the dynamics inside the PL band; this different dynamics is also observed in the PL rise time/decay time at different energies inside the PL spectrum [40]. In Fig.3.5 we compare normalized TR PL spectra of a 70 nm thick sample prepared by RF-MS on SLG. The high energy exponential tail has a slope which decreases with time delay as a consequence of the exciton gas cooling whose temperature gradually approaches that of the lattice [40]. The signature of the complete thermalization of the excitons is the constant slope of the high energy PL exponential tail. If we consider the time evolution of the low energy side of the PL, we detect the absence of an internal dynamics and a decrease of the exponential slope during the excitons cooling until their temperature gets stabilized. Therefore, the same dynamics, as shown in Fig.3.5(b) for different energies, i.e. the exciton and two energies in the low energy side, characterizes the Urbach tail and the exciton emission, and this is the signature of the intrinsic nature of the Urbach tail, arising from a dynamic disorder.

3.3 Results discussion

From the results obtained through the measurements previously presented, all the samples we analyzed show a spatial inhomogeneity that, in the case of the bulk

sample (Fig.3.4) mainly affects the contribution of the free and bound exciton emission and does not produce any relevant change in the free exciton linewidth and in the low energy tail. Referring to spin-coated and magnetron sputtered samples, we find that the PL obtained from MPL measurements shows only a few meV (nearly 2 meV) increase in the line broadening with no change in the shape when compared to µPL spectra. Therefore, at low temperature, in all the investigated samples, we conclude that the main PL broadening is a consequence of a static disorder in a sub-micrometer scale while on the macro-scale we observe a limited randomness of the free exciton energy.

Moreover, we have shown that in both CW and TR experiments the excitons and carriers population is thermalized in a few *ps*. The presence of a thermalized distribution at a temperature T_{eff} , higher than T_L at low T and gradually approaching this latter rising T, allows to extract the absorption $\alpha(E)$ from PL spectra given the relation [9, 141]:

$$I_{PL}(E) = E^2\alpha(E)e^{\frac{-E}{KT_{eff}}} \tag{3.1}$$

$\alpha(E)$ is the absorption coefficient and T_{eff} is the effective temperature of the excitons/carriers population we extract from the high energy tail of the PL spectrum. As previously noted, using in our experiment a low excitation density ($\leq 10^{16}\ cm^{-3}$) we can assume a Boltzmann distribution for the population (non-degenerate case). It is worth mentioning that in several cases the direct measurement of the absorption coefficient and in particular its spectral dispersion is a difficult task, for instance when nanometric thin films or thick samples are studied, and when the substrate is an absorbing material unless to resort to techniques as etching. Therefore the use of the PL spectrum is a very efficient way to retrieve $\alpha(E)$; moreover we can have an high sensitivity and cover an extended dynamic range as it will be shown in the following figures.

By means of equation (3.1) $\alpha(E)$ is extracted from the spectra of fig.3.2 and it is shown in fig.3.6. Using a log scale representation (fig.3.6(a)) we can appreciate the extended UT over ten orders of magnitude, while in linear scale (figure 3.6(b)) the free exciton resonance is visible and we also observe the Stokes Shift (SS) of the PL (dashed lines) respect to the absorption.

However, in TR experiments, the hypothesis of thermal equilibrium has to be verified so to extract $\alpha(E)$. Therefore we have to exclude the first few picoseconds needed to the exciton gas to reach a quasi-equilibrium thermal distribution. Then we can extract $\alpha(E)$, having evaluated T_{eff}, from the high energy tail of the PL spectrum. In fig.3.5(c) we show the absorption as extracted from the spectra of fig.3.5(a) at different time delays, correspondingly the effective excitonic temperature changes from 81 K (delay +14 ps) to 51 K (delay $\geq$ 300 ps). It is worth noting the presence of the exponential tail covering more than ten orders of magnitude and how this slope follows the decrease of T_{eff}; this is a marked evidence of the strong correlation between such slope and the exciton dynamics. The main consequence of this result is the proof of the intrinsic nature of the Urbach tail, which comes from the dynamic disorder due to the exciton-phonon interaction; instead the contribution of the static disorder is negligible.

In fig.3.7 the absorption of the spin coated sample on soda lime glass is shown

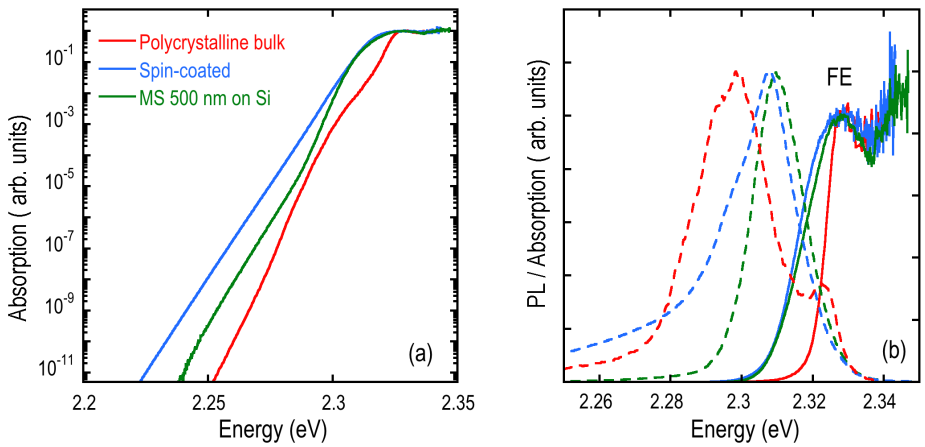

Figure 3.6. (a) Absorption in log scale as extracted from PL spectra of fig.3.2 (b) PL spectra of fig.3.2 in linear scale (dashed lines) and absorption (continuous lines) in linear scale[35].

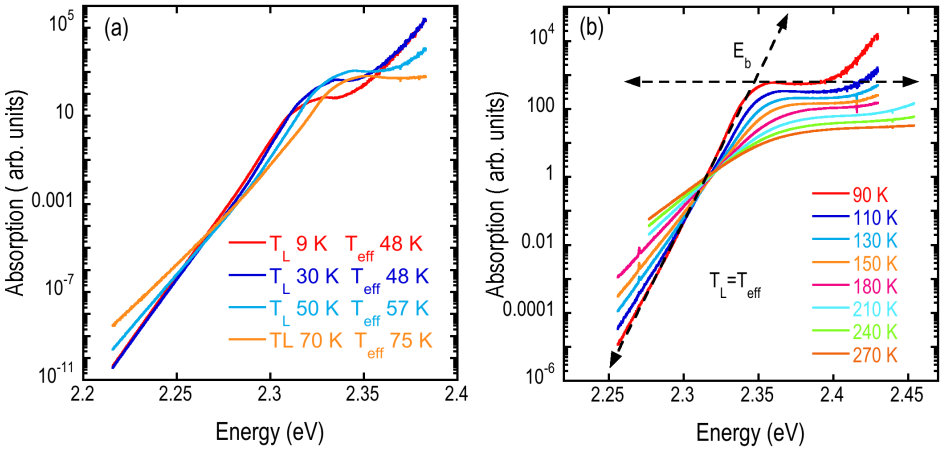

Figure 3.7. Absorption as a function of T: a) low T range. b) high T range[35].

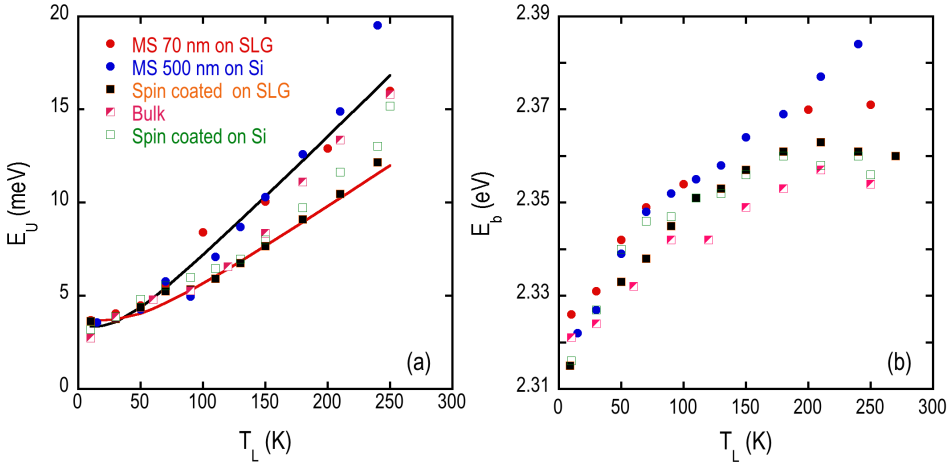

Figure 3.8. (a)E_U vs T_L for the whole set of investigated samples. The solid lines are fits as discussed in the text. (b)E_b vs T_L for the whole set of investigated samples [35].

at different temperatures as extracted from PL spectra of fig.3.1.

A fit of the low exponential tail provides the value of the Urbach energy E_U and we want to enlighten a correlation, if present, with the exciton energy E_b . We note that in disordered systems the PL peak energy, due to the Stokes shift, does not give directly the value of E_b; therefore we have estimated E_b in an approximated way. In fact, we have evaluated, for each temperature, the quantity $E_b{}^*$ as the energy of the intercept, on a log scale, of the line determined by the almost horizontal DOS and the line determined by the exponential tail, as shown in fig.3.7(b). Being the shift of $E_b{}^*$ with respect to the exciton energy E_b independent of the temperature, i.e. from E_U, we can assume E_b=$E_b{}^*$ as long as we are interested to its variation with the temperature with no loss in generality. In fig.3.8 the Urbach energy E_U and E_b are reported as a function of the lattice temperature for the whole set of investigated samples.

It turns out that the Urbach energy E_U increases monotonously with T_L, and almost linearly at high temperature; instead the dependence of E_b on T_L changes around 100-150 K, showing a marked flattening as commonly reported in literature. This latter behavior, which comes out to be sample dependent, indicates that other processes, in addition to the intrinsic ones due to the exciton-phonon interaction, contribute to determine the temperature dependence of the band gap energy.

Similar results are found for all the investigated samples and in fig.3.9 the relationship between the value of the energy E_b and the Urbach energy E_U is reported for each temperature.

All samples show a similar behavior in the temperature range 10-270 K; in particular, apart from the *bulk*, the same dependence of E_b on E_U is almost linear at low T, below $T_M \approx 110$ K. Instead, above T_M, the relation between E_b and E_U deviates from linearity and it depends on the sample under study. It is also worth noting that similar values of the Urbach energy, as the ones here found, are reported

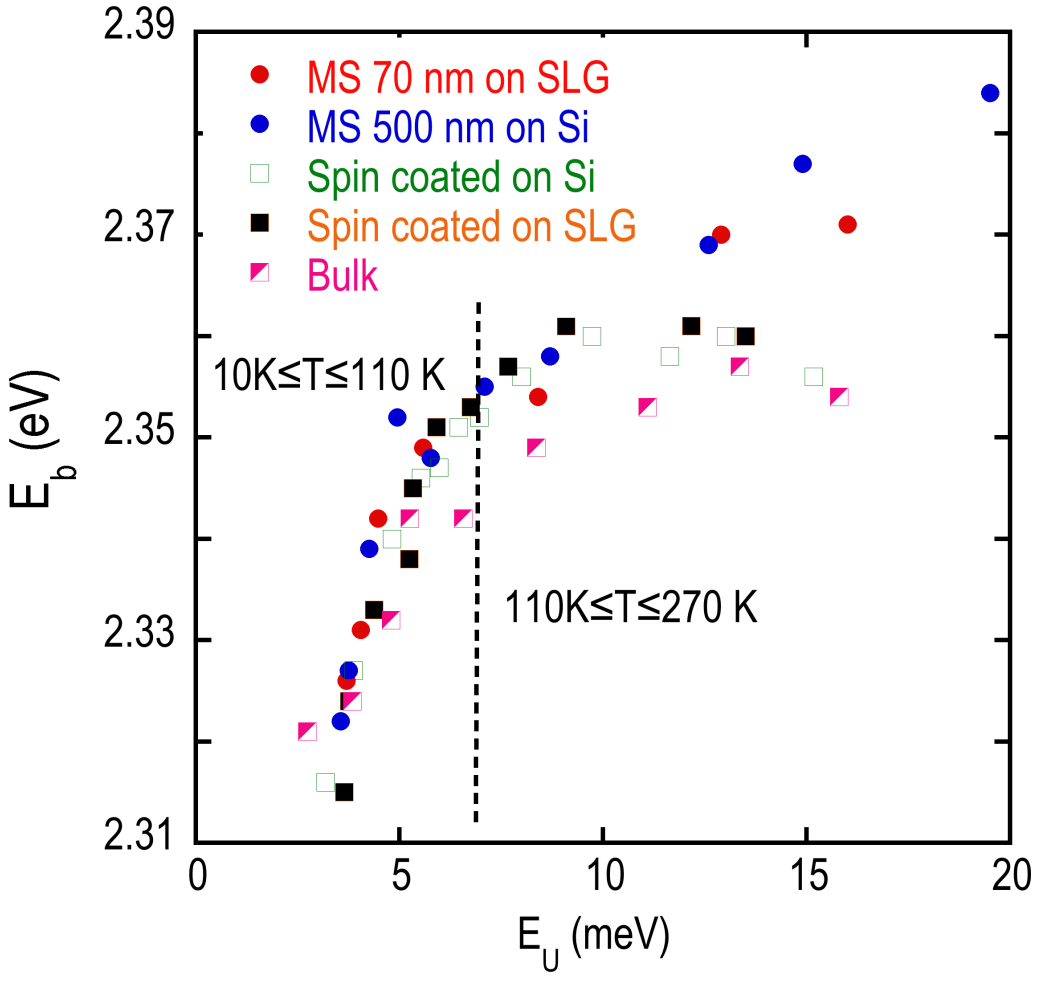

Figure 3.9. Dependence of E_b on E_U for samples differing for substrate, thickness, synthesis/deposition method. The dashed line separates the temperature range below/above 110 K [35].

in literature for halide perovskites nanocrystals and quantum dots [74, 85, 52]: this finding suggests that the origin of the tail in this class of materials does not involve relevant contribution from the crystal surfaces.

To understand the experimental results, we have to consider that the exciton/carrier-phonon interaction is responsible for the band gap shift with the temperature, as a consequence of the T-dependent phonon occupation number n, and it also accounts for the increase of the Urbach tail slope due to its growing fluctuation with T. Both processes have the same dependence on n. Cody and others [23, 116] stated an almost linear dependence of E_b on E_U if the same phonons are involved, which in our case explains the results of fig.3.9 below T_M. For temperature $T \geq T_M$, we find a behavior which cannot be reproduced by a competition between phonon modes as already invoked by ref.[19], and it is rather sample dependent. It has to be noted that the lattice thermal expansion accounts only in part to the band-gap energy shift. In fact, on the basis of the few experimental data at room temperature concerning the volumetric expansion coefficient α , the bulk modulus B[105] and the pressure coefficient of the band-gap[137], we can estimate a value of $\frac{dE_g}{dT} = 5.84 \times 10^{-2}$ meV/K at room T. Even considering the variation of α with T, in the framework of the Einstein-Debye model with a phonon energy of 12 meV, the estimated change in the band-gap energy is around 14 meV in the range 10-300 K (with a negligible dependence on the phonon energy): this value does not account for the results of fig.3.8(b). Moreover, above 50 K the energy shift of the band-gap due to the lattice expansion results linear, which is very different from the data of fig.3.8(b). Therefore the experimental findings of figs 3.8(b) and 3.9 require an extrinsic mechanism, sample dependent, which could be a release of the strain in the bulk of the crystal or at the interface between the film and the substrate.
The experimental data of fig.3.8(a) can be reproduced according to the expression reported by Cody and coworkers [23]

$$E_U = \frac{\hbar\omega_{ph}}{\sigma_0}\left[\frac{(1+X)}{2} + \frac{1}{exp(\hbar\omega_{ph}/k_BT) - 1}\right] \tag{3.2}$$

where $\hbar\omega_{ph}$ is the average phonon energy, σ_0 is the steepness parameter and X is the static disorder contribution normalized to the zero-point fluctuations. The solid lines in fig.3.9(a) are two different fits with the same X value of 0.01, and two different values of the average phonon energy, and steepness parameter; the black (red) line corresponds to $\hbar\omega_{ph} = 9$ (13) meV, in agreement with the phonon energies in $CsPbBr_3$ [83, 42] and σ_0=1.3 (1.8) 10^{-3}, respectively. The other experimental data can be fitted with values of $\hbar\omega_{ph}$ and σ_0 intermediates between them and the same value for X.

So, our experimental results bring clear evidence that in $CsPbBr_3$ the Urbach tail has an intrinsic origin, related to the exciton-phonon interaction, and that the contribution of the static disorder is quite small. Noting that the values of the Urbach energy reported in literature [27, 74] for other types of halide perovskites are comparable to the ones here discussed, our conclusion is that the intrinsic nature of the Urbach tail is a common characteristics of this class of materials.

However it is difficult to identify the intrinsic mechanism which rules the de-

pendence of E_U on temperature in semiconductors. In fact, different models have been proposed. In presence of a strong exciton-phonon interaction as in ref.[124] we can have exciton self-trapping. The fluctuations of the band-edge due to thermal phonons can possibly originate the Urbach tail as in ref.[116]. Finally electric field at the micro-scale due to phonon thermal excitation has been proposed in ref.[31]. However, in all these different theoretical frameworks, the dependence of E_U on T is the same as in ref.[23] and equation (3.2): this makes hard the identification of a specific mechanism between the different proposed.

Now we can try to answer a question: given the impressive advances in opto-electronics based on halide perovskites in the last decade can the UT represent a limitation to the performance of a device? If the UT comes from intragap states that eventually affect the transport mechanism and the carrier recombination, we expect consequences on a device efficiency. Instead, on the basis of the results here discussed and literature data, we can conclude that in halide perovskites the presence of the Urbach tail will not represent a limit to the performance of a solar cell or a light emitting device, which are presently the most interesting devices under study. In fact, investigations on the correlation between the UT and the photovoltaic conversion efficiency [27, 136] and recent results [128, 91] bring to the conclusion that the intrinsic origin of UT can account for the large values of the open circuit voltage in solar cells. Instead, the limitation in the power conversion efficiency mostly originates from the high content of defects at the interfaces between the active layer and the charge transport layer, so requiring a proper engineering of such interfaces [128, 91]. In halide-perovskites LEDs the overall performance has been improved by material engineering [64] (controlling the grain size, optimizing the injection of carriers, etc.); presently the major problem seems to rely on the light extraction efficiency due to the large refractive index mismatch, so that photonic structures have been recently used to improve the external efficiency [157]. This specific topic will be addressed in chap.4. In fact, the experimental results that I present in the following chapter, concerning the light diffusion and ASE in samples where $CsPb_3$ microcrystals are integrated with *T-Rex* beads (Chapter 4), suggest a way to improve the light extraction.

Chapter 4

Coupling HP to *T-Rex*

In this chapter I will show the experimental data obtained for the samples under analysis, going into detail regarding the synthesis of $CsPbBr_3$ and its integration with *T-Rex* spheres. Our results show how this integration leads to *Light Diffusion*, *Random Lasing* and *Amplified Spontaneous Emission* (ASE) phenomena. First of all, to proceed to the integration of $CsPbBr_3$ with the beads, it was necessary to identify the most suitable deposition technique, between the two we used (spin-coating and magnetron sputtering) enlighting advantages and disadvantages. This preliminary activity led to the refinement of the synthesis of *T-Rex* and perovskite. Then, based on the photoluminescence analysis, we tried to understand how the diameter and thickness of the shell of the *T-Rex* affected the interaction between spheres and perovskite. To this aim we investigated a large set of samples listed in tab.2.1, comparing the results obtained by PL spectroscopy. This allowed to define a protocol for the $CsPbBr_3$ deposition, thereby fixing the dilution of the *T-Rex* and the thickness of the shell. Samples prepared with the refined protocol showed random lasing and ASE effects.

4.1 Sample preparation: morphology and homogeneity

Samples were prepared depositing on a Si substrate SiO_2 spheres of different diameters covered by a 100 nm TiO_2 layer by ALD. A TiO_2 layer surrounds the spheres and this leads to spheres with a SiO_2 core and a TiO_2 shell (*T-Rex*) [131].The TiO_2 layer is applied to exploit its photocatalytic properties of interest for different applications [3]. An exagonal 2D lattice of spheres is formed on the substrate, constituting the metasurface which is then decorated by spinning the $CsPbBr_3$ solution o depositing it by RF-MS. Samples with different *T-Rex* microsphere diameter were realized as reported in tab.2.1.

The preliminary work consisted in the deposition, by means of Radio Frequency-Magnetron Sputtering (RF-MS), of thin films of $CsPbBr_3$ (200 nm thickness) on different substrates (fig. 4.1), with and without *T-Rex*, in order to understand how

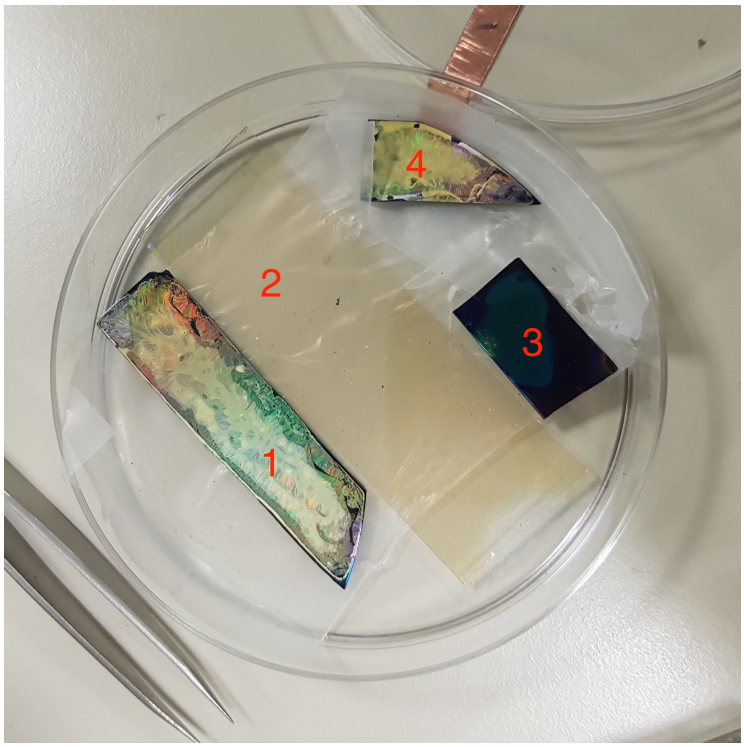

Figure 4.1. First *T-Rex*/PVK samples made using RF-MS. The samples shown differ in the type of material used as substrate and the layers of which they are composed. (see tab.4.1)

Table 4.1. *T-Rex*/$CsPbBr_3$ samples made using RF-MS. Sample 1 is the sample with all layers as discussed in the text. Sample 2 has only $CsPbBr_3$ deposited on a soda lime glass substrate. Sample 3 does not have the SiO_2 spheres that form the core of *T-Rex* but $CsPbBr_3$ is deposited on a TiO_2 over a Si substrate. In Sample 4 the beads are not covered by the TiO_2 shell . The bead diameter is 2 µm.

Sample 1	Si + *T-Rex* (SiO_2 + TiO_2) + PVK
Sample 2	Soda Lime Glass + $CsPbBr_3$
Sample 3	Si + TiO_2 + $CsPbBr_3$
Sample 4	Si + SiO_2 + $CsPbBr_3$

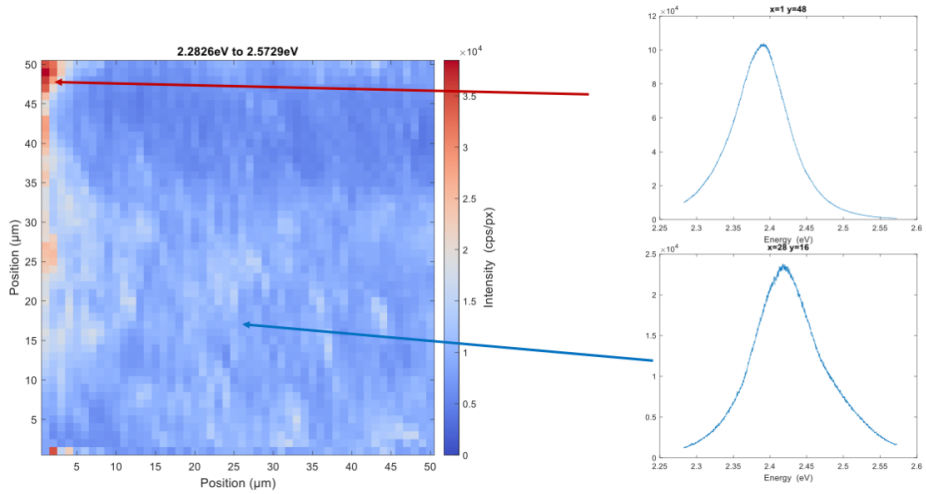

Figure 4.2. Micro-PL map of sample 1 (50 µm×50 µm; step 1 µm; P=500 µW; laser=366.9 nm). On the right the PL spectra acquired in two different points are shown.

perovskite and *T-Rex* interfaced. In tab.4.1 a summary table of the substrates used for the perovskite deposition is reported: the different samples were deposited at the same time in order to highlight the differences between them. Sample 1 is the complete sample, i.e. formed by the silicon substrate on which TiO_2 and the *T-Rex* and finally $CsPbBr_3$ are deposited; sample 2 is composed of a thin film of $CsPbBr_3$ deposited on a soda-lime glass: this sample is used as reference regarding the optical properties of $CsPbBr_3$; sample 3 is the sample without SiO_2 spheres that form the core of *T-Rex* while sample 4 is the one without the TiO_2 layer. The differences in the substrates allowed me to evaluate the role of each layer in determining the optical properties of the sample.

By means of a setup of micro-PL and macro-PL spectroscopy (fig. 2.14 and 2.12, respectively) I studied the sample homogeneity concerning the main PL characteristics. The micro-PL setup allowed me to appreciate the quality and homogeneity of the samples with a spatial resolution of the order of 1 µm: the samples showed a good degree of homogeneity, indicating that the RF-MS technique is ideally suited for homogenous deposition of perovskites especially for large area samples.

In Fig.4.2 I report a micro-PL map of sample 1 at room temperature: the color scale refers to the PL intensity integrated in the spectral range 2.2826-2.5729 as it can be seen, there are no strong differences regarding the intensity of photoluminescence, index of a good degree of homogeneity. More information concerning the spectral variations in the sampled area are shown in Fig.4.3 where for each point of the map the PL peak energy is reported.

Previous results prove that this technique allows to obtain samples with a good degree of homogeneity and that anyway there is affinity between spheres *T-Rex* and perovskite crystals. A further step was necessary to understand: a) the optimal sphere diameter to couple to $CsPbBr_3$, b) which dilution has to be used to deposit

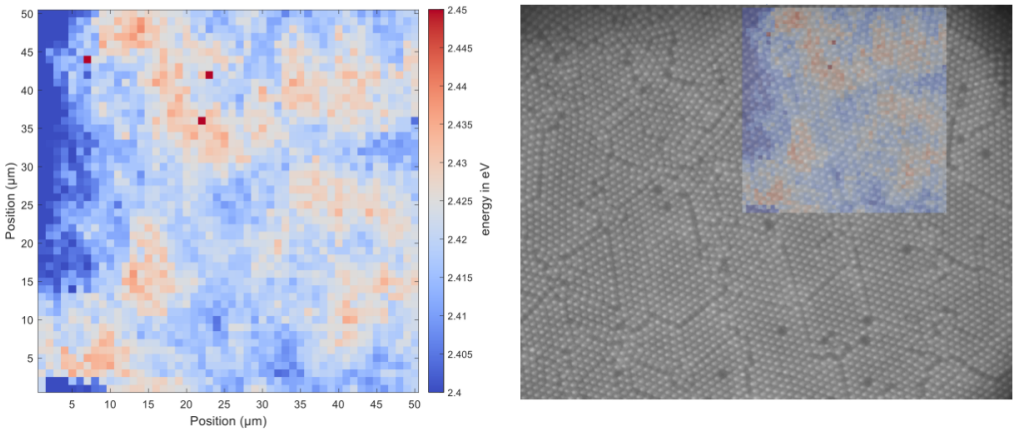

Figure 4.3. Micro-PL map of sample 1 (50 µm×50 µm; step 1 µm; P=500 µW; laser = 366.9 nm). The PL peak energy is reported in the map. On the right the image of the sampled region is shown.

the spheres on the substrate of Si, c)the thickness of TiO_2 most suitable for the sphere *T-Rex* d) the deposition technique that best suits our applications between RF-MS and Spin-coating. For this reason it was necessary to prepare the samples of tab.2.1 with the different dilutions D1, D2 and D3 introduced in the Chap.2. Depending on the dilution of SiO_2 spheres, we end up with a multi-layer or mono-layer substrate and this can affect the coupling with perovskite microcrystals. Our result indicates that the dilution D3 (1:100 in water) leads to a mono-layer of beads, with regions without spheres. The dilution D2 (1:10 in water) instead guarantees a substrate totally covered by SiO_2 spheres, which we remember will form the core of the *T-Rex* spheres, with some multilayer regions where we find an overabundance of spheres. On the other hand, with regard to dilution D1 (1:1), there is an excess of SiO_2 spheres that do not allow interaction with perovskite, since it does not penetrate between the spheres but remains on the surface. For these reasons we conclude that the dilution, that best suits our applications, is the dilution D2. To achieve this conclusion it was necessary to make a set of samples differing exclusively for the dilution and compare the results by means of of micro-PL and macro-PL measurements that we will discuss in the followings. The samples I prepared are summarized in tab.2.1 with different dilutions. I deposited, by ALD, a TiO_2 film of different thicknesses (25÷100nm) to form the shell of the *T-Rex*. Finally I deposited on top a film of $CsPbBr_3$ by the Spin-coater, with dilution of precursor salt $PbBr_2$ of 0.17 M and 0.017 M. For spinned samples, $CsPbBr_3$ was synthesized by the following technique: the precursor salts $PbBr_2$ and CsBr were dissolved in DMF at 75 °C and methanol at 50 °C respectively. Then 100 µL of $PbBr_2$/DMF was deposited by spin-coating on the metasurface and dried at 75 °C for 30 minutes. At the end of this process, the sample was immersed in a $CsBr$/methanol solution kept at

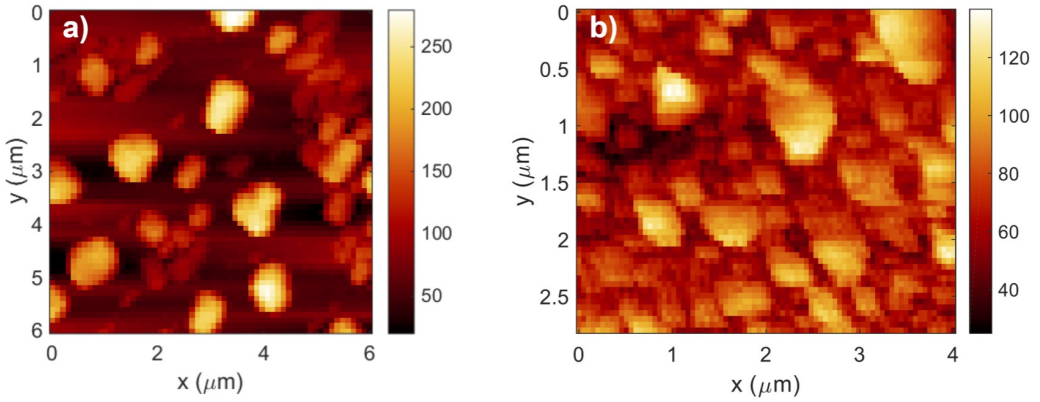

Figure 4.4. SNOM maps of a spin-coated (a) and a RF-MS (b) $CsPbBr_3$ sample on a soda lime glass substrate.

50 °C for 15 min and rinsed with 2-propanol afterwards. Finally, to evaporate the solvent, the sample was dried at 150°C for 30 minutes. I also investigated samples prepared by Radio Frequency-Magnetron Sputtering. $CsPb_3$ powder was obtained the grinding of the two precursor salts (CsBr and $PbBr_2$) in equal molar ratio in a mixer mill (Retsch model MM400). The sputtering target (5 cm diameter disk) was realized by pressing the perovskite powder by means of a pneumatic press (11.5 MPa working pressure) for 24 h at 150°C. The deposition was performed at room temperature with an RF power of 20 W and argon gas flow of 20 sccm. In these conditions,the deposition rate resulted to be in the range from 5 to 7 $\cdot$ 10^{-2} nm/s. The film thickness was monitored during the deposition by using a quartz crystal nanobalance until it reached the desired value. The comparison of samples realized with the two techniques allowed us to understand which is the best deposition technique depending on the application we have in mind. In fact, the deposition technique (spin-coating/RF-MS) determines a peculiar $CsPbBr_3$ crystallization on the substrate.

In fig.4.4 I report the topography maps, realized by the use of a *Scanning Near-field Optical Microscope*(SNOM) (spatial resolution $\approx 100nm$), of a $CsPbBr_3$ film deposited on glass by Spin-coater (a) and by RF-MS (b); the perovskite forms a more compact network of crystallites with a minor spread in size in (b) while using the spin-coating deposition (a) the perovskite crystals are more separated and with a greater size distribution [34].

When $CsPbBr_3$ is deposited on *T-Rex* substrate, what is obtained for the two different deposition techniques is shown in fig.4.5. From the SEM images of $CsPbBr_3$ films deposited on T-Rex, it can be seen that the perovskite forms microcrystals between the microspheres in the case of Spin-coating (fig.4.5(a)), while if it is deposited through RF-MS (fig.4.5(b))) nanocrystals are observed above the spheres. These nanocrystals are of about the same size, and they are placed above the *T-Rex* spheres in a rather homogeneous way. This is a rather different behavior from the deposition with Spin-coater that shows crystals of larger dimensions, different from each other, not very homogeneous, mostly placed between the spheres. The main consequence of the different arrangement between crystals and spheres when spin-

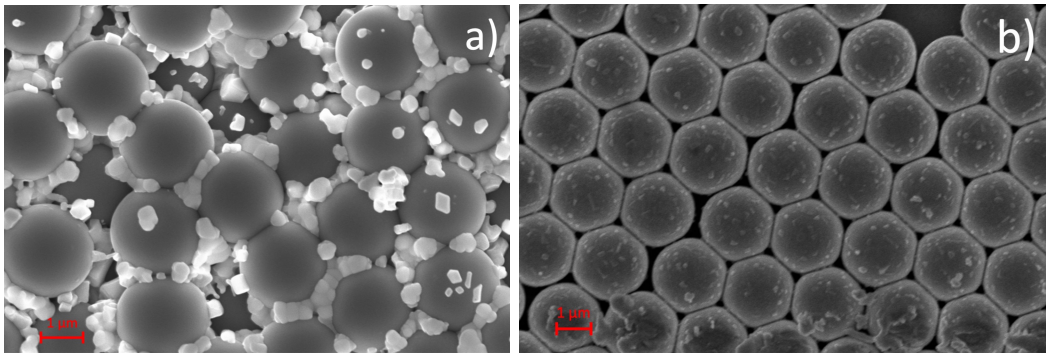

Figure 4.5. SEM images of a spin-coated (a) and a magnetron-sputtered (b) $CsPbBr_3$ sample on *T-Rex* (2 µm diameter; 100 nm TiO_2).

coating or sputtering is used shows in the light diffusion as I will discuss in the followings.

In Fig.4.6(a,b) typical SEM images for spinned samples with 2 µm and 6 µm *T-Rex* diameters are reported respectively, showing the presence of nanometric crystals of $CsPbBr_3$ whose distribution in size and position on the substrate is not homogeneous. From the SEM images (Fig.4.6) we can observe how perovskite crystallizes between the *T-Rex* spheres. In particular, for samples with *T-Rex*, nanocrystals are formed mostly between the spheres ((Fig. 4.6(a,b). We report the images of samples with 2 and 6 µm *T-Rex* diameters, but a similar situation is also found for the other samples studied (tab.2.1), provided that the perovskite was spinned, as we have seen in fig.2.10. On the other hand, if we observe the morphology of sample without the presence of the *T-Rex* spheres, in which the perovskite is deposited directly on the TiO_2 layer on the silicon substrate (Fig. 4.6 (c)), the $CsPbBr_3$ film is more compact with a density of microcrystals at least one order of magnitude higher respect to samples with beads. Also the $CsPbBr_3$ crystal size is greater respect to what found in (a) and (b). Therefore, it turns out that, despite the same procedure used in the spin-coating deposition, the presence of the spheres modifies the perovskite assembly. In Fig. 4.6(d) a SEM image of different parts of the *T-Rex* bead is shown.

A room temperature optical characterization of the samples was performed detecting the PL by the use of the SNOM in a illumination/collection configuration and a home-made confocal microscope (hereafter indicated as *micro-PL*). By means of the SNOM setup the sample was excited with a diode laser at 405 nm coupled into a chemically etched optical fiber. By a spatial scan of the sample, the PL spectrum was acquired in each tip position through the same probe, and the PL dispersed by a spectrometer was detected by a liquid nitrogen cooled CCD camera with a spectral resolution of 0.4 nm. In Fig.4.7 we report the results of a 6 µm×6µm SNOM scan performed on a sample with 2µm *T-Rex* beads: the spatial step is 100 nm. The sample topography shown in Fig.4.7(a), and overlapped with the PL map integrated in a [506÷550] nm wavelength range, confirms the SEM analysis with a localized emission around the spheres which appear in dark-blue. In Fig.4.7(b) it is reported a typical SNOM PL spectrum acquired in the point of maximum intensity of the map. Even though the high SNOM resolution allows to explore in great detail

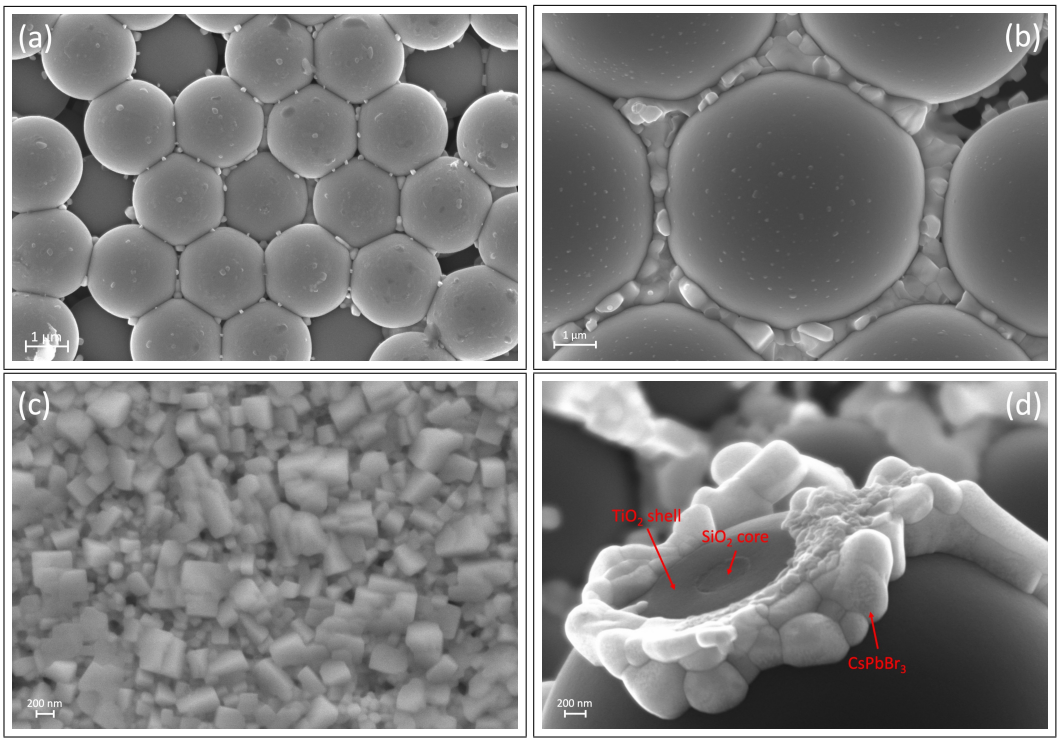

Figure 4.6. SEM images of samples with 2 µm (a) and 6 µm (b) *T-Rex* diameters. Same image of the sample without *T-Rex* (c). SEM image of the parts of sample with 2 µm *T-Rex* microsphere (d).

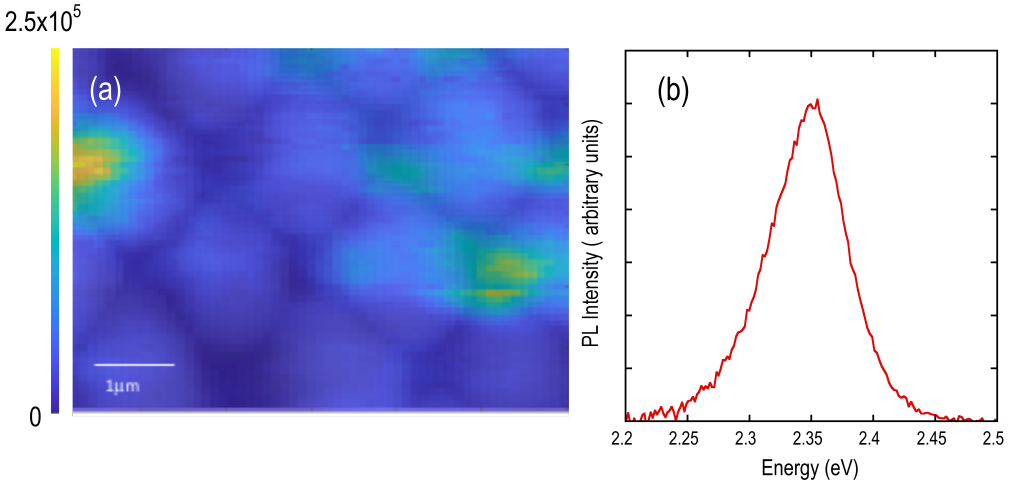

Figure 4.7. (a) SNOM PL map of sample with 2 µm *T-Rex* beads. The color map provides, for each pixel, the spectrally integrated PL intensity in the range 2.2÷2.5 eV. (b) typical PL spectra as from the SNOM map.

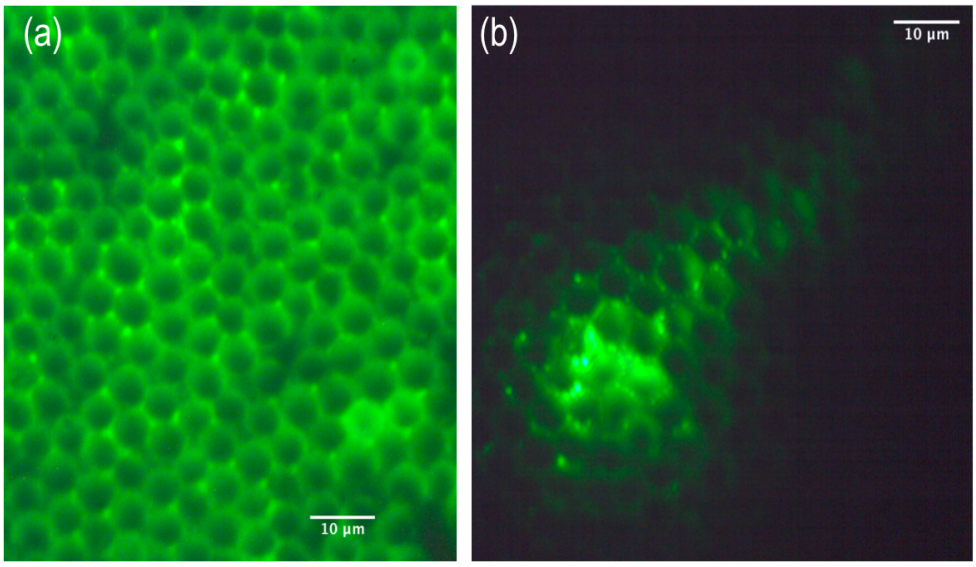

Figure 4.8. (a) Micro PL image of the sample with 6 µm *T-Rex* beads after excitation of a large spot on the sample with a 355 nm laser. The image is collected with a camera filtering the PL with a low pass filter at 500 nm. (b) Micro PL image of the same sample after excitation of a micron-sized spot with a 405 nm laser. The image is collected with a camera filtering the PL with a low pass filter at 500 nm.

micron-sized region of the sample identifying the nanocrystals position, the size of the *T-Rex* limits the possibility of using this tool when the bead diameter is >2 µm.

4.2 PL diffusion

In order to highlight the morphology of the sample in a wider region we used a room temperature *micro-PL* setup (fig.2.14) to excite the sample and collect the PL image with a spatial resolution of 1 µm. In fig.4.8 the PL image of sample with 6 µm *T-Rex* beads as detected by a CCD camera with a low-pass filter at 500 nm is reported after excitation of a wide sample region (Fig.4.8(a)), using the microscope only in collection mode; in Fig.4.8(b) we excite and collect the PL through the microscope having therefore a micron-size excitation spot. It is evident the beads network with the perovskite crystals between the spheres (in dark) with a PL emission at $\sim$ 532 nm from $CsPbBr_3$ and, as shown in Fig.4.8(b) the strong diffusion of the PL, indicating an efficient coupling between the spheres and the nanocrystals. This has allowed us to understand how *T-Rex* spheres and perovskite crystals match each other, modifying the typical $CsPbBr_3$ PL spatial emission. Similar situations, although less pronounced, are also found for other spheres diameters, provided $CsPbBr_3$ has been deposited by spin-coating. In fig.4.9, as an example, I show the image of diffusion of the PL for a sample having 411 nm spheres diameter with 100 nm shell thickness obtained by the micro-PL setup compared with the image of the laser spot taken at the same time, filtered with a 500 nm filter. The comparison therefore shows that the presence of the *T-Rex* spheres generate a diffusion along a large part of the

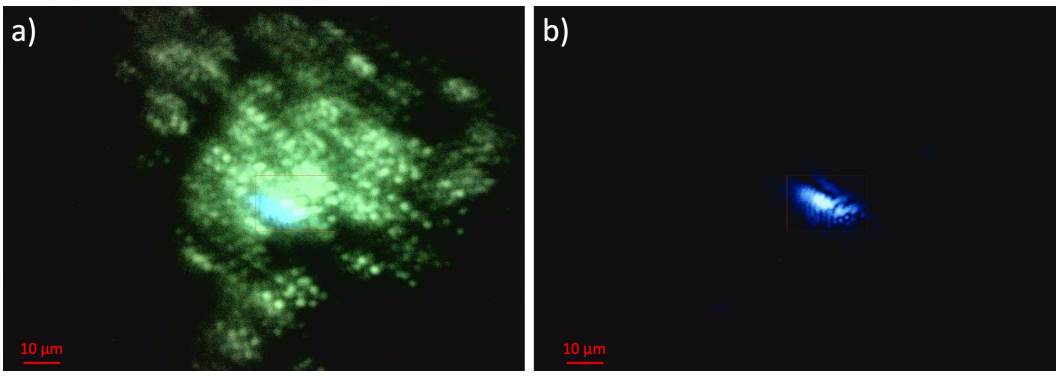

Figure 4.9. Photoluminescence diffusion collected with a camera and a low pass filter at 500 nm (a) and the spot laser of 405 nm (b) for a sample with 411 nm *T-Rex* diameter spheres and 100 nm of TiO_2.

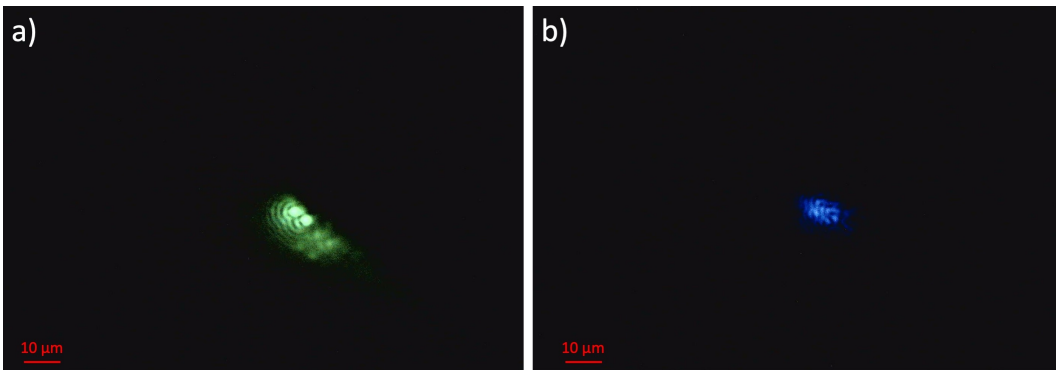

Figure 4.10. Photoluminescence diffusion collected with a camera and a low pass filter at 500 nm (a) and the spot laser of 405 nm (b) for a film of $CsPbBr_3$ deposited on soda-lime glass.

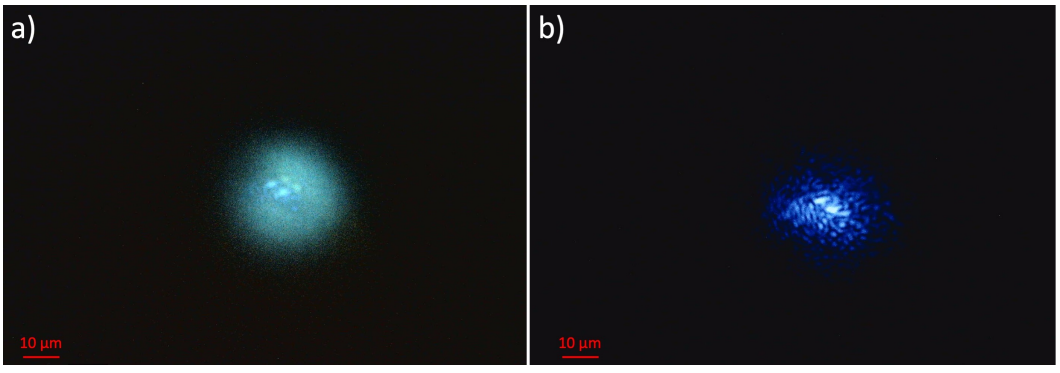

Figure 4.11. Photoluminescence diffusion collected with a camera and a low pass filter at 500 nm (a) and the spot laser of 405 nm (b) for a sample with 755 nm *T-Rex* diameter and 100 nm TiO_2 tickness: in this case $CsPbBr_3$ is deposited by RF-MS.

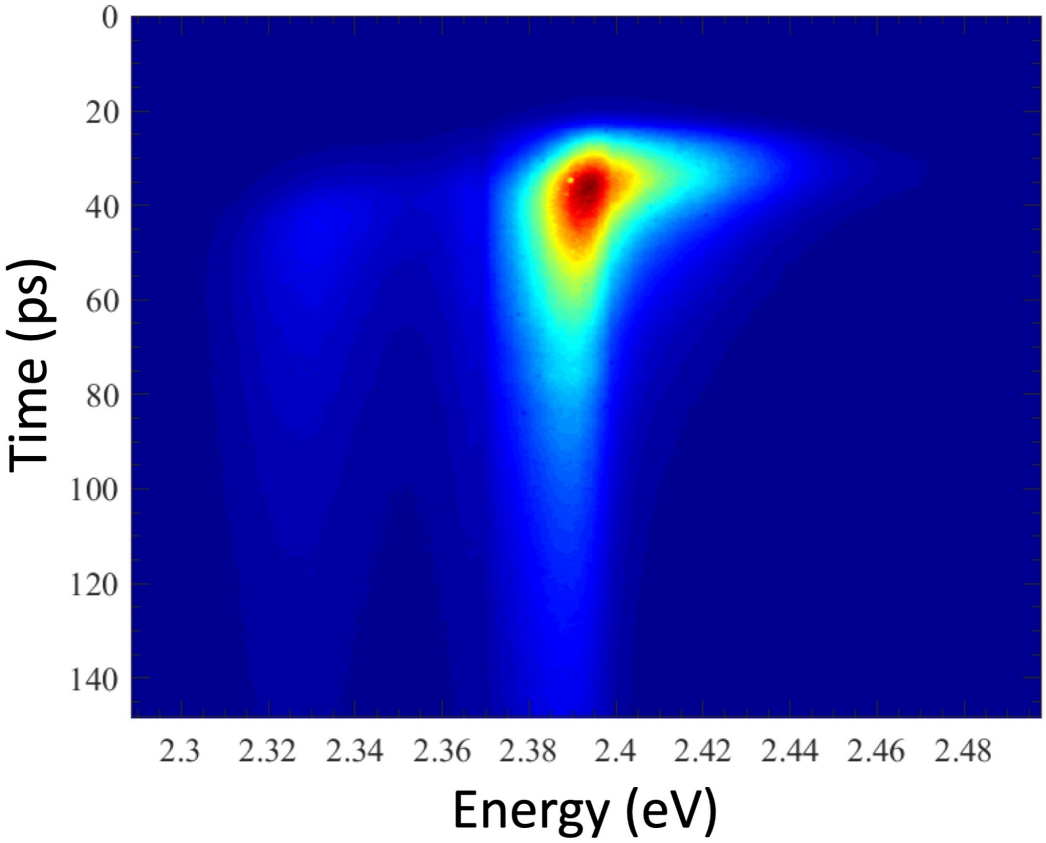

Figure 4.12. Time resolved PL streak image of sample 1 (see Tab.4.1).

.

sample surface while the excitation spot is of a few micron size. This experimental finding has been observed in all spin-coated samples of tab.2.1. The fact that PL propagates in this way between the spheres could be attributed to an interesting link between T-Rex spheres and perovskite. In fact, if we deposite $CsPbBr_3$ on a substrate like a soda lime glass and observe the PL emission no relevant diffusion of the PL is found (fig.4.10). Indeed, in this case the size of PL is comparable to that of the laser spot.

Similarly, for samples with beads where the perovskite has been deposited by RF-MS, PL does not show any relavnt diffusion (fig.4.11). It is worth noting that the halo observed is mostly due to the presence of the TiO_2 layer.

4.3 CW and TR PL measurements

To elucidate if perovskite and *T-Rex* spheres interact I studied the samples of Tab.4.1 by means of the MPL (Fig.2.12) and µPL setup (Fig.2.14), doing CW and TR PL measurements. Using a streak camera as detector, I got time-resolved PL maps (Fig.4.12): from this kind of maps we can get information on the recombination dynamics. By the map, I can extract both the time-resolved PL spectra and the decay of PL at fixed energies.

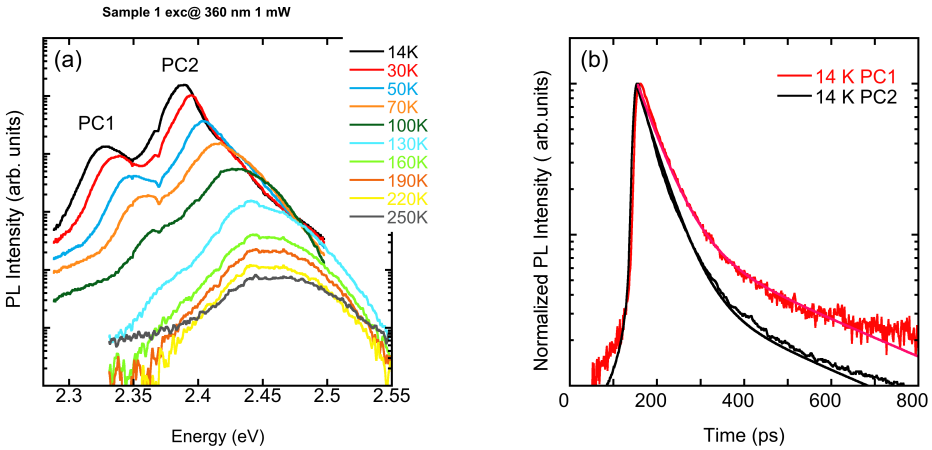

Figure 4.13. (a) Photoluminescence spectra of sample 1 as a function of temperature.(b) PL time decay at the energies PC1 e PC2 at 14 K extracted from fig.4.12.Solid lines are a two exponential fit.

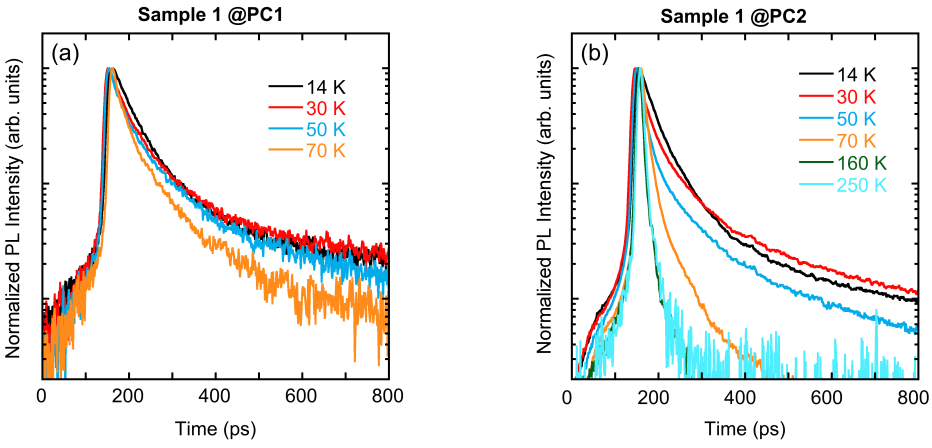

Figure 4.14. Sample 1: (a) PL decays at PC1 versus T. (b) PL decays at PC2 versus T.

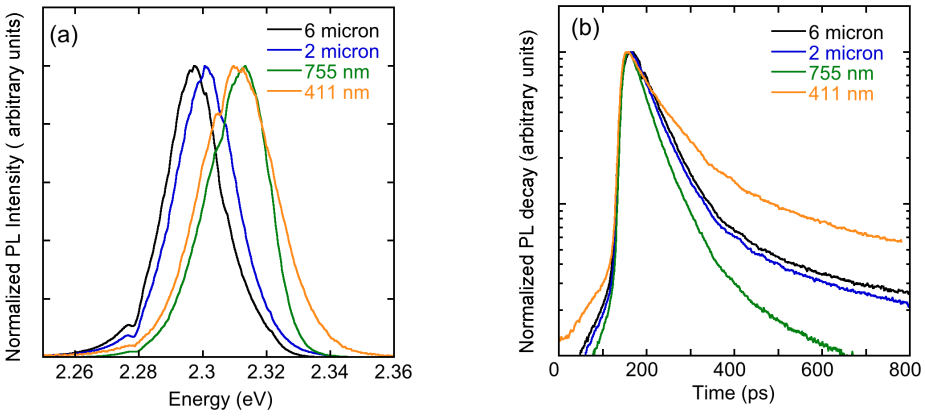

Figure 4.15. Spin coated samples differing for the bead diameter. T=15 K (a) PL spectra in focus mode. (b) PL decays at the PL peak energy.

In Fig.4.13(a) the PL spectra are reported varying the temperature. As commonly found the PL broadens increasing T and at the same time a significant PL quenching occurs. PL time decay at the energies PC1 e PC2 at 14 K extracted from fig.4.12 are shown in Fig.4.13(b) at low T and for different temperatures in Fig.4.14. As commonly found the PL decay cannot be described by a single exponential. Solid lines in Fig.4.13(b) are fits with a sum of two exponential functions with time constant $\tau_1 = (45 \pm 5)$ ps and $\tau_2 = (350 \pm 20)$ps. These values substantially agree with reports in literature [40]. The band indicated as PC1 corresponds to the PL of $CsPbBr_3$. The origin of the emission at PC2 is not clear; in fact it was also observed in sample 3 where no beads are present. In samples prepared with different bead diameter by RF and spin-coating, time resolved data show only a PL band centered at ≈ 2.31 eV in agreement with the $CsPbBr_3$ emission.

The comparison of the PL spectrum and time evolution for spinned samples differing for the bead diameter is reported in Fig.4.15

A clear trend is registered: decreasing the bead diameter from 6µm to 755 nm the fastening of the PL decay suggests a better coupling between the perovskite and the bead; for a further decrease of the size (411nm) the PL decay gets slower indicating a lack of coupling. SEM analysis of the 411 nm sample indicates a coverage of the beads: therefore we believe that in this case we are observing the film of microcrystals on top of the beads, mostly equivalent to the sample without beads.

Therefore, understood that the presence of the *T-Rex* could benefit the radiative recombination, it was necessary to understand which were the diameters that best interfaced with the perovskite.

From the SEM results, it was clear that the shell thickness that best suited our purposes is 100 nm. In fact, in spin-coating deposition, the best packing of perovskite with beads occurs when the *T-Rex* spheres have a 100 nm shell, allowing the crystals to nicely grow between the spheres. This produces a more homogeneous sample. When using shell thicknesses less than 100 nm, we reconfigured that during

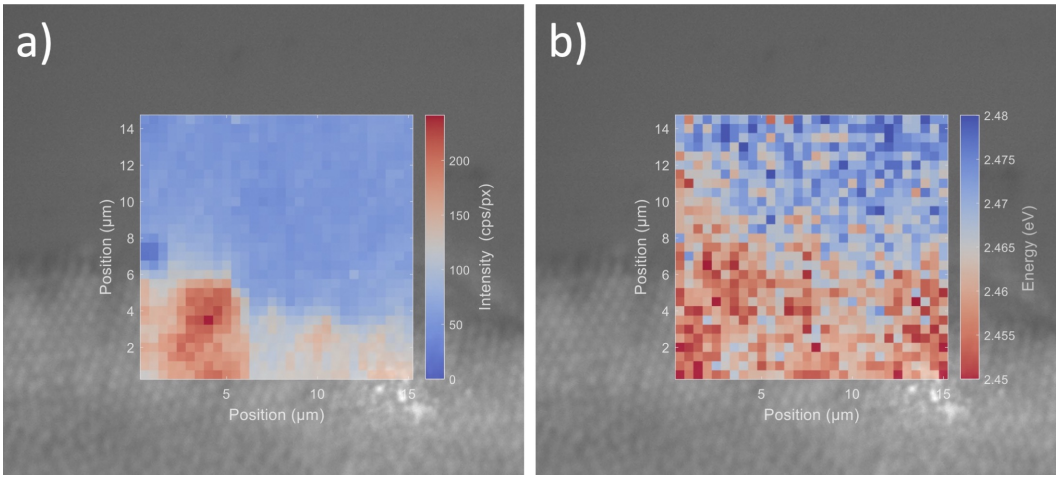

Figure 4.16. Intensity map (a) and energy map (b) of $CsPbBr_3$ deposited on *T-Rex* (755 nm, 100 nm of TiO_2) by RF-MS.

synthesis perovskite scratched the spheres in some areas of the sample by positioning itself below them. The film of TiO_2, in addition to defining the shell of the *T-Rex* spheres, acts as a protector of the beads keeping them packed, anchored to the substrate of Si.

By means of the confocal microscopy set-up (Fig.2.14) we got the PL intensity and energy maps of the samples. These measurements allow to understand if the presence of *T-Rex* brings an increase or decrease in the intensity of the PL emitted by the sample. In Fig.4.16 I present the intensity and energy maps for a sample with 755 nm *T-Rex* diameters and 100 nm TiO_2 thickness in which the perovskite was deposited by RF-MS. In particular, the Fig.4.16 shows the image of the sample, with a part without beads, where the TiO_2 layer and the $CsPbBr_3$ were deposited directly on the Si substrate, and a part with *T-Rex* spheres, on which the relative maps of intensity and energy have been superimposed. Then from these maps we can compare the emission originating from the two parts of the sample on which the perovskite was deposited at the same time. It turns out that the *T-Rex* microspheres produce an enhancement of the PL intensity. In fact, the emission of $CsPbBr_3$ deposited on the nanospheres by RF-MS is a factor four greater than the emission of perovskite deposited directly on the Si substrate (Fig.4.17(a,b). An energy shift is also observed, probably linked to the strain of the material (Fig.4.17(a,b)).

In the previous section (4.1), we have seen how the deposition techniques are essential in the homogeneity of the samples, in the assembly of the perovskite crystals with *T-Rex* spheres and, consequently, in the PL emission by $CsPbBr_3$. Therefore, it is necessary to compare the PL spectra and the PL decays at fixed energy for samples synthesized with different technique, spin-coating and RF-MS. Using the MPL setup (Fig.2.12), I obtained the TR- PL maps of Fig.4.18 for a sample deposited with RF-MS (Fig.4.18(a)) and one with spin-coating (Fig.4.18(b)). There is a slight difference of ≈10 meV in the PL peak energy being the emission of the sputtered sample at higher energy: this is in substantial agreement with the SNOM results of Fig.4.4 that indicate crystals of smaller size in the RF-MS sample, giving rise to a blue-shift of the PL. The faster decay observed in the case of the spin-coated sample

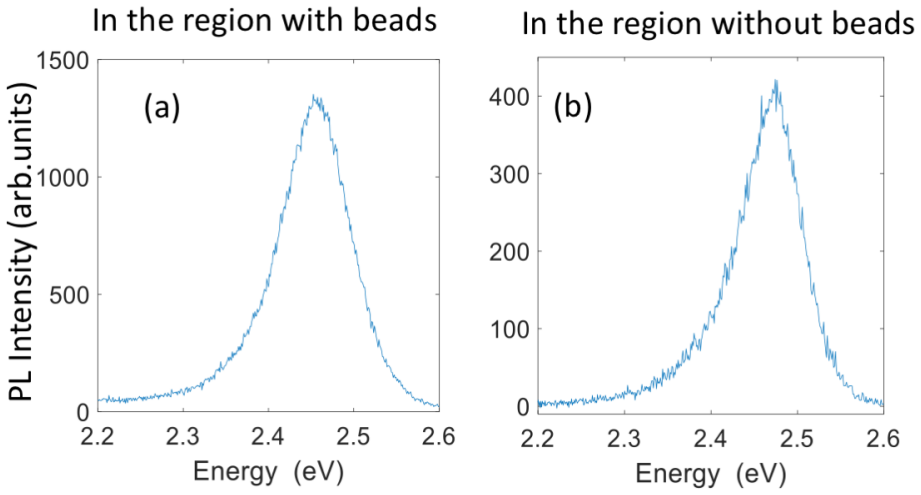

Figure 4.17. PL spectrum detected in the sample region with beads (a) in sample region without beads (b) as extracted from Fig.4.16.

suggests a good coupling with the *T-Rex* beads which are decorated by the crystals (Fig.2.10, while in the case of the sputtered sample we have a partial coverage of the top of the beads (Fig.:2.8. Therefore, we conclude that the synthesis techniques not only change the homogeneity of the sample and its morphology, but also act on the intrinsic properties of the material.

We have already seen in the Section 4.1 how in spin-coated perovskite samples there are strong PL diffusion effects (Parag.4.2) respect to perovskite magnetron sputtered samples that showed no effects of PL diffusion. The from TR-PL spectra we have found a difference in the recombination time, dependent on the bead diameter. These results bring evidence of a coupling between the microcrystals and the beads. In the next paragraph I will show how this coupling affects the amplification of the spontaneous emission (ASE).

4.4 Amplified Spontaneous Emission ASE

In this section I present results of PL spectra of samples realized spinning $CsPbBr_3$ on metasurfaces with 2μm (Sample A) and 6μm (Sample B) *T-Rex* diameter; a sample where $CsPbBr_3$ was deposited directly on the TiO_2 layer on Si (Sample C) is also shown for comparison. For these experiments we used the macro-PL setup(Fig.2.12), exciting the the samples in a quasi back-scattering geometry; the collected PL was dispersed by a 50 cm flat-field spectrometer and detected by a cooled CCD camera . We used two different laser sources reported in tab.2.2: the pulsed laser at 266 nm and the continuous wave (CW) laser at 450 nm so to provide different excitation conditions referring to the number of photons. Samples were kept in a closed-cycle cold finger cryostat so to vary the temperature in the range 10-300 K.

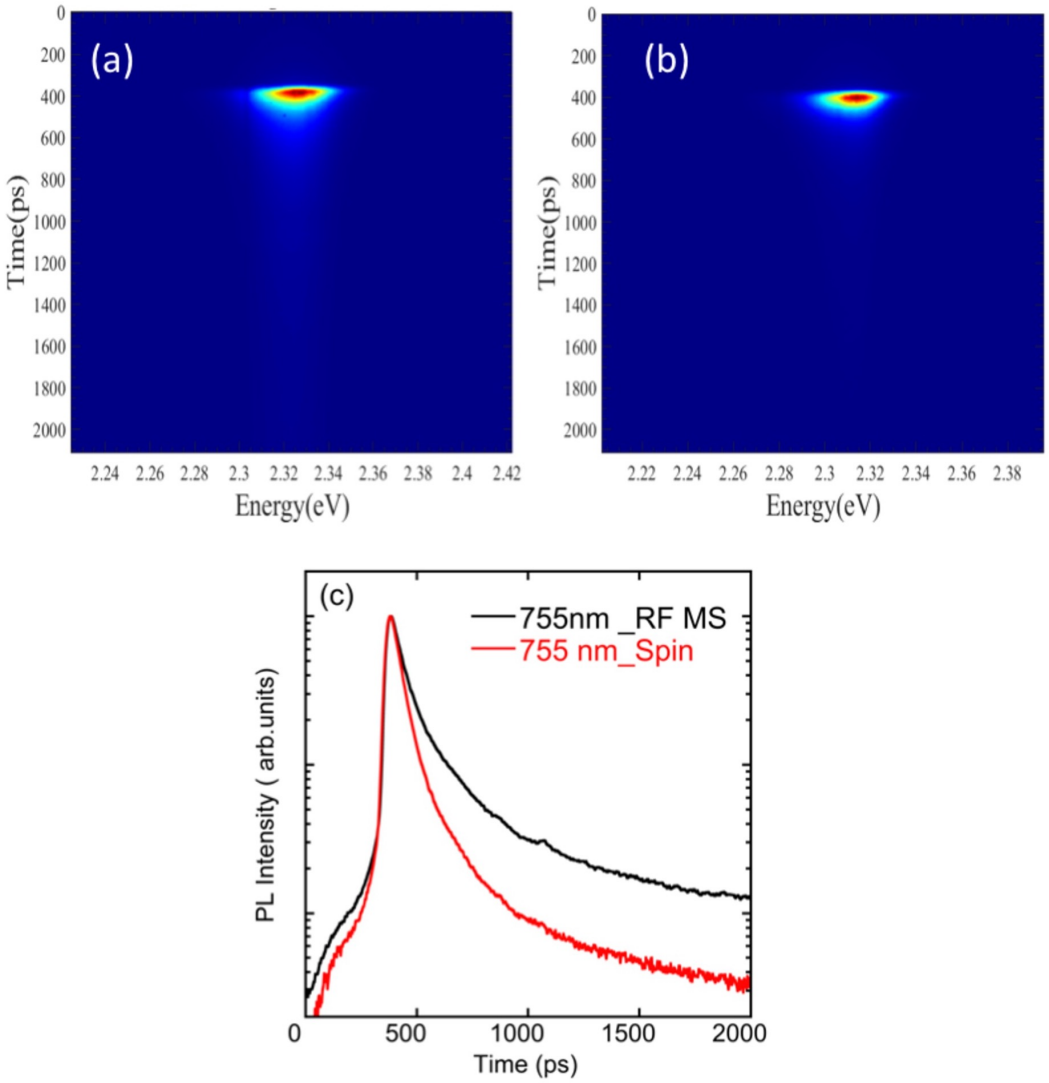

Figure 4.18. TR-PL maps for the sample with 755 nm microspheres diameter obtained by RF-MS (a) and by spin-coating (b). The PL decays at the PL peak energy are reported in (c) as extracted from (a,b).

First of all, I present PL spectra after CW excitation at 450 nm (2.76 eV), and then I compare them with the results obtained by exciting the samples with 300 ps pulses at 266 nm (4.66 eV). It is worth noting that in both cases a significant excess of energy with respect to the band-gap energy (2.3 eV) is provided to the carriers.

In Fig.4.19 low temperature PL spectra are shown varying the excitation power at 450 nm in the range 0.5 µW-1400 µW for sample A and C. Sample C (Fig.4.19(b)) shows an emission peak at 2.293 eV coming from the exciton recombination of micron-sized crystals and the PL full width half maximum (FWHM) is 18 meV in agreement with literature results for spin-coated samples [135]. Moreover a minor contribution to PL comes from a an higher energy shoulder at 2.32 eV possibly due excitonic recombination from $CsPbBr_3$ nano-sized crystals [34]. Sample A shows a PL peaked between 2.302 and 2.308 eV depending on the position of the excitation spot and the FWHM varies between 20 and 22 meV (Fig.4.19a). The blue-shift (10÷15 meV) observed in sample A (Fig.4.6(a)) can be ascribed to the reduction in the size of the micro-crystals respect to sample C (Fig.4.6(c))as reported from the SEM analysis.
Quite remarkable is the similar value of the PL intensity when comparing sample A and C at the same excitation density. In fact, if we take into account the ratio between the volume of excited halide perovskite in the two different samples as from the SEM images, we would expect that the PL intensity of sample A was at least an order of magnitude lower than sample C. Moreover, we cannot ascribe such finding to sample inhomogeneities which at maximum can account for a factor 2. Therefore, in our opinion this result is a strong indication that the metasurface structure optimizes the extraction of light from the sample.

When the PL spectra for different excitation power are normalized to the maximum of the emission (Fig. 4.19(c)), it turns out that the line shape remains the same except for the low energy tail which shows a saturation for the highest excitation condition. In Fig.4.19(d) I report the PL spectrally integrated intensity as a function of the power P_{exc} for the different samples along with the fit with a power law

$$I_{PL} \sim P_{exc}^{\alpha} \tag{4.1}$$

The α coefficient is between 1 and 1.1 for all the samples; this indicates a linear dependence of the PL over four orders of magnitude in a generally speaking low excitation condition as the one provided by the CW laser.

A different scenario is found when the excitation occurs by the 300 ps long pulses as shown in Fig.4.20.

For all samples, when the average power is ≥1 mW, corresponding to pulse energy ≥50 nJ, narrow peaks appear (hereafter indicated as *modal* structure), at the limit of the setup resolution, and the emission increases superlinearly. The observed phenomenology is similar to what is reported in the literature relating to the establishment of an ASE and/or random lasing regime [123, 10, 155]. Increasing the lattice temperature the presence of the *modal* structure persists up to ≈ 150 K as shown in Fig.4.20(d). Above 150 K the spectrum is smooth with no relevant feature. It should be pointed out that the perovskite nanocrystals maintain the orthorhombic phase up to the temperature of 350 K [126] and therefore the observed effects cannot be associated with a structural phase change. The emission shifts

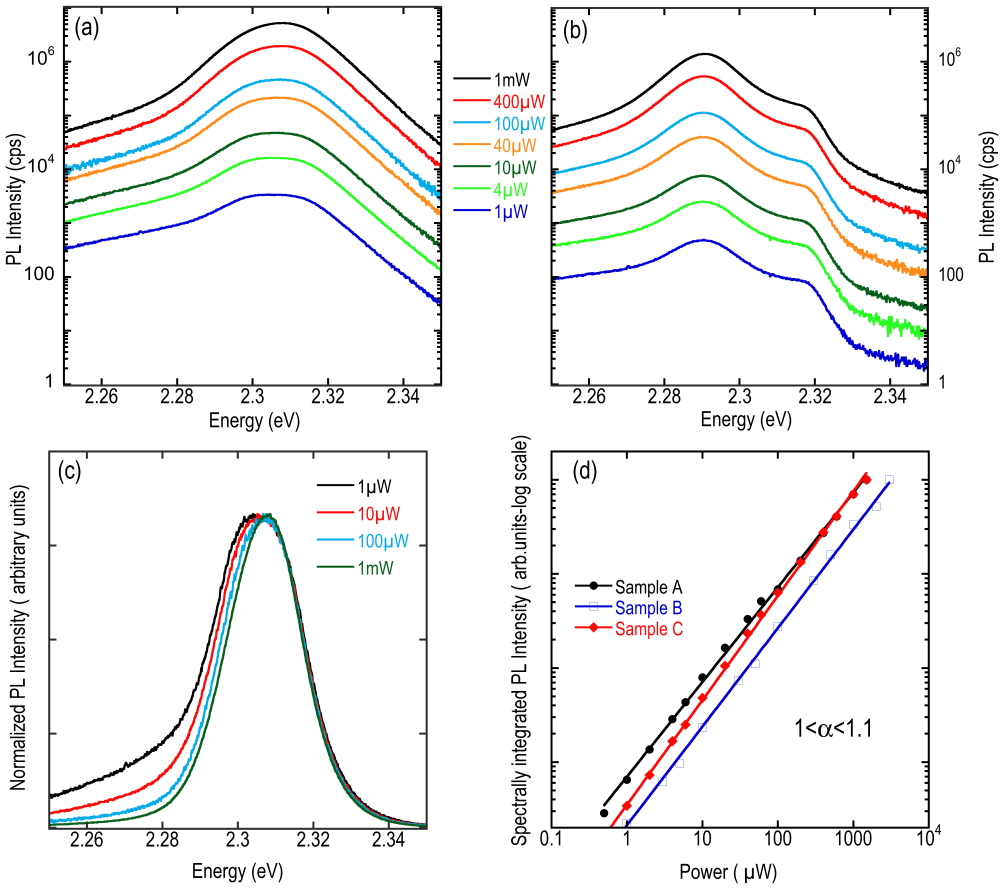

Figure 4.19. PL spectra at $10K$ as a function of the power under CW excitation in log scale (a) sample A (2μm bead), (b) sample C (no bead), (c) normalized PL spectra of sample A for different excitation power, (d) Dependence of the spectrally integrated PL on the excitation power for sample A ,B (6μm bead),C. The solid line is a fit with a power law and α is the power law exponent.

.

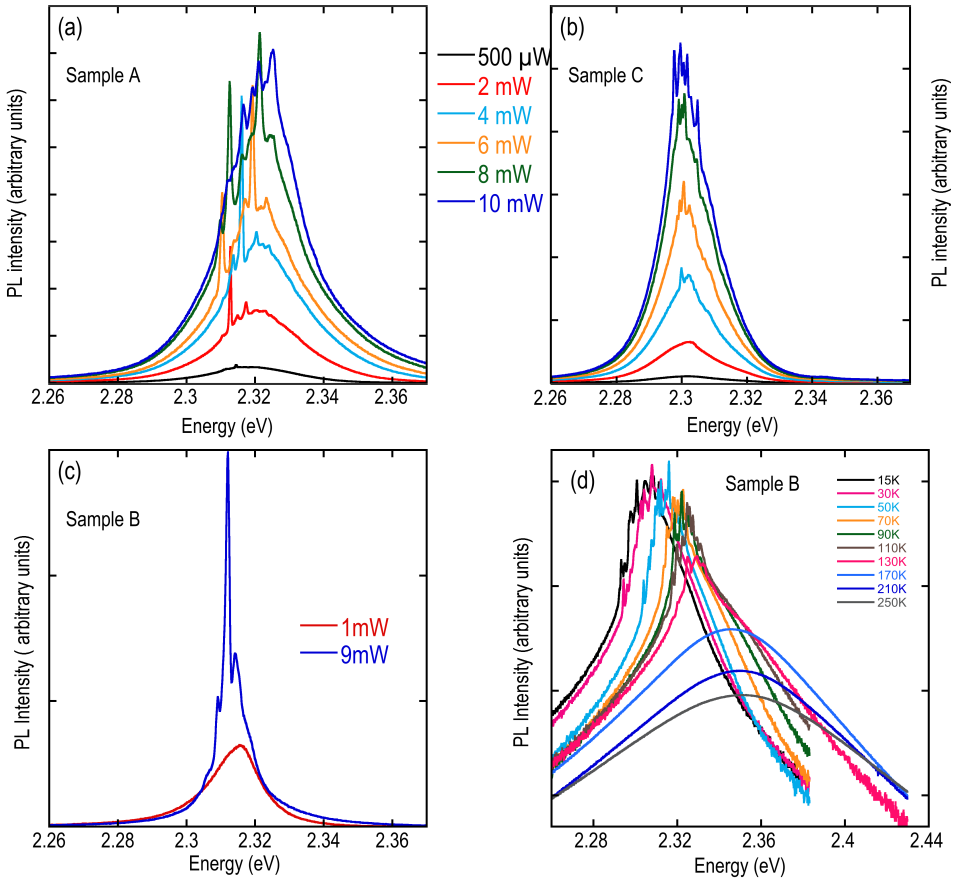

Figure 4.20. PL spectra after excitation with pulses at 266 nm at 10 K: sample A (a), sample C (b), sample B (c). Temperature dependence of the PL for sample B (d).

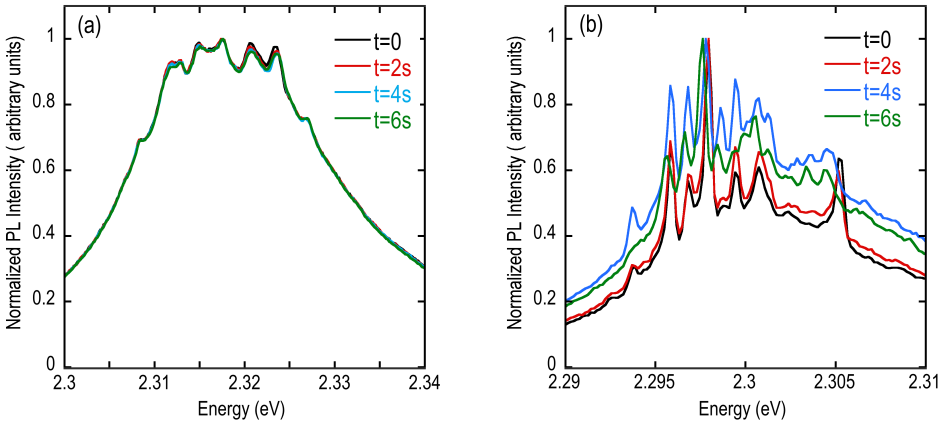

Figure 4.21. PL spectra after excitation with pulses at 266 nm at 10 K. Spectra have been acquired in a kinetic mode as discussed in the text. For each spectrum the time of acquisition is indicated: sample A (a), sample C (b).

towards high energies with the increase of temperature and the shift is in agreement with the variation of the band gap energy of $CsPbBr_3$.

In Fig.4.21 I report the PL spectra, in the region where modes are present, acquiring the signal in a kinetic mode. In thsi case the spectrum is acquired with a short time of exposure (21 ms), asynchronous with the laser pulse and the acquisition is repeated in sequence with a time delay as indicated in the figure. It clearly appears that the modal structure is stable in the case of sample A while it changes in sample C, suggesting that the presence of the *T-Rex* beads plays a role in stabilizing in time each mode. Let us now focus on the low temperature spectra; having the photoluminescence a linear trend with the excitation power (Fig:4.19), to highlight the presence of non linear effects we subtracted the lowest power spectra (0.5 mW) from each spectrum after having multiplied it by the appropriate factor to take into account the power value. This procedure removes the linear component of the emission, providing information on the remaining contribution, hereafter indicated as non linear contribution. The results are shown in Fig.4.22. Sample C, which is the film constituted by a disordered assembly of micro and nanosized crystals, shows a superlinear increase of the emission with several modes as indicated in Fig.4.22(b) and as expected for the ASE contribution.

In the case of sample A (Fig.4.22(a)) and similarly on sample B , three spectral regions are evidenced with a different dependence on the excitation power: the low energy side, below 2.31 eV, which shows a marked saturation provoking a negative contribution of the non-linear component, a region between 2.31 and 2.32 eV, corresponding to the peak emission, characterized by the presence of the modal structure superimposed to the saturated profile and above 2.32 eV a spectral band with a superlinear growth. If we spectrally integrate the non-linear contribution, over the whole band for sample C and in the three different spectral regions for

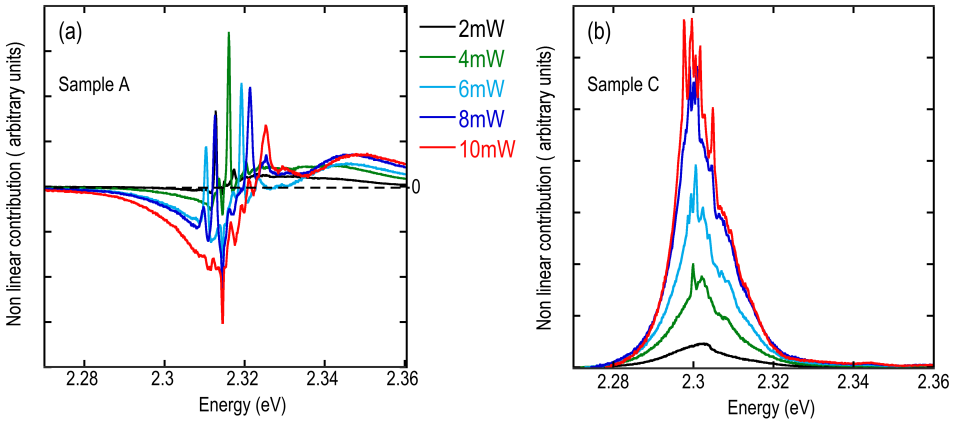

Figure 4.22. Non linear contribution at 10 K extracted from spectra of Fig.4.20 for sample A (a) and sample C (b).

sample A we obtain the results shown in Fig.4.23. The solid and dashed lines in the figure are fits of the non linear contribution according to a power law with β as exponent. It turns out that the results for sample C (Fig.4.23(b)) indicates the presence of ASE with a significant superlinearity even though in our experimental conditions the excitation energy is pretty low (at maximum 50 nJ per pulse).

A different scenario comes out for sample A (Fig.4.23 (a)): the superlinear growth of the high energy side arises from the recombination of free non-geminated charges with two different values of β, the lowest energy side bleaching originates from saturation of the localized states emission, while a linear dependence (shown as the flat dotted line in the figure) of the region centered at the peak is found up to 5 mW followed by a sublinear trend which is the same as the low energy side. Considering that the non-linear contribution has been spectrally integrated it is not surprising that even in the region where the modal structures are present we find a sublinear trend. However, if we focus on each modal structure (Fig.4.22) a slight superlinearity is recovered. We believe that the absence of a significant superlinear trend for samples A and B comes from the limited number of emitters present in the excited spot as indicated from the SEM images (Fig:4.6 (a,b)). Moreover the linear behavior below 5 mW with presence of modes suggests a condition of lasing action within a microresonator consisting in the *T-Rex* itself. Quite remarkable it is also the persistence of the non linear emission up to 150 K. Recent literature data show the observation of ASE up to 300 K in compact films of $CsPbBr_3$ after a heat treatment[101] that leads to a recrystallization with crystals of micrometric size bigger than those of the samples studied here. Therefore, the results here presented seem promising in particular with regard to the integration of perovskite in the metasurface of *T-Rex*. It is also worth noting that the experiments were performed in a quasi back-scattering geometry while most of the reports concerning the detection of ASE in halide perovskite samples were realized in a guided mode configuration

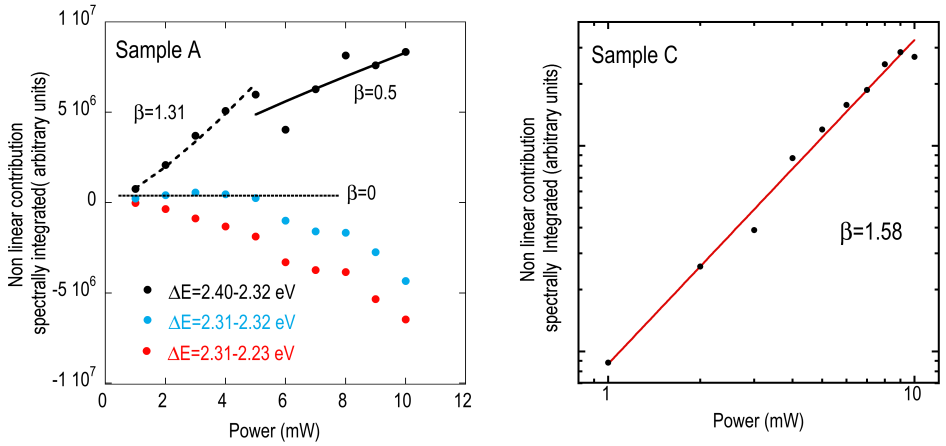

Figure 4.23. Spectrally integrated non linear contribution as from 4.22. (a) Sample A: the points refer to the spectral integration in different region of 4.22; the two lines correspond to a power law fit with two different values of β. (b) Sample C: the solid line corresponds to a power law fit with β indicated in the figure.

[140, 26]: this is a further evidence of the beneficial action of the metasurface in this case.

In order to theoretically verify the presence of enhancement in the perovskite emission in presence of the *T-Rex* spheres (sample A and B) with respect to the flat substrate case (sample C) we performed Finite Difference Time Domain (FDTD) simulations, employing the commercial software Lumerical. This simulations was made by Dott.ssa N. Granchi.

To simulate the emission from the perovskite, a spectrally narrow electric dipole x-polarized is used, centered around 2.34 eV (no changes are found when the energy is in the range 2.3÷2.36 eV) with a pulse length of 100 fs. To simulate the emission of sample C, the dipole is positioned on the substrate composed by a Si bulk and 100 nm thick layer of TiO_2. Then, the same dipole is positioned on top of a core-shell sphere with a diameter $d = 2\mu m$ (sample A) and $d = 6\mu m$ (sample B). In all cases, the intensity spectra are collected from a time monitor positioned at a distance of 400 nm from the dipole. A clear enhancement of the electromagnetic field intensity in both sample A and B (purple and green lines) is found with respect to the flat case. The maximum enhancement factor (4.5) is achieved for the biggest sphere, i.e. sample B. Simulations reported in the SI (S6) evidence the presence of MIE resonances in the spheres in the spectral region where $CsPbBr_3$ emits. Recent reports [140, 142, 153, 102, 138] indicate lasing from multiple gallery-whispering of single microresonators decorated with $CsPbBr_3$ quantum dots or nanocrystals. Our results suggest that lasing can eventually occur from the coupling of the hexagonal arrangement of microspheres: in the SI (S7) preliminary analysis is shown to verify this coupling condition.

In conclusion, the experimental results presented in the different sections of this chapter bring evidence of the beneficial coupling of $CsPbBr_3$ micro-crystals with

the *T-Rex* microresonators for what concern the light extraction, the change in the radiative decay time and the amplification of the emission.

Chapter 5

Conclusions

I conclude this thesis by summarising the results obtained during my PhD, which were addressed in the previous chapters. First of all I presented a detailed analysis of the Urbach tail, which is a characteristic feature that semiconductors with a degree of disorder show in the absorption spectrum. In particular, the focus of my study was the investigation of the nature of the Urbach tail in an inorganic halide perovskite, $CsPbBr_3$ by a deep analysis of the photoluminescence in different experimenental conditions. Provided that also hybrid halide perovskites show a similar behavior in the Urbach tail as reported in the literature, we are confident that our analysis can be extended to the whole class of these semiconductors. The experimental findings on a large set of samples, prepared with different synthesis/deposition methods, indicate a very similar behavior independent of the sample morphology (bulk, thin nanocrystalline films), thickness, substrate, and growth/deposition technique. Our results indicate that the Urbach tail has an origin ascribable to the dynamical disorder, induced by the lattice vibrations; the Urbach energy E_U, in a limited temperature range, is linearly correlated to the band-gap variation and the exciton energy E_b. While the dependence of E_U on T nicely follows the phonon population, the discrepancy observed for E_b from the expected intrinsic contribution, being strongly sample-dependent, has to be ascribed to an extrinsic phenomenology possibly related to strain release between grains in macrocrystal samples and between substrate and film in spin-coated and sputtered samples.

Another important result was obtained in the coupling of the *T-Rex* spheres with perovskite microcrystals. Starting from the synthesis of $CsPbBr_3$ and its integration with *T-Rex* spheres, I studied how this integration leads to *Light Diffusion*, *Random Lasing* and *Amplified Spontaneous Emission* (ASE) phenomena. In the study of these phenomena, we have reported on the non-linear emission in $CsPbBr_3$ films made by spin-coating on a semiconductor substrate and on a metasurface. A different morphology of the films is found depending on the presence/absence of the metasurface realized with *T-Rex* beads. In particular the comparison of the volumes

of excited material in the samples and the corresponding PL intensities indicates that the significant increase of the PL in presence of the *T-Rex*, originates from a better light extraction due to the presence of the beads. Measurements by varying the laser power used for excitation show a transition from a linear photoluminescence regime to a superlinear one with the appearance of modal structures in the spectral region of the PL maximum. While in the sample without the metasurface the phenomenology can be attributed to ASE, the mostly linear trend found for the modal structures in samples with the beads suggests that spherical micro-resonators promote a *real* lasing action. Moreover, from the analysis of the PL kinetic series it can be deduced that the deposition of perovskite on the metasurface helps to stabilize in time the modes produced.

Appendix A

Use of halide perovskite nanocrystals for water remediation; an explorative study

Climate change and environmental sustainability ask for a more efficient and circular waste management. In parallel, water and air purification is another major goal that challenges the scientific community to develop new materials, techniques and strategies. Moreover, there is a growing interest to produce green energy with low-cost materials. In particular, in the last decade, halide perovskites have received considerable interest from the communities of physicists of matter, chemists and materials scientists for the many possible applications to replace the classic semiconductors for photovoltaics, optoelectronics and sensors [56, 39]. In this Chapter we will show how halide perovskites can also be used as substrates for the absorption of pollutants. As an example, Methylene Blue (MB), a typical pollutant that can be found in water as waste of textile industry, has been considered. The final idea is the possibility to circularly reuse perovskites recovered from other applications, such as photovoltaics [5], and exploit their pollutant adsorption properties. In this way it is possible to create a double advantage for the environment: reduce the amount of solid waste and improve water quality.

In particular, I will show the results obtained during my PhD in the drainage of textile industrial pollutants, such as Methylene blue (MB), from the water used perovskite powder encapsulated inside chitosan bubbles, organic material derived from shrimp shells and recently used as a green pollutants adsorber [87]. This represents an innovative application for HPs perovskite usage, which has never been tested before. Here I will report the first preliminary results of this research activity, obtained in collaboration with Dott.sa M. Maddaloni, Department of Mechanical and Industrial Engineering, University of Brescia, which are still in progress.

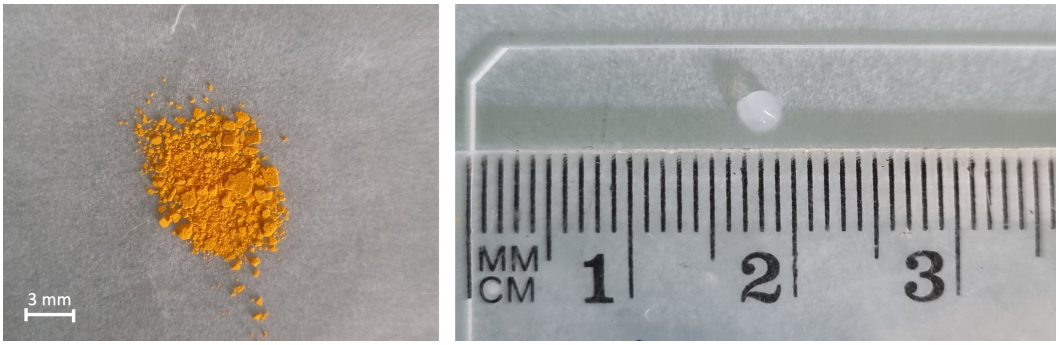

Figure A.1. $CsPbBr_3$ nano-powders (NPs) synthesized by the protocol described (a). Bubble of chitosan (b).

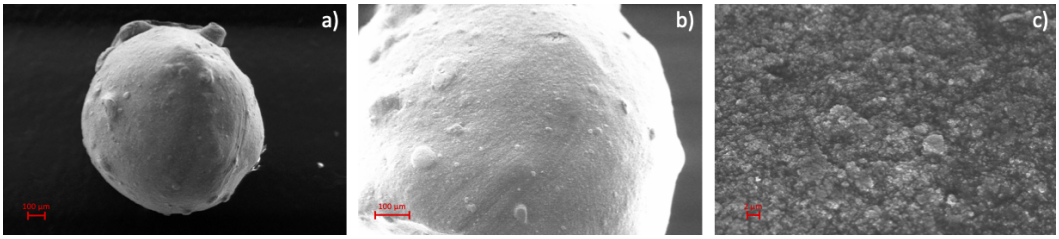

Figure A.2. SEM images, kindly provided from Prof. M. Ferroni, of dried $CH@TiO_2$ bubbles at a) 150X, b) 300X and c) 5000X.

A.1 Samples preparation and analysis setup

This research is focused on the use of $CsPbBr_3$ as absorbers of 10^{-5}M aqueous solutions of MB, which simulates a typical range of concentration of organic dye pollutants in textile industry effluents. For this application, the $CsPbBr_3$ was synthesized in powder (see Fig.A.1(a)) so that it can be dispersed within the aqueous solution of MB, thus directly using perovskite as an adsorber, and, in addition, so that it can be encapsulated inside bubbles of chitosan (see Fig.A.1(b)), then exploit the catalytic properties of perovskite and accelerate the processes of adsorption of pollutants, typical of chitosan.

In Fig.A.2 are shown three SEM images of a typical dried $CH@TiO_2$ bubbles at three different magnification that allows us to better appreciate the morphology of the bubbles. To obtain the SEM images, a drying process is required. For this reason, the Fig.A.2 represent only Bubbles of chitosan with TiO_2. The presence of Titania, in fact, allow us to maintain the rigidity of the sphere, otherwise compromised in the case of chitosan hydrogel alone, in which the Bubbles collapse after drying.

To synthesizes $CsPbBr_3$, the precursor salts $PbBr_2$ (0.17 M) and CsBr (0.035 M) were dissolved in DMF (Dymethylformamide) and Methanol (MeOH), respectively at the temperarures of 75°C for $PbBr_2$ and 50°C for CsBr for 5/10 min. Under magnetic stirring, the $PbBr_2$ was mixed with CsBr and the solvents were allowed to evaporate. Evaporation times depend on the amount of solvent. Once the powdered perovskite was obtained, it was cleaned in 2-propanol, in order to eliminate any solvent residue. The molar ratio between $PbBr_2$ and CsBr is important for the synthesize of the perovskite. In this research, four different molar ratios of $PbBr_2$/CsBr salt precursors,

namely 1; 1.9; 2.9 and 3.9, were investigated, leading to the systems called PVK 1, PVK 1.9, PVK 2.9 and PVK 3.9. The XRD analysis of the obtained powders confirmed the presence in all cases of the $CsPbBr_3$ phase, with a significant percentage of spurious phases for higher molar ratios. The analysis for the adsorption of the pollutants and its photodegradation was carried out using a UV-VIS spectrometer and illumination was performed by a solar simulator. In particular, we measured the percentage of MB contained in the aqueous solution, in direct contact with the adsorber, as time changes. This was possible through an adsorption setup in which the intensity absorbed by the aqueous solution containing the pollutant is measured as the absorption time changes. In fact, according to the Lambert-Beer law:

$$I = I_0 e^{-A} \tag{A.1}$$

where A is the absorbance, directly linked to the molar absorption coefficient, the molarity and the optical path ($A = \epsilon_\lambda l M$ where ϵ_λ is the molar absorption coefficient, l the optical path and M the molarity; the last two fixed), the light intensity is directly proportional to the concentration of the solution that can vary over time depending on the adsorber used. Therefore, we have a direct measurement on the concentration of the pollutant contained in the aqueous solution. So the study was carried out analyzing the percentage of MB adsorbed by the $CsPbBr_3$ nanopowders (NPs) as a function of time. In addition, to facilitate the manipulation of the $CsPbBr_3$ NPs and reduce any eventual Pb release in water during their employment as adsorbents/catalysts, they were incorporated into millimiter-sized hydrogel bubbles made of chitosan (CH), a biopolymer extracted from the waste of shrimp's shells. Chitosan bubbles (CH-BB) with the $CsPbBr_3$ NPs were obtained according to the following chemical procedure: 0.10 g of chitosan was dissolved in 10 mL of 5% (v/v) acetic acid to obtain a 10 g/L solution. The dissolution process was accelerated thanks to the use of an ultrasonic bath or magnetic stirring. As soon as the chitosan is dissolved, perovskite powder (1% w/v) is added and we wait for it to dissolve in the chitosan solution. The prepared solution was then poured dropwise by a syringe in a solution of 3 M NaOH, used as a cross-linker. The crosslinking step lasted 6 hours, at the end of which the obtained bubbles were recovered and washed with milli-Q water until a neutral pH was reached.

Pollutants absorption experiments were also conducted for this hybrid hydrogel composites, and compared with the absorption of analogous systems made of chitosan alone.

A.2 Results discussion

In this paragraph I show the results obtained for the absorption of MB in two systems: the use of perovskite NPs as adsorber of pollutants from aqueous solutions; the use of $CsPbBr_3$, encapsulated inside chitosan bubbles, to enhance MB adsorption from bubbles.

A.2.1 Pollutants adsorption from perovskite NPs

In order to investigate the capabilities of the different $CsPbBr_3$ samples (PVK 1, PVK 1.9, PVK 2.9 and PVK 3.9) concerning the pollutants adsorption, the synthesized

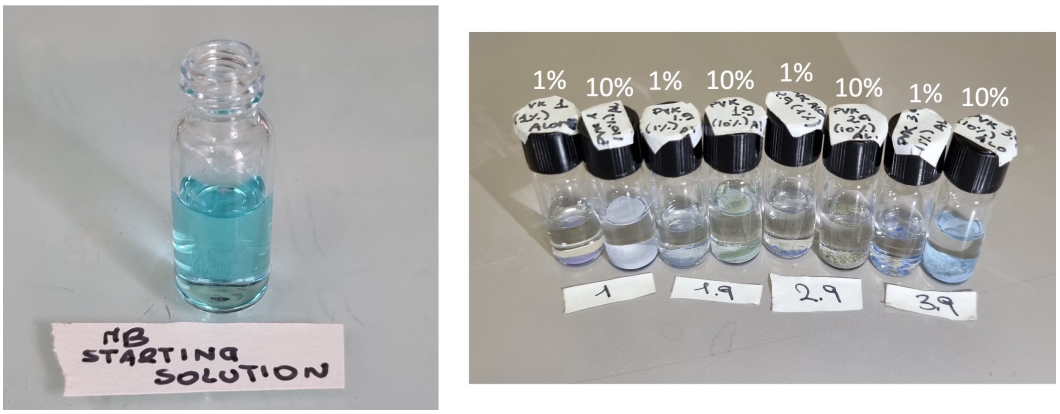

Figure A.3. MB starting solution (a). MB solutions adsorbed after 5 min by $CsPbBr_3$ NPs for different precursors salts molar ratio and in different percentages (1% and 10%) (b).

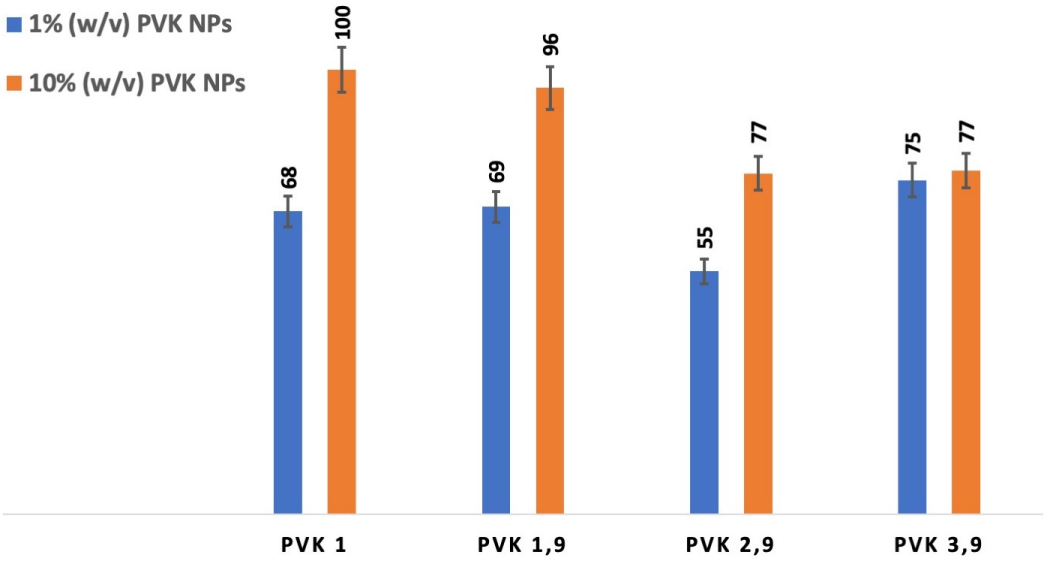

Figure A.4. Percentage of MB (starting concentration 10^{-5M}) after 5 min of contact with perovskite NPs at concentration 1% w/v and 10% w/v.

perovskite powders were simply put in contact with a MB aqueous solution. Starting from a MB solution 10^{-5} M, Fig.A.3(a), we measured the concentration of the pollutant remained in solution in fuction of time, according to the procedures described in the ParagraphA.1. Two different concentration of perovskite NPs were investigated: 1% (w/v) and 10% (w/v). As shown in Fig.A.3(b), a very reduced contact time between the MB and perovskite NPs is needed to obtain significant MB absorption: in just 5 min, a considerable adsorption of the pollutant is obtained. In Fig.A.4 its shown the Percentage of MB adsorbed by $CsPbBr_3$ NPs 1% and 10% for the different molar precursor salts ratio after 5 min of contact. In general, higher absorption is obtained when the perovskite powder loading is 10%. The absorption was confirmed both by the visual analysis, and by the UV-VIS analysis conducted through the spectrophotometer following the spectroscopy techniques described in ParagraphA.1. The samples prepared with a molar ratio of 1:1 (PVK 1) between the precursor salts show a greater MB absorption capability than the other ratios, with 10% of the adsorber in the solution. In particular, a complete adsorption of the MB can be obtained in only five minute when the PVK system is composed of pure $CsPbBr_3$.

A.2.2 Perovskite as catalyst in adsorption processes

When $CsPbBr_3$ is incorporated inside chitosan bubbles, the adsorption capability of the system is reduced, as enlightened by the fact that complete MB removal cannot be obtained even after 5 hours. Anyway, it is noteworthy that the incorporation of the perovskite NPs enables to enhance the absorption capabilities of bubbles made of pure chitosan. In Fig.A.5 its showed the MB absorption data related to various chitosan-perovskite bubbles, obtained by incorporating the different perovskite powders at 1%. This results have been obtained by the UV-VIS analysis, by measuring the concentration of MB absorbed at different times for a total of 5 hours. In contrast to what occurs in the case of $CsPbBr_3$ NPs in direct contact with the pollutant, the hydrogel systems BB-CH/$CsPbBr_3$ that show best adsorption capabilities (removal of 70% of MB after 5 hours contact) are those containing perovskite systems 1.9 and 2.9 molar precursors salts ratio (CH+PVK 1.9 and CH+PVK 2.9). Furthermore, unlike the absorption of MB by bare $CsPbBr_3$ NPs, the adsorption is greater and faster with a reduced percentage of perovskite inside the CH-BB: best results in the case of PVK loading equal to 1% w/v. In particular, the results show that the presence of perovskite inside the chitosan bubbles increase and speeds up the adsorption respect to chitosan bubbles alone and this could be a signal of perovskite stabilization in this hydrogel system, which requires further more in-depth analysis..

So, in the case of perovskite encapsulated into CH-BB, the time is longer but we have the advantage of being able to recover the perovskite once the adsorption process is over. These results open the way to the use of halide perovskite material as adsorbers for different pollutants in water. It is interesting to note that the use of chitosan brings us closer to a solution for the well-known stabilization problem of perovskite in water [47].

The study presented in this chapter is exploratory and preliminary. More in-depth analysis will be made both for the use of perovskite for the adsorption of

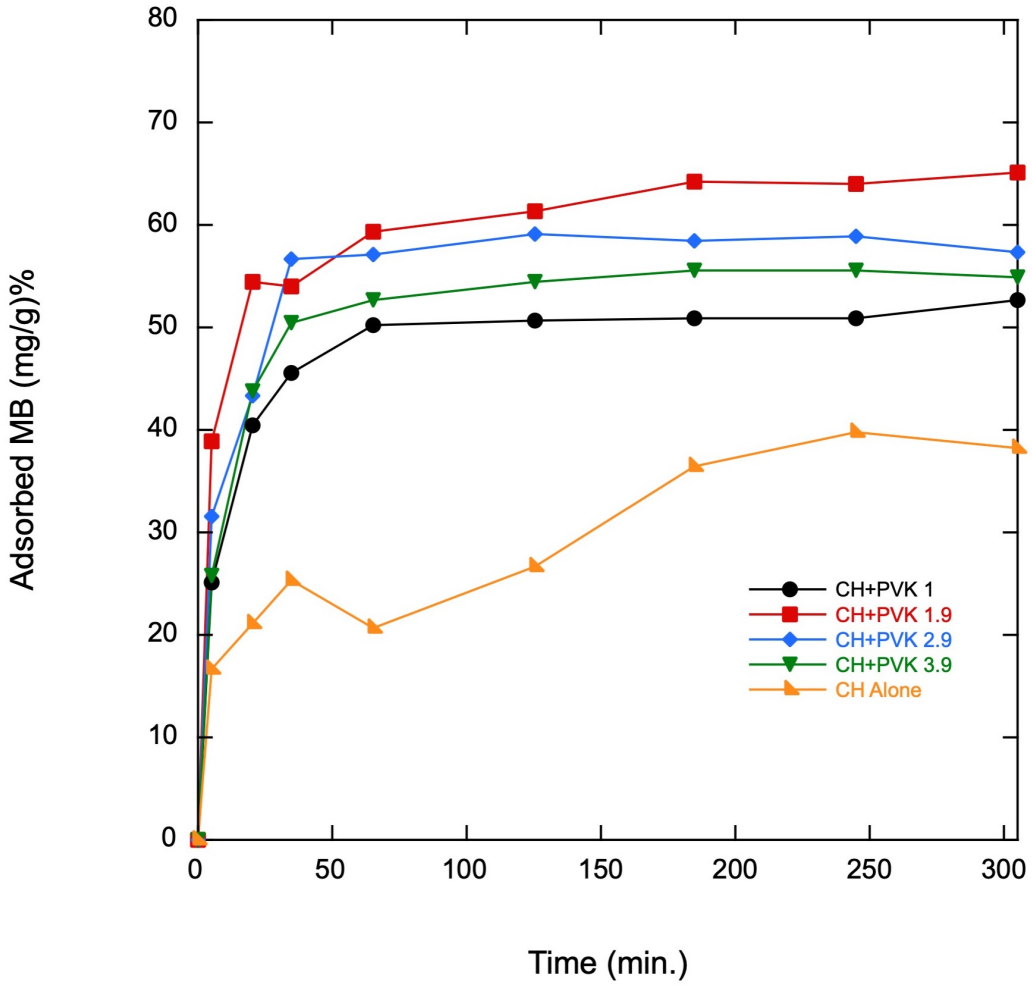

Figure A.5. Adsorption curves of MB treated with CH+PVK (1÷3.9) (1% w/v) and CH bubbles alone. Experimental errors are counted in the points size.

pollutants and especially for the stabilization of perovskite in water. Note that the starting point already has excellent results in these areas.

A.3 Conclusions

We treated one of the future applications of $CsPbBr_3$ as adsorbers in the processes of adsorbing pollutants from industrial waste water. With $CsPbBr_3$ nanopowders dissolved in aqueous solution or included in chitosan bubbles, we obtained a remarkable adsorption of Methylene Blue (MB). In the first case we get the disposal of the pollutant in a very short time (about 5 min). The results obtained have shown how the molar ratio of precursor salts used for the synthesis of perovskite affects the process of adsorption of pollutants in aqueous solution. In particular, using a $PbBr_2$/CsBr molar ratio of $\sim$2.9, MB adsorption is achieved by more than 70%, opening the way to use $CsPbBr_3$ as a MB adsorber.

In the second case, we have observed how the use of $CsPbBr_3$ inside chitosan bubbles acts as a catalyst in the processes of adsorption of MB from industrial waste water, increasing the adsorption capacity of chitosan compared to only chitosan bubbles. The time is longer but we have the advantage of being able to recover the perovskite once the adsorption process is over. Both systems can therefore be used for different purposes. Moreover it is interesting to note that the use of chitosan brings us closer to a solution for the well-known problem of stabilizing inorganic halide perovskite in water.

Finally it would be interesting to explore the possibility of a circular reuse of perovskites recovered from other applications, such as photovoltaics, and exploit their adsorbing properties. In this way it would be possible to create a double advantage for the environment: reduce the amount solid waste and improve water quality. These results open the way to the use of $CsPbBr_3$ perovskite NPs as adsorbers for different pollutants in water.

Appendix B

Papers published and conferences I attended during the PhD

The results shown in this PhD thesis have been published in several scientific journals and have been presented in several conferences. The list of supported publications and conferences is shown below.

Scientific Articles:

- Nonlinear emission in $CsPbBr_3$ decorated metasurfaces - Appl. Phys. Lett. 122, 241101 (**2023**). https://doi.org/10.1063/5.0140471
- Analysis of the Urbach tail in caesium lead halide perovskites - Journal of Applied Physics 131, 010902 (**2022**). https://doi.org/10.1063/5.0076712
- A new route for caesium lead halide perovskite deposition - J. Eur. Opt. Soc.-Rapid Publ. 17, 8 (**2021**). https://doi.org/10.1186/s41476-021-00153-y
- Large-Area Nanocrystalline Caesium Lead Chloride Thin Films: A Focus on the Exciton Recombination Dynamics - Nanomaterials **2021**, 11(2), 434. https://doi.org/10.3390/nano11020434

Conferences:

- **2022**: Amplified Spontaneous Emission in $CsPbBr_3$ Decorated Metasurfaces - 5^{th} Nanophotonics and Micro/Nano Optics International Conference - Paris. (*Author and Presenter*)
- **2022**: Adsorption of Pollutants by $CsPbBr_3$ Perovskite - 9^{th} IUPAC International Conference on Green Chemistry - Athens. (*Author and Presenter*)
- **2021**: Integration of $CsPbBr_3$ Nanocrystals with Dielectric Microspheres: A Novel Metasurface for Enhanced Emission in the Green - OSA Advanced Photonics Congress: Novel Optical Materials and Applications NOMA. (*Author and Presenter*)

- **2020**: A new route for high quality nanometric films of inorganic halide perovskites - EPJ Web of Conferences.

Bibliografia

[1] Giorgio Adamo et al. “Perovskite Metamaterials and Metasurfaces”. In: *Halide Perovskites for Photonics*. Ed. by A. Vinattieri and G. Giorgi. New York: AIP Publishing, 2021.

[2] Quinten A. Akkerman and Liberato Manna. “What Defines a Halide Perovskite?” In: *ACS Energy Letters* 5.2 (2020). PMID: 33344766, pp. 604–610. DOI: 10.1021/acsenergylett.0c00039. eprint: https://doi.org/10.1021/acsenergylett.0c00039. URL: https://doi.org/10.1021/acsenergylett.0c00039.

[3] Ivano Alessandri. “Enhancing Raman Scattering without Plasmons: Unprecedented Sensitivity Achieved by TiO_2 Shell-Based Resonators”. In: *Journal of the American Chemical Society* 135.15 (2013). PMID: 23560442, pp. 5541–5544. DOI: 10.1021/ja401666p. eprint: https://doi.org/10.1021/ja401666p. URL: https://doi.org/10.1021/ja401666p.

[4] Ivano Alessandri and John R. Lombardi. “Enhanced Raman Scattering with Dielectrics”. In: *Chemical Reviews* 116.24 (2016). PMID: 27739670, pp. 14921–14981. DOI: 10.1021/acs.chemrev.6b00365. eprint: https://doi.org/10.1021/acs.chemrev.6b00365. URL: https://doi.org/10.1021/acs.chemrev.6b00365.

[5] Sol Laura Gutierrez Alvarez et al. “Morphology-Dependent One- and Two-Photon Absorption Properties in Blue Emitting CsPbBr3 Nanocrystals”. In: *The Journal of Physical Chemistry Letters* 13.22 (2022). PMID: 35622447, pp. 4897–4904. DOI: 10.1021/acs.jpclett.2c00710. eprint: https://doi.org/10.1021/acs.jpclett.2c00710. URL: https://doi.org/10.1021/acs.jpclett.2c00710.

[6] Michal Baranowski and Paulina Plochocka. “Excitons in Metal-Halide Perovskites”. In: *Advanced Energy Materials* 10.26 (2020), p. 1903659. DOI: https://doi.org/10.1002/aenm.201903659. eprint: https://onlinelibrary.wiley.com/doi/pdf/10.1002/aenm.201903659. URL: https://onlinelibrary.wiley.com/doi/abs/10.1002/aenm.201903659.

[7] Kseniia Baryshnikova et al. “Broadband Antireflection with Halide Perovskite Metasurfaces”. In: *Laser & Photonics Reviews* 14.12 (2020), p. 2000338. DOI: https://doi.org/10.1002/lpor.202000338. eprint: https://onlinelibrary.wiley.com/doi/pdf/10.1002/lpor.202000338. URL: https://onlinelibrary.wiley.com/doi/abs/10.1002/lpor.202000338.

[8] Alexander S. Berestennikov et al. “Enhanced Photoluminescence of Halide Perovskite Nanocrystals Mediated by a Higher-Order Topological Metasurface”. In: *The Journal of Physical Chemistry C* 125.18 (2021), pp. 9884–9890. DOI: 10.1021/acs.jpcc.1c01492. eprint: https://doi.org/10.1021/acs.jpcc.1c01492. URL: https://doi.org/10.1021/acs.jpcc.1c01492.

[9] Rupak Bhattacharya, Bipul Pal, and Bhavtosh Bansal. “On conversion of luminescence into absorption and the van Roosbroeck-Shockley relation”. In: *Applied Physics Letters* 100 (May 2012). DOI: 10.1063/1.4721495.

[10] F. Biccari et al. “Superlinear emission in bare perovskite: amplified spontaneous emission in disordered film versus single crystal lasing”. In: *Materials Today: Proceedings* 4 (2017), S12–S18. ISSN: 2214-7853. DOI: https://doi.org/10.1016/j.matpr.2017.05.005. URL: https://www.sciencedirect.com/science/article/pii/S2214785317307137.

[11] M. Saad Bin-Alam et al. “Ultra-high-Q resonances in plasmonic metasurfaces”. In: *Nature Communications* 12.1 (2021). DOI: 10.1038/s41467-021-21196-2.

[12] Nicola Bontempi et al. “Plasmon-free SERS detection of environmental CO2 on TiO2 surfaces”. In: *Nanoscale* 8 (6 2016), pp. 3226–3231. DOI: 10.1039/C5NR08380J. URL: http://dx.doi.org/10.1039/C5NR08380J.

[13] Claudia Borri et al. “First Proof-of-Principle of Inorganic Lead Halide Perovskites Deposition by Magnetron-Sputtering”. In: *Nanomaterials* 10.1 (2020). ISSN: 2079-4991. DOI: 10.3390/nano10010060. URL: https://www.mdpi.com/2079-4991/10/1/60.

[14] Claudia Borri et al. “Nitrogen Rich Stainless Steel Coatings Obtained by RF Sputtering Process”. In: Mar. 2019, p. 6157. DOI: 10.3390/ciwc2019-06157.

[15] Caleb C. Boyd et al. “Understanding Degradation Mechanisms and Improving Stability of Perovskite Photovoltaics”. In: *Chemical Reviews* 119.5 (2019), pp. 3418–3451. DOI: 10.1021/acs.chemrev.8b00336. eprint: https://doi.org/10.1021/acs.chemrev.8b00336. URL: https://doi.org/10.1021/acs.chemrev.8b00336.

[16] Federico Brivio et al. “Lattice dynamics and vibrational spectra of the orthorhombic, tetragonal, and cubic phases of methylammonium lead iodide”. In: *Phys. Rev. B* 92 (14 2015), p. 144308. DOI: 10.1103/PhysRevB.92.144308. URL: https://link.aps.org/doi/10.1103/PhysRevB.92.144308.

[17] Mara Bruzzi et al. “Defective States in Micro-Crystalline $CsPbBr_3$ and Their Role on Photoconductivity”. In: *Nanomaterials* 9.2 (2019). ISSN: 2079-4991. DOI: 10.3390/nano9020177. URL: https://www.mdpi.com/2079-4991/9/2/177.

[18] Mara Bruzzi et al. “Electrically Active Defects in Polycrystalline and Single Crystal Metal Halide Perovskite”. In: *Energies* 13.7 (2020). ISSN: 1996-1073. DOI: 10.3390/en13071643. URL: https://www.mdpi.com/1996-1073/13/7/1643.

[19] M. Cardona and R.K. Kremer. "Temperature dependence of the electronic gaps of semiconductors". In: *Thin Solid Films* 571 (2014). 6th International Conference on Spectroscopic Ellipsometry (ICSE-VI), pp. 680–683. ISSN: 0040-6090. DOI: https://doi.org/10.1016/j.tsf.2013.10.157. URL: https://www.sciencedirect.com/science/article/pii/S0040609013017902.

[20] Hou-Tong Chen, Antoinette J Taylor, and Nanfang Yu. "A review of metasurfaces: physics and applications". In: *Reports on Progress in Physics* 79.7 (June 2016), p. 076401. DOI: 10.1088/0034-4885/79/7/076401. URL: https://dx.doi.org/10.1088/0034-4885/79/7/076401.

[21] Qi Chen et al. "Under the spotlight: The organic-inorganic hybrid halide perovskite for optoelectronic applications". In: *Nano Today* 10.3 (2015), pp. 355–396. ISSN: 1748-0132. DOI: https://doi.org/10.1016/j.nantod.2015.04.009. URL: https://www.sciencedirect.com/science/article/pii/S1748013215000560.

[22] In Chung et al. "CsSnI3: Semiconductor or Metal? High Electrical Conductivity and Strong Near-Infrared Photoluminescence from a Single Material. High Hole Mobility and Phase-Transitions". In: *Journal of the American Chemical Society* 134.20 (2012). PMID: 22578072, pp. 8579–8587. DOI: 10.1021/ja301539s. eprint: https://doi.org/10.1021/ja301539s. URL: https://doi.org/10.1021/ja301539s.

[23] G. D. Cody et al. "Disorder and the Optical-Absorption Edge of Hydrogenated Amorphous Silicon". In: *Phys. Rev. Lett.* 47 (20 1981), pp. 1480–1483. DOI: 10.1103/PhysRevLett.47.1480. URL: https://link.aps.org/doi/10.1103/PhysRevLett.47.1480.

[24] M Ibrahim Dar et al. "Origin of unusual bandgap shift and dual emission in organic-inorganic lead halide perovskites". In: *Science Advances* 2 (Oct. 2016), e1601156–e1601156. DOI: 10.1126/sciadv.1601156.

[25] Subham Dastidar et al. "Quantitative Phase-Change Thermodynamics and Metastability of Perovskite-Phase Cesium Lead Iodide". In: *The Journal of Physical Chemistry Letters* 8.6 (2017). PMID: 28256139, pp. 1278–1282. DOI: 10.1021/acs.jpclett.7b00134. eprint: https://doi.org/10.1021/acs.jpclett.7b00134. URL: https://doi.org/10.1021/acs.jpclett.7b00134.

[26] Maria Luisa De Giorgi et al. "Amplified Spontaneous Emission Threshold Reduction and Operational Stability Improvement in $CsPbBr_3$ Nanocrystals Films by Hydrophobic Functionalization of the Substrate". In: *Scientific Reports* 9.1 (2019).

[27] S. De Wolf et al. "Organometallic halide perovskites: Sharp optical absorption edge and its relation to photovoltaic performance". In: *Journal of Physical Chemistry Letters* 5.6 (2014), pp. 1035–1039. DOI: 10.1021/jz500279b.

[28] Stefaan De Wolf et al. "Organometallic Halide Perovskites: Sharp Optical Absorption Edge and Its Relation to Photovoltaic Performance". In: *The Journal of Physical Chemistry Letters* 5.6 (2014). PMID: 26270984, pp. 1035–1039. DOI: 10.1021/jz500279b. eprint: https://doi.org/10.1021/jz500279b. URL: https://doi.org/10.1021/jz500279b.

[29] Felix Deschler et al. "High Photoluminescence Efficiency and Optically Pumped Lasing in Solution-Processed Mixed Halide Perovskite Semiconductors". In: *The Journal of Physical Chemistry Letters* 5.8 (2014). PMID: 26269988, pp. 1421–1426. DOI: 10.1021/jz5005285. eprint: https://doi.org/10.1021/jz5005285. URL: https://doi.org/10.1021/jz5005285.

[30] A. Dobrovolsky. "*Defect-induced local variation of crystal phase transition temperature in metal-halide perovskites*". In: *Nat. Commun.* 8 (2017).

[31] John D. Dow and David Redfield. "Toward a Unified Theory of Urbach's Rule and Exponential Absorption Edges". In: *Phys. Rev. B* 5 (2 1972), pp. 594–610. DOI: 10.1103/PhysRevB.5.594. URL: https://link.aps.org/doi/10.1103/PhysRevB.5.594.

[32] S. W. Eatona. "*Lasing in robust cesium lead halide perovskite nanowires*". In: *PNAS* 113.8 (2016), pp. 3692–3696.

[33] Giles E. Eperon et al. "Inorganic caesium lead iodide perovskite solar cells". In: *J. Mater. Chem. A* 3 (39 2015), pp. 19688–19695. DOI: 10.1039/C5TA06398A. URL: http://dx.doi.org/10.1039/C5TA06398A.

[34] Naomi Falsini et al. "*A new route for caesium lead halide perovskite deposition*". In: *Journal of the European Optical Society-Rapid Publications* 17.1 (2021). DOI: 10.1186/s41476-021-00153-y.

[35] Naomi Falsini et al. "Analysis of the Urbach tail in cesium lead halide perovskites". In: *Journal of Applied Physics* 131.1 (2022), p. 010902. DOI: 10.1063/5.0076712.

[36] Hong-Hua Fang et al. "Photophysics of Organic-Inorganic Hybrid Lead Iodide Perovskite Single Crystals". In: *Advanced Functional Materials* 25.16 (), pp. 2378–2385. DOI: https://doi.org/10.1002/adfm.201404421. eprint: https://onlinelibrary.wiley.com/doi/pdf/10.1002/adfm.201404421. URL: https://onlinelibrary.wiley.com/doi/abs/10.1002/adfm.201404421.

[37] Ming Fu et al. "Neutral and Charged Exciton Fine Structure in Single Lead Halide Perovskite Nanocrystals Revealed by Magneto-optical Spectroscopy". In: *Nano Letters* 17.5 (2017). PMID: 28240910, pp. 2895–2901. DOI: 10.1021/acs.nanolett.7b00064. eprint: https://doi.org/10.1021/acs.nanolett.7b00064. URL: https://doi.org/10.1021/acs.nanolett.7b00064.

[38] Yongping Fu et al. "Broad Wavelength Tunable Robust Lasing from Single-Crystal Nanowires of Cesium Lead Halide Perovskites (CsPbX3, X = Cl, Br, I)". In: *ACS Nano* 10.8 (2016). PMID: 27437566, pp. 7963–7972. DOI: 10.1021/acsnano.6b03916. eprint: https://doi.org/10.1021/acsnano.6b03916. URL: https://doi.org/10.1021/acsnano.6b03916.

[39] Yongping Fu et al. "Metal halide perovskite nanostructures for optoelectronic applications and the study of physical properties". In: *Nature Reviews. Materials* 4.3 (Feb. 2019). ISSN: 2058-8437. DOI: 10.1038/s41578-019-0080-9. URL: https://www.osti.gov/biblio/1610661.

[40] Fabio Gabelloni et al. In: *Nanophotonics* 8.9 (2019), pp. 1447–1455. DOI: doi:10.1515/nanoph-2019-0013. URL: https://doi.org/10.1515/nanoph-2019-0013.

[41] Christian Gehrmann and David Egger. "Dynamic shortening of disorder potentials in anharmonic halide perovskites". In: *Nature Communications* 10 (July 2019). DOI: 10.1038/s41467-019-11087-y.

[42] S. Ghosh et al. "Vibrational study of lead bromide perovskite materials with variable cations based on Raman spectroscopy and density functional theory". In: *Journal of Raman Spectroscopy* (2021). DOI: 10.1002/jrs.6141.

[43] Feliciano Giustino and Henry J. Snaith. "Toward Lead-Free Perovskite Solar Cells". In: *ACS Energy Letters* 1.6 (2016), pp. 1233–1240. DOI: 10.1021/acsenergylett.6b00499. eprint: https://doi.org/10.1021/acsenergylett.6b00499. URL: https://doi.org/10.1021/acsenergylett.6b00499.

[44] V. M. Goldschmidt. "*Krystallbau und chemische zusammensetzung.*" In: *Ber. Dtsch. Chem.* 60 (5) (1927), pp. 1263–1296.

[45] Christopher Grote and Robert F. Berger. "Strain Tuning of Tin-Halide and Lead-Halide Perovskites: A First-Principles Atomic and Electronic Structure Study". In: *The Journal of Physical Chemistry C* 119.40 (2015), pp. 22832–22837. DOI: 10.1021/acs.jpcc.5b07446. eprint: https://doi.org/10.1021/acs.jpcc.5b07446. URL: https://doi.org/10.1021/acs.jpcc.5b07446.

[46] William Robert Grove. "VII. On the electro-chemical polarity of gases". In: *Philosophical Transactions of the Royal Society of London* 142 (1852), pp. 87–101. DOI: 10.1098/rstl.1852.0008. eprint: https://royalsocietypublishing.org/doi/pdf/10.1098/rstl.1852.0008. URL: https://royalsocietypublishing.org/doi/abs/10.1098/rstl.1852.0008.

[47] Jie Guan et al. "Internal-External Stabilization Strategies Enable Ultrastable and Highly Luminescent $CsPbBr_3$ Perovskite Nanocrystals for Aqueous Fe^3+ Detection and Information Encryption". In: *Advanced Materials Interfaces* 8.19 (2021), p. 2100588. DOI: https://doi.org/10.1002/admi.202100588. eprint: https://onlinelibrary.wiley.com/doi/pdf/10.1002/admi.202100588. URL: https://onlinelibrary.wiley.com/doi/abs/10.1002/admi.202100588.

[48] Massimo Gurioli et al. "Exciton thermalization in quantum-well structures". In: *Phys. Rev. B* 50 (16 1994), pp. 11817–11826. DOI: 10.1103/PhysRevB.50.11817. URL: https://link.aps.org/doi/10.1103/PhysRevB.50.11817.

[49] Haiping He et al. "Exciton Localization in Solution-Processed Organolead Trihalide Perovskites". In: *Nature communications* 7 (Mar. 2016), p. 10896. DOI: 10.1038/ncomms10896.

[50] Yihui He et al. “High spectral resolution of gamma-rays at room temperature by perovskite CsPbBr3 single crystals”. In: *Nature Communications* 9 (Apr. 2018). DOI: 10.1038/s41467-018-04073-3.

[51] Shunsuke Hirotsu et al. “Structural Phase Transitions in CsPbBr 3”. In: *Journal of the Physical Society of Japan* 37 (1974), pp. 1393–1398.

[52] Shaocong Hou et al. “Efficient Blue and White Perovskite Light-Emitting Diodes via Manganese Doping”. In: *Joule* 2.11 (2018), pp. 2421–2433. ISSN: 2542-4351. DOI: https://doi.org/10.1016/j.joule.2018.08.005. URL: https://www.sciencedirect.com/science/article/pii/S2542435118303854.

[53] Jie Hu et al. “A Review on Metasurface: From Principle to Smart Metadevices”. In: *Frontiers in Physics* 8 (2021). ISSN: 2296-424X. DOI: 10.3389/fphy.2020.586087. URL: https://www.frontiersin.org/articles/10.3389/fphy.2020.586087.

[54] Dewei Huang et al. “One-step solution deposition of CsPbBr3 based on precursor engineering for efficient all-inorganic perovskite solar cells”. In: *J. Mater. Chem. A* 7 (39 2019), pp. 22420–22428. DOI: 10.1039/C9TA08465G. URL: http://dx.doi.org/10.1039/C9TA08465G.

[55] Maya Isarov et al. “Rashba Effect in a Single Colloidal CsPbBr3 Perovskite Nanocrystal Detected by Magneto-Optical Measurements”. In: *Nano Letters* 17.8 (2017). PMID: 28657325, pp. 5020–5026. DOI: 10.1021/acs.nanolett.7b02248. eprint: https://doi.org/10.1021/acs.nanolett.7b02248. URL: https://doi.org/10.1021/acs.nanolett.7b02248.

[56] Ajay Kumar Jena, Ashish Kulkarni, and Tsutomu Miyasaka. “Halide Perovskite Photovoltaics: Background, Status, and Future Prospects”. In: *Chemical Reviews* 119.5 (2019), pp. 3036–3103. DOI: 10.1021/acs.chemrev.8b00539. eprint: https://doi.org/10.1021/acs.chemrev.8b00539. URL: https://doi.org/10.1021/acs.chemrev.8b00539.

[57] Junke Jiang et al. “Atomistic and Electronic Origin of Phase Instability of Metal Halide Perovskites”. In: *ACS Applied Energy Materials* 3.12 (2020), pp. 11548–11558. DOI: 10.1021/acsaem.0c00791. eprint: https://doi.org/10.1021/acsaem.0c00791. URL: https://doi.org/10.1021/acsaem.0c00791.

[58] Tobias Jochum et al. “All-in-one: a versatile gas sensor based on fiber enhanced Raman spectroscopy for monitoring postharvest fruit conservation and ripening”. In: *Analyst* 141 (6 2016), pp. 2023–2029. DOI: 10.1039/C5AN02120K. URL: http://dx.doi.org/10.1039/C5AN02120K.

[59] Jun Kang and Lin-Wang Wang. “High Defect Tolerance in Lead Halide Perovskite CsPbBr3”. In: *The Journal of Physical Chemistry Letters* 8.2 (2017). PMID: 28071911, pp. 489–493. DOI: 10.1021/acs.jpclett.6b02800. eprint: https://doi.org/10.1021/acs.jpclett.6b02800. URL: https://doi.org/10.1021/acs.jpclett.6b02800.

[60] M. Khenkin et al. “Consensus statement for stability assessment and reporting for perovskite photovoltaics based on ISOS procedures”. In: *Nature Energy* 5 (Jan. 2020), pp. 35–49. DOI: 10.1038/s41560-019-0529-5.

[61] Gregor Kieslich, Shijing Sun, and Anthony K. Cheetham. "An extended Tolerance Factor approach for organic-inorganic perovskites". In: *Chem. Sci.* 6 (6 2015), pp. 3430–3433. DOI: 10.1039/C5SC00961H. URL: http://dx.doi.org/10.1039/C5SC00961H.

[62] Gregor Kieslich, Shijing Sun, and Anthony K. Cheetham. "Solid-state principles applied to organic-inorganic perovskites: new tricks for an old dog". In: *Chem. Sci.* 5 (12 2014), pp. 4712–4715. DOI: 10.1039/C4SC02211D. URL: http://dx.doi.org/10.1039/C4SC02211D.

[63] H. Kim. "*Planar heterojunction organometal halide perovskite solar cells: roles of interfacial layers*". In: *Energy Environ. Sci.* 9 (2016), p. 12.

[64] Y.-H. Kim et al. "Comprehensive defect suppression in perovskite nanocrystals for high-efficiency light-emitting diodes". In: *Nature Photonics* 15.2 (2021), pp. 148–155. DOI: 10.1038/s41566-020-00732-4.

[65] Matthew Kirschner et al. "Photoinduced, reversible phase transitions in all-inorganic perovskite nanocrystals". In: *Nature Communications* 10 (Jan. 2019). DOI: 10.1038/s41467-019-08362-3.

[66] A. Kojima. "*Organometal Halide Perovskites as Visible-Light Sensitizers for Photovoltaic Cells*". In: *J. Am. Chem. Soc.* 131 (2009), p. 6050.

[67] S. Kondo. "*Stimulated emission from micro-crystalline $CsPbBr_3$ films: Edge emission versus surface emission*". In: *Materials Science and Engineering* B.137 (2007), pp. 156–161.

[68] S. Kondo et al. "Photoluminescence and stimulated emission from microcrystalline $CsPbCl_3$ films prepared by amorphous-to-crystalline transformation". In: *Phys. Rev. B* 70 (20 2004), p. 205322. DOI: 10.1103/PhysRevB.70.205322. URL: https://link.aps.org/doi/10.1103/PhysRevB.70.205322.

[69] W. Kong. "*Characterization of an abnormal photoluminescence behavior upon crystal-phase transition of perovskite $CH_3NH_3PbI_3$*". In: *Phys. Chem. Chem. Phys.* 17 (2015), pp. 16405–16411.

[70] M. Kulbak. "*Cesium Enhances Long-Term Stability of Lead Bromide Perovskite-Based Solar Cells*". In: *J. Phys. Chem. Lett.* 7 (2016), pp. 167–172.

[71] L. Lang. "*First-principles study on the electronic and optical properties of cubic ABX_3 halide perovskites*". In: *Physics Letters A* 378 (2014), pp. 290–293.

[72] P. Lautenschlager. "*Temperature dependence of band gaps in Si and Ge*". In: *Phys. Rev. B* 31.4 (1985), pp. 2163–2171.

[73] Martin Ledinsky et al. "Temperature Dependence of the Urbach Energy in Lead Iodide Perovskites". In: *The Journal of Physical Chemistry Letters* 10.6 (2019), pp. 1368–1373. DOI: 10.1021/acs.jpclett.9b00138. eprint: https://doi.org/10.1021/acs.jpclett.9b00138. URL: https://doi.org/10.1021/acs.jpclett.9b00138.

[74] Martin Ledinsky et al. "Temperature Dependence of the Urbach Energy in Lead Iodide Perovskites". In: *The Journal of Physical Chemistry Letters* 10.6 (2019), pp. 1368–1373. DOI: 10.1021/acs.jpclett.9b00138.

[75] Aurélien M. A. Leguy et al. "Dynamic disorder, phonon lifetimes, and the assignment of modes to the vibrational spectra of methylammonium lead halide perovskites". In: *Phys. Chem. Chem. Phys.* 18 (39 2016), pp. 27051–27066. DOI: 10.1039/C6CP03474H. URL: http://dx.doi.org/10.1039/C6CP03474H.

[76] B. Li. "*Pathways toward high-performance inorganic perovskite solar cells: challenges and strategies*". In: *Mater. Chem.* A.7 (2019), p. 20494.

[77] C. Li. "*Formability of ABX_3 (X= F, Cl, Br, I) halide perovskites*". In: *Acta Crystallogr. Sect.* B.64 (6) (2008), pp. 702–707.

[78] C. Li. "*Highly pure green light emission of perovskite $CsPbBr_3$ quantum dots and their application for green light-emitting diodes*". In: *Optic express* 24.13 (2016).

[79] G. Li. "*Efficient Light-Emitting Diodes Based on Nanocrystalline Perovskite in a Dielectric Polymer Matrix*". In: *Nano Lett.* 15.4 (2015), pp. 2640–2644.

[80] J. Li. "*Temperature-dependent photoluminescence of inorganic perovskite nanocrystal films*". In: *RSC Adv.* 6.82 (2016), pp. 78311–78316.

[81] Junqiang Li et al. "Single-Layer Halide Perovskite Light-Emitting Diodes with Sub-Band Gap Turn-On Voltage and High Brightness". In: *The Journal of Physical Chemistry Letters* 7.20 (2016). PMID: 27689966, pp. 4059–4066. DOI: 10.1021/acs.jpclett.6b01942. eprint: https://doi.org/10.1021/acs.jpclett.6b01942. URL: https://doi.org/10.1021/acs.jpclett.6b01942.

[82] Xiaoming Li et al. "All Inorganic Halide Perovskites Nanosystem: Synthesis, Structural Features, Optical Properties and Optoelectronic Applications". In: *Small* 13.9 (2017), p. 1603996. DOI: https://doi.org/10.1002/smll.201603996. eprint: https://onlinelibrary.wiley.com/doi/pdf/10.1002/smll.201603996. URL: https://onlinelibrary.wiley.com/doi/abs/10.1002/smll.201603996.

[83] Mengling Liao, Beibei Shan, and Ming Li. "In Situ Raman Spectroscopic Studies of Thermal Stability of All-Inorganic Cesium Lead Halide (CsPbX3, X = Cl, Br, I) Perovskite Nanocrystals". In: *The Journal of Physical Chemistry Letters* 10.6 (2019), pp. 1217–1225. DOI: 10.1021/acs.jpclett.9b00344.

[84] K. Lin. "*Perovskite light-emitting diodes with external quantum efficiency exceeding 20 per cent*". In: *Nature* 562 (2018), pp. 245–248.

[85] Feng Liu et al. "Highly Luminescent Phase-Stable CsPbI3 Perovskite Quantum Dots Achieving Near 100% Absolute Photoluminescence Quantum Yield". In: *ACS Nano* 11.10 (2017). PMID: 28910074, pp. 10373–10383. DOI: 10.1021/acsnano.7b05442.

[86] Guankui Long et al. "Perovskite metasurfaces with large superstructural chirality". In: *Nature Communications* 13.1 (2022). Cited by: 11; All Open Access, Gold Open Access, Green Open Access. DOI: 10.1038/s41467-022-29253-0.

[87] Marina Maddaloni, Irene Vassalini, and Ivano Alessandri. "Green Routes for the Development of Chitin/Chitosan Sustainable Hydrogels". In: *Sustainable Chemistry* 1.3 (2020), pp. 325–344. ISSN: 2673-4079. DOI: 10.3390/suschem1030022. URL: https://www.mdpi.com/2673-4079/1/3/22.

[88] S. Meloni. "*Valence and conduction band tuning in halide perovskites for solar cell applications*". In: *J. Mater. Chem. A* 4.41 (2016), pp. 15997–16002.

[89] L. Meng. "*Addressing the stability issue of perovskite solar cells for commercial applications*". In: *Nature Communications* 9 (2018), p. 5265.

[90] R. Milot. "*Temperature-dependent charge-carrier dynamics in $CH_3NH_3PbI_3$ perovskite thin films*". In: *Adv. Funct. Mater.* 25.39 (2015), pp. 6218–6227.

[91] H. Min et al. "Perovskite solar cells with atomically coherent interlayers on SnO2 electrodes". In: *Nature* 598.7881 (2021), pp. 444–450.

[92] C. K. Moller. "*Crystal Structure and Photoconductivity of Caesium Plumbohalides*". In: *Nature* 182 (1958), p. 1436.

[93] Edoardo Mosconi, Thibaud Etienne, and Filippo De Angelis. "Rashba Band Splitting in Organohalide Lead Perovskites: Bulk and Surface Effects". In: *The Journal of Physical Chemistry Letters* 8.10 (2017). PMID: 28467716, pp. 2247–2252. DOI: 10.1021/acs.jpclett.7b00328. eprint: https://doi.org/10.1021/acs.jpclett.7b00328. URL: https://doi.org/10.1021/acs.jpclett.7b00328.

[94] Kyle T. Munson et al. "Dynamic Disorder Dominates Delocalization, Transport, and Recombination in Halide Perovskites". In: *Chem* 4.12 (2018), pp. 2826–2843. ISSN: 2451-9294. DOI: https://doi.org/10.1016/j.chempr.2018.09.001. URL: https://www.sciencedirect.com/science/article/pii/S2451929418304108.

[95] G. Murtaza. "*First principle study of the structural and optoelectronic properties of cubic perovskites $CsPbM_3$ (M=Cl, Br,I)*". In: *Physica B406* (2011), pp. 3222–3229.

[96] W. Nie. "*Light-activated photocurrent degradation and self-healing in perovskite solar cells*". In: *Nat. Commun.* 7 (2016), p. 11574.

[97] D. Olguin. "*Electron-phonon effects on the direct band gap in semiconductors: LCAO calculations*". In: *Solid State Commun.* 122.11 (2002), pp. 575–589.

[98] Luis K. Ono, Shengzhong (Frank) Liu, and Yabing Qi. "Reducing Detrimental Defects for High-Performance Metal Halide Perovskite Solar Cells". In: *Angewandte Chemie International Edition* 59.17 (2020), pp. 6676–6698. DOI: https://doi.org/10.1002/anie.201905521. eprint: https://onlinelibrary.wiley.com/doi/pdf/10.1002/anie.201905521. URL: https://onlinelibrary.wiley.com/doi/abs/10.1002/anie.201905521.

[99] Robert M. Pasquarelli, David S. Ginley, and Ryan O'Hayre. "Solution processing of transparent conductors: from flask to film". In: *Chem. Soc. Rev.* 40 (11 2011), pp. 5406–5441. DOI: 10.1039/C1CS15065K. URL: http://dx.doi.org/10.1039/C1CS15065K.

[100] Laura Piveteau et al. “Bulk and Nanocrystalline Cesium Lead-Halide Perovskites as Seen by Halide Magnetic Resonance”. In: *ACS Central Science* 6.7 (2020). PMID: 32724848, pp. 1138–1149. DOI: 10.1021/acscentsci.0c00587. eprint: https://doi.org/10.1021/acscentsci.0c00587. URL: https://doi.org/10.1021/acscentsci.0c00587.

[101] Neda Pourdavoud et al. “Room-Temperature Stimulated Emission and Lasing in Recrystallized Cesium Lead Bromide Perovskite Thin Films”. In: *Advanced Materials* 31.39 (2019), p. 1903717. DOI: https://doi.org/10.1002/adma.201903717. eprint: https://onlinelibrary.wiley.com/doi/pdf/10.1002/adma.201903717. URL: https://onlinelibrary.wiley.com/doi/abs/10.1002/adma.201903717.

[102] Michael B. Price et al. “Whispering-Gallery Mode Lasing in Perovskite Nanocrystals Chemically Bound to Silicon Dioxide Microspheres”. In: *The Journal of Physical Chemistry Letters* 11.17 (2020). PMID: 32786818, pp. 7009–7014. DOI: 10.1021/acs.jpclett.0c02003. eprint: https://doi.org/10.1021/acs.jpclett.0c02003. URL: https://doi.org/10.1021/acs.jpclett.0c02003.

[103] Loredana Protesescu et al. “Nanocrystals of Cesium Lead Halide Perovskites ($CsPbX_3$, X = Cl, Br, and I): Novel Optoelectronic Materials Showing Bright Emission with Wide Color Gamut”. In: *Nano Letters* 15.6 (2015). PMID: 25633588, pp. 3692–3696. DOI: 10.1021/nl5048779. eprint: https://doi.org/10.1021/nl5048779. URL: https://doi.org/10.1021/nl5048779.

[104] Gabriele RainÃ² et al. “Single Cesium Lead Halide Perovskite Nanocrystals at Low Temperature: Fast Single-Photon Emission, Reduced Blinking, and Exciton Fine Structure”. In: *ACS Nano* 10.2 (2016). PMID: 26771336, pp. 2485–2490. DOI: 10.1021/acsnano.5b07328. eprint: https://doi.org/10.1021/acsnano.5b07328. URL: https://doi.org/10.1021/acsnano.5b07328.

[105] Y. Rakita et al. “Mechanical properties of APbX3 (A = Cs or CH3NH3; X = i or Br) perovskite single crystals”. In: *MRS Communications* 5.4 (2015), pp. 623–629. DOI: 10.1557/mrc.2015.69.

[106] Julien Ramade et al. “Fine structure of excitons and electron-hole exchange energy in polymorphic CsPbBr3 single nanocrystals”. In: *Nanoscale* 10 (14 2018), pp. 6393–6401. DOI: 10.1039/C7NR09334A. URL: http://dx.doi.org/10.1039/C7NR09334A.

[107] Marcello Righetto and Franco Cacialli. “Charge Transport Layers in Halide Perovskite Photonic Devices”. In: *Halide Perovskites for Photonics*. Chap. Chapter 5, pp. 5-1-5–32. DOI: 10.1063/9780735423633_005. eprint: https://aip.scitation.org/doi/pdf/10.1063/9780735423633_005. URL: https://aip.scitation.org/doi/abs/10.1063/9780735423633_005.

[108] G. Rose. *De novis quibusdam fossilibus quae in montibus Uraliis inveniuntur*. typis A.G. Schadii e Berolini, Berlin, 1839.

[109] Maximilian J. Schilcher et al. "The Significance of Polarons and Dynamic Disorder in Halide Perovskites". In: *ACS Energy Letters* 6.6 (2021), pp. 2162–2173. DOI: 10.1021/acsenergylett.1c00506. eprint: https://doi.org/10.1021/acsenergylett.1c00506. URL: https://doi.org/10.1021/acsenergylett.1c00506.

[110] R. F. Schnabel et al. "Influence of exciton localization on recombination line shapes: $In_xGa_{1-x}As$/GaAs quantum wells as a model". In: *Phys. Rev. B* 46 (15 1992), pp. 9873–9876. DOI: 10.1103/PhysRevB.46.9873. URL: https://link.aps.org/doi/10.1103/PhysRevB.46.9873.

[111] M. Sebastian et al. "Excitonic emissions and above-band-gap luminescence in the single-crystal perovskite semiconductors $CsPbBr_3$ and $CsPbCl_3$". In: *Phys. Rev. B* 92 (23 2015), p. 235210. DOI: 10.1103/PhysRevB.92.235210. URL: https://link.aps.org/doi/10.1103/PhysRevB.92.235210.

[112] Fumiya Sekiguchi et al. "Enhancing the Hot-Phonon Bottleneck Effect in a Metal Halide Perovskite by Terahertz Phonon Excitation". In: *Phys. Rev. Lett.* 126 (7 2021), p. 077401. DOI: 10.1103/PhysRevLett.126.077401. URL: https://link.aps.org/doi/10.1103/PhysRevLett.126.077401.

[113] Muthaiah Shellaiah and Kien Wen Sun. "Review on Sensing Applications of Perovskite Nanomaterials". In: *Chemosensors* 8.3 (2020). ISSN: 2227-9040. DOI: 10.3390/chemosensors8030055. URL: https://www.mdpi.com/2227-9040/8/3/55.

[114] Rohan Singh et al. "Localization dynamics of excitons in disordered semiconductor quantum wells". In: *Phys. Rev. B* 95 (23 2017), p. 235307. DOI: 10.1103/PhysRevB.95.235307. URL: https://link.aps.org/doi/10.1103/PhysRevB.95.235307.

[115] S. Singh. "*Effect of thermal and structural disorder on the electronic structure of hybrid perovskite semiconductor* $CH_3NH_3PbI_3$". In: *J. Phys. Chem. Lett.* 7.15 (2016), pp. 3014–3021.

[116] T. Skettrup. "Urbach's rule derived from thermal fluctuations in the band-gap energy". In: *Phys. Rev. B* 18 (6 1978), pp. 2622–2631. DOI: 10.1103/PhysRevB.18.2622. URL: https://link.aps.org/doi/10.1103/PhysRevB.18.2622.

[117] Henry Snaith. "Present status and future prospects of perovskite photovoltaics". In: *Nature Materials* 17 (Apr. 2018). DOI: 10.1038/s41563-018-0071-z.

[118] T. Soma. "*Thermal expansion coefficient of GaAs and InP*". In: *Solid State Commun.* 42.12 (1982), pp. 889–892.

[119] J. Song. "*Monolayer and Few-Layer All-Inorganic Perovskites as a New Family of Two-Dimensional Semiconductors for Printable Optoelectronic Devices*". In: *Adv. Mater.* 28 (2016), p. 4861.

[120] J. Song. "*Quantum Dot Light- Emitting Diodes Based on Inorganic Perovskite Cesium Lead Halides* ($CsPbX_3$)". In: *Adv. Mater.* 27 (2015), p. 7162.

[121] C. C. Stoumpos. "*Growth of the Perovskite Semiconductor $CsPbBr_3$: A New Material for High-Energy Radiation Detection*". In: *Cryst. Growth Des.* 13 (2013), pp. 2722–2727.

[122] Daniel B. Straus et al. "Understanding the Instability of the Halide Perovskite CsPbI3 through Temperature-Dependent Structural Analysis". In: *Advanced Materials* 32.32 (2020), p. 2001069. DOI: https://doi.org/10.1002/adma.202001069. eprint: https://onlinelibrary.wiley.com/doi/pdf/10.1002/adma.202001069. URL: https://onlinelibrary.wiley.com/doi/abs/10.1002/adma.202001069.

[123] I. Suárez and J. P. Martínez Pastor. "Amplified spontaneous emission generation in lead halide perovskite semiconductors". In: *Halide Perovskites for Photonics*. Ed. by A. Vinattieri and G. Giorgi. New York: AIP Publishing, 2021.

[124] Hitoshi Sumi and Yutaka Toyozawa. "Urbach-Martienseen Rule and Exciton Trapped Momentarily by Lattice Vibrations". In: *Journal of the Physical Society of Japan* 31.2 (1971), pp. 342–358. DOI: 10.1143/JPSJ.31.342. eprint: https://doi.org/10.1143/JPSJ.31.342. URL: https://doi.org/10.1143/JPSJ.31.342.

[125] R. J. Sutton. "*Bandgap-Tunable Cesium Lead Halide Perovskites with High Thermal Stability for Efficient Solar Cells*". In: *Adv. Energy Mater.* 6 (2016), p. 1502458.

[126] Sarunas Svirskas et al. "Phase transitions, screening and dielectric response of $CsPbBr_3$". In: *J. Mater. Chem. A* 8 (28 2020), pp. 14015–14022. DOI: 10.1039/D0TA04155F. URL: http://dx.doi.org/10.1039/D0TA04155F.

[127] Weijian Tao et al. "Momentarily trapped exciton polaron in two-dimensional lead halide perovskites". In: *Nature communications* 12.1 (2021), p. 1400. ISSN: 2041-1723. DOI: 10.1038/s41467-021-21721-3. URL: https://europepmc.org/articles/PMC7930248.

[128] Ujwal K. Thakur et al. "Consistently High Voc Values in p-i-n Type Perovskite Solar Cells Using Ni3+-Doped NiO Nanomesh as the Hole Transporting Layer". In: *ACS Applied Materials & Interfaces* 12.10 (2020). PMID: 31904215, pp. 11467–11478. DOI: 10.1021/acsami.9b18197.

[129] E. L. Unger. "*Roadmap and roadblocks for the band gap tunability of metal halide perovskites*". In: *J. Mater. Chem.* A.5 (2017), pp. 11401–11409.

[130] Y. P. Varshni. "*Temperature dependence of the energy gap in semiconductors*". In: *Physica* 34 (1967), pp. 149–154.

[131] Irene Vassalini et al. "The role of morphology in all-dielectric SERS: A comparison between conformal (T-rex) and non conformal TiO2 shells". In: *Vibrational Spectroscopy* 109 (2020), p. 103085. ISSN: 0924-2031. DOI: https://doi.org/10.1016/j.vibspec.2020.103085. URL: https://www.sciencedirect.com/science/article/pii/S0924203120300886.

[132] Y. Wang. "*All-Inorganic Colloidal Perovskite Quantum Dots: A New Class of Lasing Materials with Favorable Characteristics*". In: *Adv. Mater.* 27 (2015), pp. 7101–7108.

[133] Haotong Wei and Jinsong Huang. "Halide lead perovskites for ionizing radiation detection". In: *NATURE COMMUNICATIONS* 10 (2019). ISSN: 2041-1723. DOI: 10.1038/s41467-019-08981-w.

[134] K. Wei. "*Temperature-dependent excitonic photoluminescence excited by two-photon absorption in perovskite $CsPbBr_3$ quantum dots*". In: *Opt. Lett.* 41.16 (2016), p. 3821.

[135] Christoph Wolf and Tae-Woo Lee. "*Exciton and lattice dynamics in low-temperature processable $CsPbBr_3$ thin-films*". In: *Materials Today Energy* 7 (2018), pp. 199–207. ISSN: 2468-6069. DOI: https://doi.org/10.1016/j.mtener.2017.09.010. URL: https://www.sciencedirect.com/science/article/pii/S2468606917301600.

[136] Joeson Wong, Stefan T. Omelchenko, and Harry A. Atwater. "Impact of Semiconductor Band Tails and Band Filling on Photovoltaic Efficiency Limits". In: *ACS Energy Letters* 6.1 (2021), pp. 52–57. DOI: 10.1021/acsenergylett.0c02362. eprint: https://doi.org/10.1021/acsenergylett.0c02362. URL: https://doi.org/10.1021/acsenergylett.0c02362.

[137] Guanjun Xiao et al. "Pressure Effects on Structure and Optical Properties in Cesium Lead Bromide Perovskite Nanocrystals". In: *Journal of the American Chemical Society* 139.29 (2017). PMID: 28682634, pp. 10087–10094. DOI: 10.1021/jacs.7b05260.

[138] Minghong Xie et al. "Solution-processed whispering-gallery-mode microsphere lasers based on colloidal CsPbBr3 perovskite nanocrystals". In: *Nanotechnology* 33.11 (2021), p. 115204.

[139] S. Yakunin. "*Low-threshold amplified spontaneous emission and lasing from colloidal nanocrystals of caesium lead halide perovskites*". In: *Nature Communications* 6.8056 (2015).

[140] Sergii Yakunin et al. "Low-threshold amplified spontaneous emission and lasing from colloidal nanocrystals of caesium lead halide perovskites". In: *Nature Communications* 6 (2015).

[141] Takumi Yamada et al. "Light emission from halide perovskite semiconductors: bulk crystals, thin films, and nanocrystals". In: *Journal of Physics D: Applied Physics* 54.38 (2021), p. 383001. DOI: 10.1088/1361-6463/ac0e58. URL: https://dx.doi.org/10.1088/1361-6463/ac0e58.

[142] Dongdong Yan et al. "Stable and low-threshold whispering-gallery-mode lasing from modified $CsPbBr_3$ perovskite quantum dots SiO_2 sphere". In: *Chemical Engineering Journal* 401 (2020), p. 126066.

[143] Ruo Xi Yang et al. "Spontaneous Octahedral Tilting in the Cubic Inorganic Cesium Halide Perovskites CsSnX3 and CsPbX3 (X = F, Cl, Br, I)". In: *The Journal of Physical Chemistry Letters* 8.19 (2017). PMID: 28903562, pp. 4720–4726. DOI: 10.1021/acs.jpclett.7b02423. eprint: https://doi.org/10.1021/acs.jpclett.7b02423. URL: https://doi.org/10.1021/acs.jpclett.7b02423.

[144] S. Yang. "*Recent advances in perovskite solar cells: efficiency, stability and lead-free perovskite*". In: *Journal of Materials Chemistry* A.5 (2017), p. 11462.

[145] Ye Yang et al. "Observation of a hot-phonon bottleneck in lead-iodide perovskites". In: *Nature Photonics* 10.1 (2016), pp. 53–59. DOI: 10.1038/nphoton.2015.213.

[146] Zhichun Yang et al. "Research progress on large-area perovskite thin films and solar modules". In: *Journal of Materiomics* 3.4 (2017), pp. 231–244. ISSN: 2352-8478. DOI: https://doi.org/10.1016/j.jmat.2017.09.002. URL: https://www.sciencedirect.com/science/article/pii/S2352847817300576.

[147] N. Yantara. "*Inorganic Halide Perovskites for Efficient Light-Emitting Diodes*". In: *J. Phys. Chem. Lett.* 6.21 (2015), pp. 4360–4364.

[148] Junzhi Ye et al. "Defect Passivation in Lead-Halide Perovskite Nanocrystals and Thin Films: Toward Efficient LEDs and Solar Cells". In: *Angewandte Chemie International Edition* 60.40 (2021), pp. 21636–21660. DOI: https://doi.org/10.1002/anie.202102360. eprint: https://onlinelibrary.wiley.com/doi/pdf/10.1002/anie.202102360. URL: https://onlinelibrary.wiley.com/doi/abs/10.1002/anie.202102360.

[149] Y. Ye. "*Nature of the band gap of halide perovskites $ABX_3(A = CH_3NH_3, Cs; B = Sn, Pb; X = Cl, Br, I)$: First-principles calculations*". In: *Chin. Phys. B* 24.11 (2015), p. 116302.

[150] Zixi Yin et al. "Defect-Induced Inhomogeneous Phase Transition in 2D Perovskite Single Crystals at Low Temperatures". In: *ACS Omega* 6.51 (2021), pp. 35427–35432. DOI: 10.1021/acsomega.1c04800. eprint: https://doi.org/10.1021/acsomega.1c04800. URL: https://doi.org/10.1021/acsomega.1c04800.

[151] J. Young. "*Octahedral rotation preferences in perovskites iodides and bromides*". In: *J. Phys. Chem. Lett.* 7 (2016), pp. 918–922.

[152] C. Yu. "*Temperature dependence of the band gap of perovskite semiconductor compound $CsSnI_3$*". In: *J. Appl. Phys.* 110.6 (2011), p. 063526.

[153] Huimin Yu et al. "Narrow linewidth CsPbBr3 perovskite quantum dots microsphere lasers". In: *Optical Materials* 133 (2022), p. 112907. ISSN: 0925-3467. DOI: https://doi.org/10.1016/j.optmat.2022.112907. URL: https://www.sciencedirect.com/science/article/pii/S0925346722009417.

[154] Jiaoxian Yu et al. "Perovskite CsPbBr3 crystals: growth and applications". In: *J. Mater. Chem. C* 8 (19 2020), pp. 6326–6341. DOI: 10.1039/D0TC00922A. URL: http://dx.doi.org/10.1039/D0TC00922A.

[155] Huiling Zhang et al. "Amplified spontaneous emission and random lasing using CsPbBr3 quantum dot glass through controlling crystallization". In: *Chem. Commun.* 56 (19 2020), pp. 2853–2856. DOI: 10.1039/C9CC07676J. URL: http://dx.doi.org/10.1039/C9CC07676J.

[156] Q. Zhang. "*Room-temperature nearinfrared high-Q perovskite whispering gallery planar nanolasers*". In: *Nano Lett.* 14.10 (2014), pp. 5995–6001.

[157] Q. Zhang et al. "Efficient metal halide perovskite light-emitting diodes with significantly improved light extraction on nanophotonic substrates". In: *Nature Communications* 10.1 (2019). DOI: 10.1038/s41467-019-08561-y.

[158] Yuji Zhao et al. “Green Semipolar (2021) InGaN Light-Emitting Diodes with Small Wavelength Shift and Narrow Spectral Linewidth”. In: *Applied Physics Express* 6.6 (2013), p. 062102. DOI: 10.7567/APEX.6.062102. URL: https://dx.doi.org/10.7567/APEX.6.062102.

[159] Yixuan Zhou et al. “Nonlinear optical properties of halide perovskites and their applications”. In: *Applied Physics Reviews* 7.4 (2020), p. 041313. DOI: 10.1063/5.0025400. eprint: https://doi.org/10.1063/5.0025400. URL: https://doi.org/10.1063/5.0025400.

[160] H. Zhu. “*Lead halide perovskite nanowire lasers with low lasing thresholds and high quality factors*”. In: *Nat Mater* 14.6 (2015), pp. 636–642.

Acknowledgements

The research activity presented in this PhD thesis has been supported by the Department of Information Engineering DII of the University of Brescia, in the framework of *"Dipartimento di Eccellenza 2018-2022"* program.

I would like to thank Prof. I. Alessandri for the opportunity, the passion and the teachings that he has transmitted to me in these three years of my PhD that I believe have been very formative. I am grateful for sharing this journey with you.

I would like to thank Prof.sa A. Vinattieri for having accompanied me also in this goal of PhD, for the advice, the stimulating discussions, the passion and the teachings and for believing in me all these years that I'm happy to have shared.

Thanks to Prof. F. Biccari for support, help and advice on the subject.

Thanks to all the Chem4Tech group for welcoming me, for the hospitality, the affection and the exciting discussions made together that allowed me to grow.